UNIVERSITÀ DEGLI STUDI DI PADOVA

UNIVERSITA' DEGLI STUDI DI PADOVA

Dipartimento di Ingegneria Industriale DII

Corso di Laurea Magistrale Energy Engineering

Experimental investigation of flow condensation of propylene in a horizontal smooth tube

Relatore: Prof. Davide Del Col (DII – Università di Padova)

Co-Relatore: Prof. Andrea Luke (TTK – Universität Kassel)

Supervisore: Christos Tsitsiloudis (TTK – Universität Kassel)

Luca Vittorio Valentini – Mat. 2055043

Anno Accademico 2023/2024

Ringrazio tutte le persone che mi sono state vicino durante i miei studi. Ringrazio in maniera particolare la Prof. Co-relatrice Luke e il supervisore Christos per avermi accolto nel gruppo di ricerca del TTK presso l'Università di Kassel e per avermi supportato nella realizzazione del presente lavoro. Un ringraziamento speciale al tecnico di laboratorio Reiner e al collaboratore Ziat per il loro importante contributo nella preparazione del tubo sperimentale.

Infine, ringrazio il relatore Prof. Del Col per l'opportunità offertami.

I thank all the people who have been close to me during my studies. In particular, I would like to thank my Co-Rapporteur Prof. Luke and my supervisor Christos for welcoming me into the research group of the TTK pressure University of Kassel and for supporting me in the realization of the experimental work and the writing of this thesis. I dedicate special thanks to Reiner and Ziat for their important contribution in preparing the experimental tube.

Finally, I thank the supervisor Prof. Del Col for the opportunity given to me.

Abstract

Flow condensation is a very widely spread physical process, used in condensers adopted for several applications like heat pumps, air conditioning systems, and the chemical industry. The urge of the refrigeration industry to find alternative refrigerants to HFC, characterized by null ODP but too high GWP, makes the study of hydrocarbons for inverse cycle applications very important. The goal of the present work is to study flow condensation of propylene inside a horizontal smooth tube. Flow condensation is a very complex heat transfer mechanism that currently, cannot be described by analytical equations. Therefore, experimental analysis becomes an important tool to validate the correlations presented in the literature. The present experimental work has been conducted exploiting an industrial scale test rig, KIIR, that allows to set the thermodynamics conditions at the inlet of the test section, where partial condensation occurs. The test section consists in a tube-shell-heat exchanger. Propylene is cooled down by an oil in counter-current flow configuration. The test tube has been equipped with temperature sensors and installed in the experimental apparatus and the measurement plan has been conducted. Each test has been executed under constant operating conditions in terms of pressure p, mass flux G and vapor quality x.

The analysis of the local experimental results has allowed to observe the dependency of the heat transfer coefficient α on the radial position ϕ of the test tube. Specifically, under test conditions associated with the occurrence of stratified flow, the heat transfer coefficient α varies considerably as function of the radial position ϕ. Under the conditions associated with high turbulence and annular flow, the heat transfer coefficient α is approximately constant as function of the radial position ϕ. Because of the uncertainties of the experimental set up, these observations were clearer under the test conditions in which the average temperature difference between the test substance and the cooling oil was higher.

Moreover, it was observed that the overall heat transfer coefficient α increases as the mass flux G increases. In the same way, it was possible to observe that the overall heat transfer coefficient α decreases as the pressure p increases. By comparing the results regarding overall heat transfer and pressure drops, it was verified that a high heat transfer coefficient is always coupled with a high value of pressure drops.

Sommario

La condensazione durante deflusso è un processo fisico molto diffuso, utilizzato nei condensatori adottati per diverse applicazioni come pompe di calore, impianti di condizionamento e nell'industria chimica. L'esigenza dell'industria della refrigerazione di trovare refrigeranti alternativi a HFC, caratterizzati da un ODP quasi nullo ma da un GWP troppo elevato, rende molto importante lo studio degli idrocarburi per le applicazioni a ciclo inverso. L'obiettivo del presente lavoro è studiare la condensazione del flusso di propilene all'interno di un tubo orizzontale liscio. La condensazione in flusso è un meccanismo di trasferimento del calore molto complesso che attualmente non può essere descritto da equazioni analitiche. Pertanto, l'analisi sperimentale diventa uno strumento importante per convalidare le correlazioni presentate in letteratura. Il lavoro sperimentale è stato condotto sfruttando un impianto di prova su scala industriale, il KIIR, che consente di impostare le condizioni termodinamiche all'ingresso della sezione di prova, dove avviene la condensazione parziale. La sezione di prova consiste in uno scambiatore di calore a fascio tubiero. Il propilene viene raffreddato da un olio in configurazione di flusso controcorrente. Il tubo sperimentale è stato dotato di sensori di temperatura e installato all'interno dell'apparato sperimentale. Ciascun test è stato eseguito in condizioni operative costanti in termini di pressione p, flusso di massa G e titolo di vapore x. L'analisi dei risultati a livello locale ha permesso di dimostrare la dipendenza del coefficiente di trasferimento di calore α dalla posizione radiale ϕ del tubo. In particolare, nelle condizioni di prova associate al verificarsi di un flusso stratificato, il coefficiente di trasferimento di calore α varia notevolmente in funzione della posizione radiale ϕ. Nelle condizioni di alta turbolenza e flusso anulare, il coefficiente di trasferimento di calore α è approssimativamente costante in funzione della posizione radiale ϕ. A causa delle incertezze del set-up sperimentale, queste osservazioni sono state più chiare nelle condizioni di

prova in cui la differenza di temperatura media tra la sostanza in esame e l'olio di raffreddamento era più elevata.

Inoltre, è stato possibile verificare sperimentalmente che il coefficiente di trasferimento del calore α aumenta all'aumentare del flusso di massa G. Allo stesso modo, è stato possibile verificare che il coefficiente di trasferimento di calore α diminuisce con l'aumento della pressione p.

Confrontando i risultati relativi al trasferimento di calore complessivo e alle perdite di carico, si è dedotto che un elevato coefficiente di trasferimento di calore è sempre abbinato a un alto valore di perdite di carico.

Contents

Nomenclature

Latin symbols

a	height, [m]
A	area, [m^2]
A_0^*	TC calibration coefficient, [−]
B	linear interpolation coefficient, [−]
B_0^*	TC calibration coefficient, [−]
c	convective film constant, [−]
c_p	isobaric heat capacity, [J/(kg·K)]
C	linear interpolation coefficient, [−]
C_D	drag coefficient, [−]
C_{LM}	parameter from Lockhart Martinelli correlation, [−]
d	diameter, [m]
d_H	hydraulic diameter, [m]
D	linear interpolation coefficient, [−]
E	linear interpolation coefficient, [−]
f	friction factor, [−]
g	gravity force, [m/s^2]
G	mass flux, [kg/(m^{2}s)]
h	specific enthalpy, [J/kg]
h_{LV}	specific latent heat of vaporization, [J/kg]
J_V	dimensionless vapor velocity, [−]
K	overall heat transfer coefficient, [W/m^{2}K]
l	characteristic length, [m]
L	tube length, [m]
$\dot{m}$	mass flow rate, [kg/s]
M	coefficient for Muller's frictional pressure drop model, [−]
N	coefficient for Muller's frictional pressure drop model, [−]
p	Pressure, [bar]
p^*	reduced pressure, [−]
p_{crit}	critical pressure, [bar]
P	coefficient for Muller's frictional pressure drop model, [−]
P_i	perimeter of liquid-vapor interface, [m]

q	heat flux, [W/m^2]
$\dot{Q}$	heat flow rate, [W]
r	radius, [m]
R	thermal resistance, [m^2·K/W]
R_F	Friedel's two phase multiplier, [−]
S	coefficient for Muller's frictional pressure drop model, [−]
T	temperature, [°C]
u	velocity, [m/s]
U	characteristic velocity, [m/s]
x	vapor quality, [−]
X_{tt}	Martinelli parameter with both phases turbulent, [−]
z	longitudinal coordinate, [m]
Z	parameter for Shah's correlation

Greek symbols

α	heat transfer coefficient, [W/(m^2·K)]
γ	tube tilt angle, [°]
δ	liquid film thickness of annular ring, [m]
Δ	variation, [−]
ε	void volume fraction, [−]
θ	falling film angle, [°]
λ	thermal Conductivity, [W/(m·K)]
μ	kinematic viscosity, [Pa·s]
ν	dynamic viscosity, [m^2/s]
ξ	El Hajal's map factor, [−]
ρ	density, [kg/m^3]
σ	surface tension, [N/m]
ϕ	radial coordinate, [°]
τ	shear stress, [Pa]

Subscripts

$1Ph$	single-phase
Bc	boundary curve
$bubbly$	bubbly flow
c	convective condensation, Critical
cal	calibrated
$calc$	calculated
con	conduction
$cond$	condensation
d	dimensionless
Et	Empty tube
exp	experimental
ext	external
f	frictional
$film$	film
h	hydrostatic
i	generic section
IA	intermittent to annular flow
in	inlet
ins	inside
int	internal
k	related to the respective phase
L	liquid
LO	liquid only
loc	local
m	mean
$mist$	mist flow
ml	mean logarithmic
mod	modified
oil	oil
out	outlet
$prop$	propylene
r	relative
raw	raw

sat	saturated
$strat$	stratified flow
sub	substance
tot	total
tp	two-phase
tt	turbulent-turbulent
V	vapor
VO	vapor only
$wall$	surface
$wavy$	wavy flow
ρ	acceleration

Dimensionless numbers

Bo	Bond number
Eu	Euler number
Fr	Froude number
Nu	Nusselt number
Pr	Prandtl number
Re	Reynolds number

List of Figures

List of Tables

1. Introduction

In the context of rising global energy demand, research in the energy sector is concerned with optimizing existing process technologies to minimize the impact on climate change. In this regard, thermal processes such as evaporation and condensation are particularly interesting because high heat flux densities can be transferred with very low temperature differences, so that exergy destruction is kept low.

Film-wise condensation is a thermal process that occurs when a fluid in the gaseous state comes in contact with a surface, whose temperature is lower than the saturation temperature of the fluid at the present thermodynamics' conditions. During the process, the condensing fluid rejects latent heat to the environment; often, in industrial applications, heat is absorbed by a cooling fluid. Under ideal conditions (isobaric), the condensation of a pure fluid occurs at constant temperature. Condensers are adopted in both direct cycles for power plants [1] and reverse cycles for refrigeration purposes [2]. Furthermore, condensation is widely used in desalination processes [3]. Among the listed applications, refrigeration industry is facing an important period of change. In fact, the nowadays broadly used HFC and HFO, are being progressively replaced by alternative refrigerants. Among these new refrigerants, hydrocarbons, like propylene (R1270) studied in the present work, will play a key role in the future for their null ODP and very small GWP.

In literature, several articles analyze and assess condensation of different fluids in different configurations.

The analysis of two-phase flow condensation is particularly complex since many variables are involved in the heat transfer mechanism. For this reason, no analytical equations are available and thus, experts need to rely on empirical or semi-empirical correlations that have been proposed by researchers in the past. The estimation of the heat transfer coefficient α and of the pressure drops $\left(\frac{\Delta p}{\Delta L}\right)_{tp}$ is further complicated by the

existence of several possible condensation flow patterns inside horizontal tubes.

The purpose of this work is to analyze condensation of a pure hydrocarbon (propylene) inside a horizontal smooth tube. In particular, the scope is that of evaluating the local heat transfer coefficients around the tube circumference and at different cross sections. The experimental work consists in the acquisition of data under several test conditions (pressure p, vapor quality x, mass flux G) and flow regimes. The work will cover the process of equipping the test tube, including the installation of the thermocouples, and the comparison of the experimental data with correlations found in the literature.

The experimental work has been carried out at the “Institute of Technical Thermodynamics” at the University of Kassel. The department features an industrial scale test rig to provide realistic conditions and to carry out tests in partial condensation, varying the operating conditions. The experimental apparatus also allows to properly adjust the thermodynamic conditions of both the test substance and the cooling oil at the inlet of the test section.

2. Theoretical basis

Flow condensation is a widely used process; a better understanding and evaluation of this phase change phenomenon is important for the enhancement of energy production and use. Differently from single-phase heat transfer, condensation occurs in the simultaneous presence of two phases, the liquid phase, and the gaseous phase. In the case of condensation inside a horizontal tube, the formation of condensate leads to the formation of a liquid film. Depending on the flow conditions, this film can take various forms inside the tube. It is evident that the determination of the film thickness, its shape, and the interaction between the two phases within the tube are important to describe the heat transfer mechanism.

The interaction of the two phases depends, among other parameters, on substance properties such as density ρ and dynamic viscosity μ as well as the occurring flow conditions and the pipe geometry [4] [5] [6].

The empirical and semi-empirical models used in the literature to calculate the heat and momentum transfer accurately, assume the knowledge of the flow regime. Once set the flow conditions, flow pattern maps are able to predict the flow pattern occurring inside the tube.

2.1 Flow regimes and flow pattern maps

Depending on mass flux G, on flow velocity u on the vapor quality x, on tube geometry and orientation, several flow regimes can verify inside a horizontal tube.

The two-phase flow is governed by the action of 3 different, simultaneously operating forces, which are:

1) *Inertial forces mainly associated to vapor velocity*
   The inertial forces induced by the gas phase perturb the liquid phase, applying shear stress forces τ.

2) *Adhesive/surface tension forces that act on the liquid-vapor interface*
   The adhesive forces, proportional to the surface tension, tend to mitigate and counteract the inertial forces.
3) *Gravity force*
   The gravity force tends to push the liquid phase on the bottom of the tube, having a higher density ρ than the gaseous phase.

The combination of these 3 forces determines the two-phase flow regime. The intensity of the 3 mentioned forces is a function of mass flow rate $\dot{m}$, velocity u, vapor quality x, density ρ and viscosity μ of the phases, tube roughness and geometry.
The mutual comparison between the three forces previously listed is customarily described by dimensionless numbers.

1) Reynolds number (Re) is defined as the ratio between the inertial force and the viscous one.

$$Re = \frac{ul}{\nu} = \frac{\rho u l}{\mu} \tag{2.1}$$

2) Froude number (Fr) is defined as the ratio between the inertial force and the gravity one.

$$Fr = \frac{u}{\sqrt{gl}} \tag{2.2}$$

3) Weber number (We) is defined as the ratio between the drag (inertial) force and the cohesion one.

$$We = \left(\frac{8}{C_D}\right)\frac{\left(\frac{\rho u^2}{2} C_D \pi \frac{l^2}{4}\right)}{(\pi l \sigma)} = \frac{\rho u^2 l}{\sigma} \tag{2.3}$$

4) Bond (Bo) or Eötvös (Eo) number is defined as the ratio between the gravity force and the surface tension one.

$$Bo = \frac{\Delta\rho g l^2}{\sigma} \tag{2.4}$$

5) Euler number (Eu) is defined as the ratio between the pressure forces and the inertial forces.

$$Eu = \frac{\Delta p}{\rho U^2} \tag{2.5}$$

The simultaneous action of inertial, surface tension and gravity forces can give rise to several different flow regimes, listed below.

Bubble flow: The liquid phase lays on the lower part of the tube while gas bubbles travel along the tube, tending to stay on the upper part of the tube because of their smaller density ρ.
Plug flow: This flow regime is similar to the previous one, but the vapor bubbles are bigger and starts to congregate.
Stratified flow: The two phases are separated with a smooth interface, with the liquid laying in the lower part and the gas in the upper one.
Wavy flow: As vapor velocity increases, the interface between the two phases is disturbed by waves travelling in the direction of the flow.
Slug flow: This flow regime is similar to the previous one but, being the vapor velocity higher, waves become bigger, and they touch the upper part of the tube.
Annular flow: In this configuration, the gas flows in the center of the tube, while the liquid remains in contact with the inner diameter of the tube under the shape of a film.

Inside a horizontal tube, vapor travels in the same direction of the condensate. If the vapor travels at relatively low speed u_V, the flow is mainly regulated by gravity and the flow is stratified. If the vapor travels at high speed, it exerts a tangential stress on the liquid film, tearing drops out from the liquid layer, reducing the thickness of the film. The shear stress [7],

$$\tau_V = \frac{f_V G_V^2}{2\rho_V} \tag{2.6}$$

exerted by the vapor on the liquid, is proportional to the squared vapor mass velocity G_V. When the force, due to the shear stress, in the axial direction, is much greater than the force due to gravity in the vertical direction, the flow is ruled by the inertial forces. In these conditions, the effect of gravity is negligible on the thickness of the condensate film and the flow regime is annular or annular mist. The thickness of the film and therefore the heat transfer coefficient α are controlled by vapor velocity u_V, which progressively decreases as the test substance condenses along the tube.

A representation of the flow regimes is reported down below, in Fig. 2.1 [8].

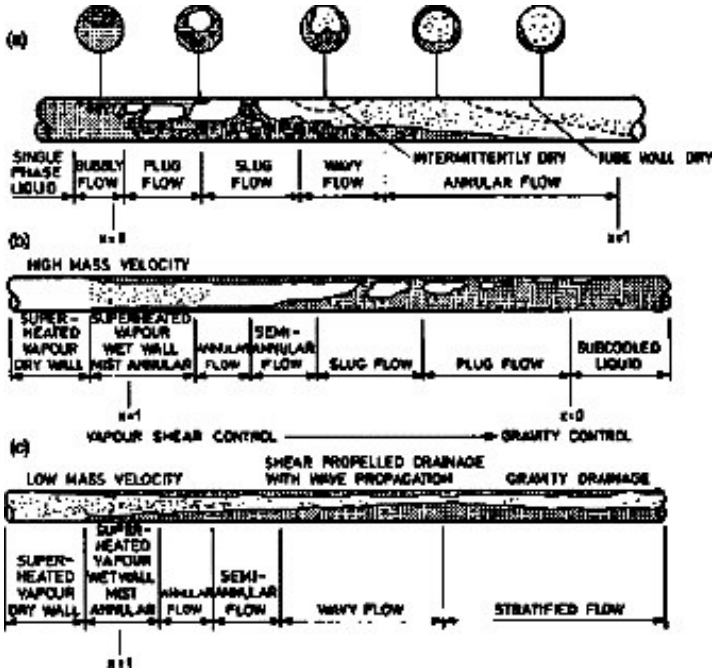

FIGURE 2.1 - CONDENSATION FLOW REGIMES [8] EL HAJAL

To determine the flow form, a basic distinction is made between diabatic and adiabatic flow forms [9].

Steiner [10] proposes a flow map for two-phase flow in horizontal tubes under adiabatic conditions. Steiner's flow map, like the flow map of

Breber et al. [11], is based on the analytical model of Taitel and Dukler [12]. Steiner [10] transfers the model of Taitel and Dukler [12] for flow boiling to condensation. For this purpose, the calculated boundary curves of Taitel and Dukler [12] are validated with the help of experimental data of hydrocarbons and refrigerants, so that the flow map according to Steiner [10] is adapted for low-boiling and normal-boiling fluids. In contrast to the flow map of Taitel and Dukler [12] and Breber et al. [11], the model of Steiner [10] considers the mist flow condition. Figure 2.2 shows the flow map according to Steiner [10]. The map displays the Martinelli parameter X_{tt} on the x-axis and the parameter $(Re_L Fr_V)^{0.5}$ on the y-axis.

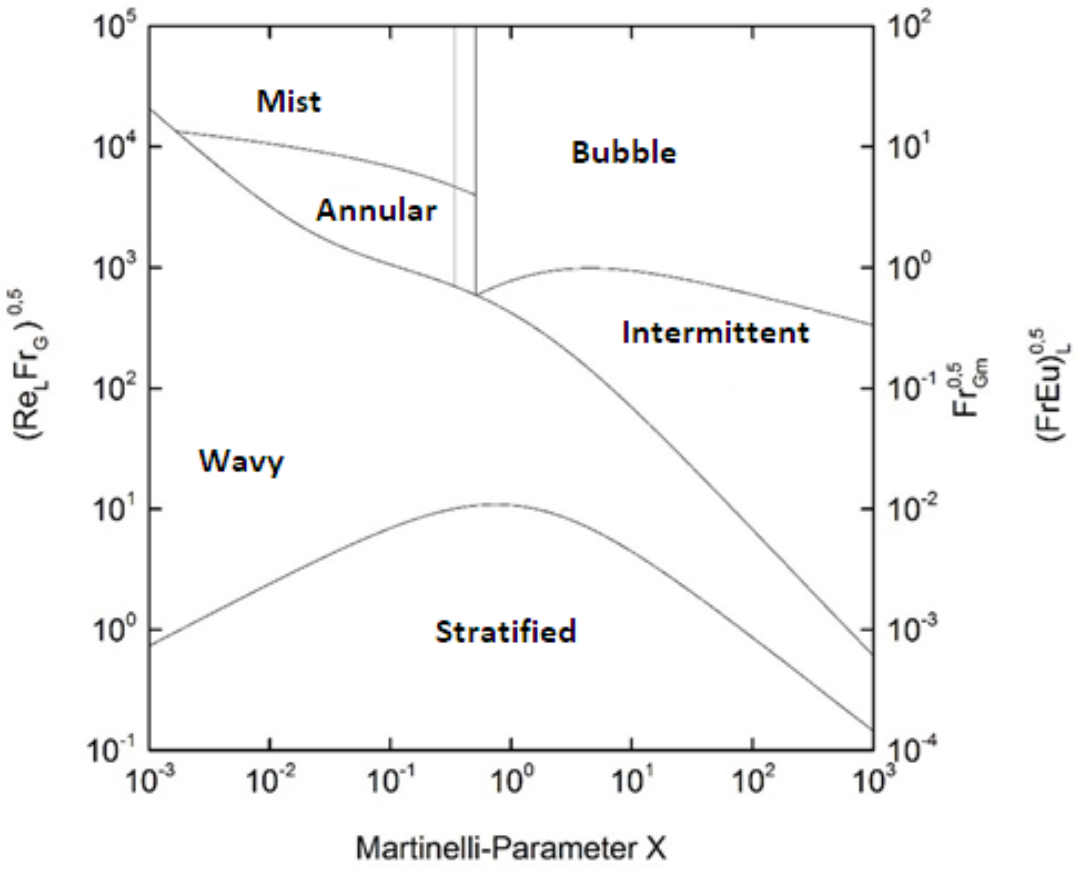

FIGURE 2.2 - FLOW PATTERN MAP ACCORDING TO STEINER [10] FOR A HORIZONTAL PIPE FLOW

To determine the flow form, Lockhart-Martinelli's parameter is firstly determined according to Eq. (2.7)

$$X_{tt}{}^2 = \left[\left(\frac{\tilde{u}_V + \tilde{u}_i}{\pi}\right)^{0,25}\left(\frac{\pi^2}{64\tilde{A}_V^2}\right)\left(\frac{\tilde{u}_V}{\tilde{A}_V} + \frac{\tilde{u}_i}{\tilde{A}_L} + \frac{\tilde{u}_i}{\tilde{A}_V}\right) - \frac{1}{(Fr\ Eu)_V}\right] * \left(\frac{\pi}{\tilde{u}_L}\right)^{0,25}\left(\frac{64\tilde{A}_L^3}{\pi^2\tilde{u}_L}\right) \quad (2.7)$$

with

$$(FrEu)_V = \frac{f_{V,Et}(Gx)^2}{2\ d\ g\ \rho_V(\rho_L - \rho_V)\ sin\,\gamma} \quad (2.8)$$

as a function of the relative liquid height

$$\tilde{a}_L = \frac{a_L}{d}, \quad (2.9)$$

so calculated. For horizontal pipes ($\gamma = 0$), the calculated value from Eq. (2.8) becomes infinite, therefore, it can be neglected for Eq. (2.7). The calculation of the parameters used in Eq. (2.7) with a tilde (~) is done depending on the relative liquid height $\tilde{a}_L$, which is determined iteratively. A distinction is made between two cases in which the calculation of the dimensionless variables takes place as a function of the relative fluid height ($\tilde{a}_L \leq 0.5$ or $\tilde{a}_L > 0.5$).

Steiner [10] defines the boundary curves between the individual flow forms with the help of ratios of dimensionless numbers. As explained previously, these numbers are function of substance parameters such as the surface tension σ, the density ρ and the angle of inclination of the pipe γ. Table 2.1 shows the boundary curves of the flow pattern map according to Steiner [10] with the corresponding flow form transition.

TABLE 2.1 – BUONDARY CURVES EQUATIONS ACCORDING TO STEINER [10]

Flow form transition	**Boundary curve**

Stratified to wavy flow	$(Re_L Fr'_V)^{0,5}_{tt,Bc} = \left[\frac{(226,3)^2}{\pi^3}\tilde{A}_L \tilde{A}_V{}^2\right]^{0,5}$	(2.10)
Wavy to plug or surge flow	$(Fr_{Gm})^{0,5}_{tt,Bc1} = \left[\frac{16\tilde{A}_V{}^3}{\pi^2\sqrt{1-(2\tilde{a}_L-1)^2}} * \left[\frac{\pi^2}{25\tilde{a}_L^2}\left(\frac{Fr}{We}\right)_L + \frac{1}{cos\,\gamma}\right]\right]^{0,5}$	(2.11)
Bubble to plug or surge flow	$[(FrEu)_L]^{0,5}_{Bc} = \left[\frac{128\tilde{A}_V \tilde{A}_L{}^2}{\pi^2 \widetilde{U}}\right]^{0,5}$	(2.12)
Bubble flow to mist flow and annular flow	$X_{tt} = 0,51$	(2.13)
Fog to ring flow	$(Fr_{Vm})^{0,5}_{Bc2} = \left[\frac{7680\tilde{A}_V{}^2}{\pi^2 f_{tp}}\left(\frac{Fr}{We}\right)_L\right]^{0,5}$	(2.14)

The flow regimes are determined as a function of the following parameters,

$$(Re_{Fl}Fr_V')^{0,5} = \left(\frac{G^3 x^2 (1-x)}{\rho_V(\rho_L - \rho_V)\,\mu_L\, g\, cos\,\gamma}\right)^{0,5}, \tag{2.15}$$

$$Fr_{G,m}^{0,5} = \left(\frac{G^2 x^2}{\rho_L\, \rho_V\, g\, d}\right)^{0,5}, \tag{2.16}$$

$$((FrEu)_L)^{0,5} = \left(\frac{f_{L,Lr} G^2 (1-x)^2}{2d\, \rho_L\, (\rho_L - \rho_V)\, g\ \ cos\,\gamma}\right)^{0,5} \tag{2.17}$$

and the ratio of the Weber number (We) and the Froude number (Fr) of a pure liquid flow

$$\left(\frac{We}{Fr}\right)_L = \frac{g\, d^2\, \rho_L}{\sigma} \tag{2.18}$$

is calculated.

For the boundary curve of a mist or ring flow, the tube two-phase friction factor

$$f_{tp} = \left[1{,}138 + 2\, log\left(\frac{\pi}{1{,}5\, \tilde{A}_L}\right)\right]^{-2} \tag{2.19}$$

is calculated. Furthermore, the coefficient of friction for a single-phase liquid flow is so calculated,

$$f_{L,Et} = \frac{0{,}3164}{Re_{L,Et}^{0,25}} \tag{2.20}$$

as function of the Reynolds number of a single-phase liquid flow. After having calculated the dimensionless ratios according to Eq. (2.9) to Eq. (2.18) and the boundary curves equations, according to Steiner [10], certain conditions must be fulfilled for a certain flow form to occur.

If the condition

$$(Re_L Fr_V')^{0,5} \leq \left(Re_{L,s} Fr_V'\right)_{tt,strat}^{0,5} \tag{2.21}$$

is satisfied, the flow is stratified. Otherwise, with the condition

$$Fr_{V,m}^{0,5} \leq \left(Fr_{G,m}\right)_{tt,Bc1}^{0,5} \tag{2.22}$$

the presence of a wavy flow is verified. The condition for the occurrence of a bubble flow is described by Steiner [10] with

$$((FrEu)_L)^{0,5} \geq [(FrEu)_L]_{Bc}^{0,5}. \tag{2.23}$$

A surge or plug flow is present for

$$X_{tt} \geq 0{,}34 \text{ and } Fr_{V,m}^{0,5} > \left(Fr_{V,m}\right)_{tt,Bc1}^{0,5}. \tag{2.24}$$

If the condition

$$X_{tt} < 0{,}51 \text{ and } Fr_{V,m}^{0,5} > \left(Fr_{V,m}\right)_{Bc2}^{0,5} \tag{2.25}$$

is fulfilled, a fog flow occurs. If none of the previous conditions is satisfied, an annular flow is to be assumed. For $X_{tt} < 0.51$, the following condition applies for an annular flow:

$$\left(Fr_{V,m}\right)_{tt,Bc1}^{0,5} < Fr_{V,m}^{0,5} < \left(Fr_{V,m}\right)_{Bc2}^{0,5}. \tag{2.26}$$

Furthermore, it should be noted that the method described by Steiner [9] for determining the flow form is only valid for turbulent flows ($Re_{L,Et/G,Et} > 1187$).

The flow pattern map proposed by El Hajal et al. [8] is a modified version of that of Kattan et al. [13] for evaporation and adiabatic flows in small diameter horizontal tubes. The flow pattern map (Fig. 2.3), for R-134a in an 8.0 mm tube at a saturation temperature of 40 °C, shows the vapor quality x on the x-axis and the mass flux G on the y-axis. Flow patterns are classified as follows: fully stratified flow (S), stratified-wavy flow (SW), intermittent flow (I), annular flow (A), mist flow (MF) and bubbly flow (B).

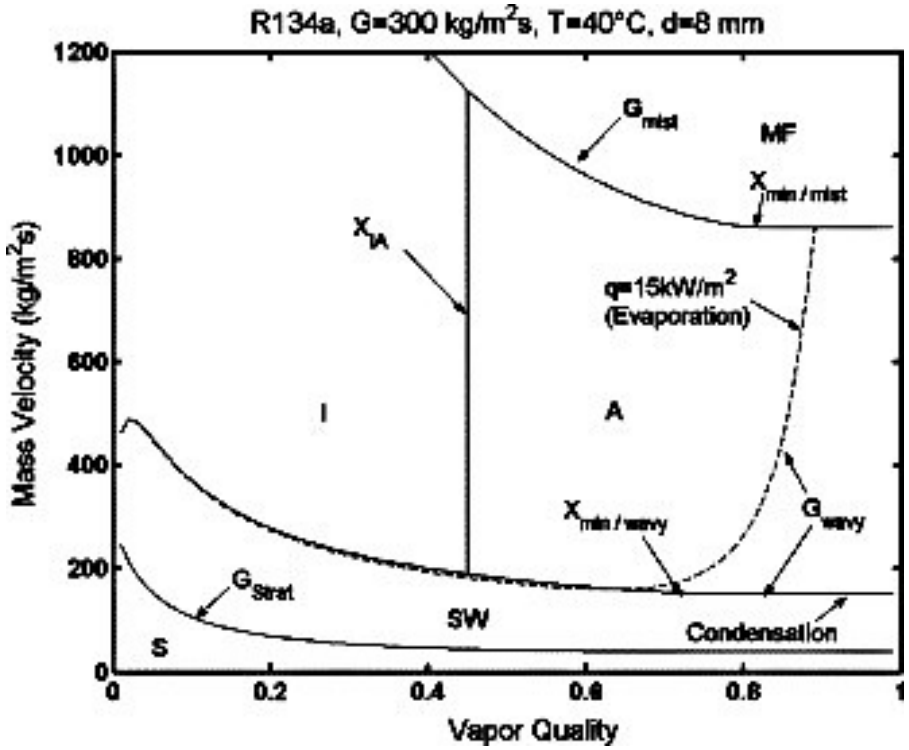

FIGURE 2.3 - FLOW PATTERN MAP PROPOSED BY EL HAJAL ET AL. [8]

Fig. 2.4 represents the geometrical dimensions of a stratified flow, where P_L is the stratified perimeter around the bottom of the tube, P_V is the non-stratified perimeter around the top of the tube, a_L is the height of the stratified liquid, P_i is the length of the interface, and A_L and A_V are the corresponding cross-sectional areas occupied by the liquid and vapor. The stratified angle θ_{strat} is the angle, which identifies the wet perimeter of the circumference.

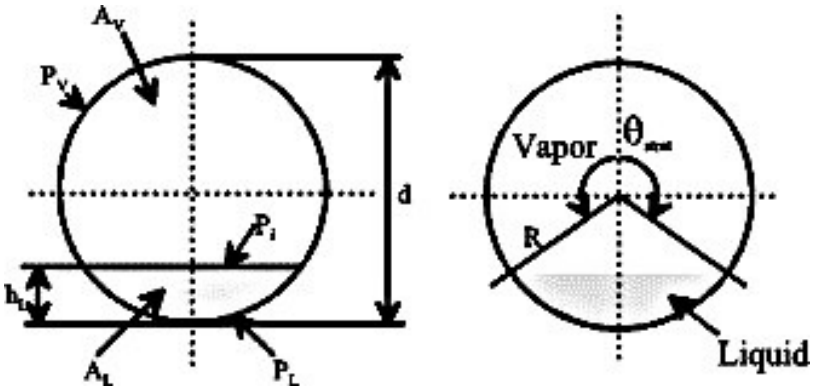

FIGURE 2.4 - GEOMETRICAL PARAMETERS FOR TWO-PHASE FLOW IN A CIRCULAR TUBE [8]

Some parameters are defined to calculate the transition curves of the map. Four variables are normalized using the tube internal diameter d to obtain four dimensionless variables:

$$a_{Ld} = \frac{a_L}{d}, \quad P_{id} = \frac{P_i}{d}, \quad A_{Ld} = \frac{A_L}{d^2}, \quad A_{Vd} = \frac{A_V}{d^2} \tag{2.27}$$

The stratified angle θ_{strat} is calculated by iterating the following geometrically defined equation:

$$A_{Ld} = \frac{1}{8}[(2\pi - \theta_{strat}) - sin\,(2\pi - \theta_{strat})] \tag{2.28}$$

The dimensionless liquid height can then be determined from the geometric expression:

$$a_{Ld} = 0.5\left(1 - cos\left(\frac{2\pi - \theta_{strat}}{2}\right)\right) \tag{2.29}$$

The geometric expression for P_{id}, as function of θ_{strat}, is

$$P_{id} = sin\left(\frac{2\pi - \theta_{strat}}{2}\right). \tag{2.30}$$

The transition curve from stratified-wavy flow to intermittent and annular flow for evaporation is determined using the following expression from Zurcher et al. [13] for G_{wavy}:

$$G_{wavy} = \left\{\frac{16A_{Vd}^3 g d \rho_L \rho_V}{x^2\pi^2(1-(2a_{Ld}-1)^2)^{0.5}}\left[\frac{\pi^2}{25a_{Ld}^2}(1-x)^{-F_1(q)} * \left(\frac{We}{Fr}\right)_L^{-F_2(q)}\right]\right\}^{0.5} + 50 - 75e^{-(x^2-0.97)^2/x(1-x)} \tag{2.31}$$

The non-dimensional empirical exponents accounting for the effect of heat flux on dry-out during evaporation are:

$$F_1(q) = 646.0\left(\frac{q}{q_{crit}}\right)^2 + 64.8\left(\frac{q}{q_{crit}}\right) \tag{2.32}$$

and

$$F_2(q) = 18.8\left(\frac{q}{q_{crit}}\right) + 1.023 \tag{2.33}$$

where the critical heat flux q_{crit} is used to normalize the local heat flux q. Since the heat flux effect on dry-out is not required for condensation

($q = 0$). Thus, the values of F_1 and F_2 become equal to 0 and 1.023, respectively.

Similarly, the transition curve from stratified-wavy flow to fully stratified flow is determined using the following expression from Zurcher et al. [14] for G_{strat}:

$$G_{strat} = \left\{\frac{(226.3)^2 A_{Ld} A_{Vd}^2 \rho_V (\rho_L - \rho_V)\mu_L g}{x^2(1-x)\pi^3}\right\} + 20x \qquad (2.34)$$

The transition between intermittent flow and annular flow is a vertical line given by x_{IA}, which is determined by setting the Martinelli parameter X_{tt} equal to 0.34, as

$$x_{IA} = \left\{\left[0.2914\left(\frac{\rho_V}{\rho_L}\right)^{-1/1.75}\left(\frac{\mu_L}{\mu_V}\right)^{-1/7}\right] + 1\right\}. \qquad (2.35)$$

This transition has a lower bound where it intersects the transition curve of G_{wavy}, as shown in Fig. 1, and has an upper bound where it intersects the transition curve of G_{mist}.

The transition curve from annular and intermittent flow to mist flow gives G_{mist} as

$$G_{mist} = \left\{\frac{7680 A_{Vd}^2 g d \rho_L \rho_V}{x^2 \pi^2 \xi}\left(\frac{Fr}{We}\right)_L\right\}^{0.5}. \qquad (2.36)$$

In the above equation, the ratio of the liquid Weber number We_L to the liquid Froude number Fr_L is

$$\left(\frac{We}{Fr}\right)_L = \frac{g d^2 \rho_L}{\sigma} \qquad (2.37)$$

and the factor ξ is

$$\xi = \left[1.138 + 2log\left(\frac{\pi}{1.5 A_{Ld}}\right)\right]^{-2}. \qquad (2.38)$$

Finally, the last transition is that to bubbly flow,

$$G_{bubbly} = \left\{\frac{256 A_{Vd} A_{Ld}^2 d^{1.25} \rho_L (\rho_L - \rho_V) g}{0.3164(1-x)^{1.75}\pi^2 P_{id} \mu_L^{0.25}}\right\} \qquad (2.39)$$

bubbly flow occurs at very high mass flux values, G.

The local flow pattern is determined as function of the tube diameter d, mass flux G, vapor quality x and the physical properties of the test substance.
To identify the flow pattern at a particular value of vapor quality x, the following logic is applied:

- Annular flow occurs if $G > G_{wavy}$, $G < G_{mist}$ and $x > x_{IA}$;
- Intermittent flow occurs if $G > G_{wavy}$, $G < G_{mist}$ or $G < G_{bubbly}$ and $x < x_{IA}$;
- Stratified-wavy flow occurs if $G_{strat} < G < G_{wavy}$;
- Fully stratified flow occurs if $G < G_{strat}$;
- Mist flow occurs if $G > G_{mist}$.

2.2 Two-phase heat transfer during condensation

The heat transfer coefficient for condensation is defined as a ratio,

$$\alpha_{cond} = \frac{\dot{Q}}{A \cdot (T_{sat} - T_{wall})}. \tag{2.40}$$

Given a fixed heat transfer area A, the heat transfer coefficient is proportional to the heat flow rate $\dot{Q}$ and inversely proportional to the temperature difference between the substance saturated temperature T_{sat} and the wall T_{wall}. It also corresponds to the reciprocal of the condensation thermal resistance R_{cond}. With reference to Eq. (2.40), in the present work, the determination of the heat flow rate $\dot{Q}$ is carried out assuming that the heat flux q only occurs in the radial direction, from the inner tube to the external annular tube where the coolant flows. Furthermore, in Eq. (2.40), the wall temperature T_{wall}, in our test, is the inner tube temperature, on which we have no information. In fact, the test tube is equipped with temperature sensors on the outer surface of the inner tube. For this reason, we cannot directly use eq. (2.40) to determine heat transfer coefficient. The methodology followed for this scope is reported in the Data Reduction, Chapter 4.

In 1916, Nusselt [15] developed an analytical theory for film condensation on a vertical wall. This theory assumes that motion is driven only by

gravity force. Unfortunately, since this and other Nusselt's assumptions are not verified in our case study, this theory cannot be used to calculate the heat transfer coefficient for two-phase flow condensation along a horizontal tube. Despite this, Nusselt's work has been useful to determine the dependencies of several key variables on the heat transfer coefficient α. In fact, numerous correlations valid for our application retain the dependencies discovered by Nusselt. The use of correlations instead of analytical models is necessary because of the dependence on flow shape, the unknown of temperature and flow fields [16], and the large number of variables influencing the mechanism. The heat transfer is mainly influenced by the flow velocity of vapor u_L [16]. At low vapor velocities u_L, a smooth or wavy layered flow is formed, so the heat transfer is mainly dominated by the gravity force [17] [18]. At high vapor velocities u_L, high shear forces τ act on the boundary layer between the two phases, consequently, an annular or turbulent flow develops [17] [18]. It can be said that the heat transfer occurs from the vapor to the liquid film through the interface between the two phases, and from the liquid film to the tube wall. Numerous models are proposed in literature to calculate the two-phase heat transfer coefficient for condensation.

Correlations often contain dimensionless numbers; we have already seen the ones that describe the flow regime. Now, the ones specifically related to heat transfer are presented.

1) Nusselt number (Nu) is defined as the ratio between convective heat transfer and conductive heat transfer across a boundary.

$$Nu = \frac{\alpha}{\lambda/L} = \frac{\alpha L}{\lambda} \tag{2.41}$$

2) Prandtl number (Pr) is defined as the ratio between momentum diffusivity and thermal diffusivity.

$$Pr = \frac{\mu/\rho}{\lambda/(c_p\rho)} = \frac{c_p\mu}{\lambda} \tag{2.42}$$

Thome et al. [19] proposed a general flow structure-based heat transfer model for condensation inside horizontal smooth tubes.
The study includes single component refrigerants, binary azeotropic or very near azeotropic refrigerant mixtures and pure hydrocarbons. The database covers a very broad range of conditions: mass velocities G from 24 to 1022 kg/(m^{2}s), vapor qualities x from 0.03 to 0.97, reduced pressures p^* from 0.02 to 0.80 and tube internal diameters d_{int} from 3.1 to 21.4 mm. Thome et al. [19] calculate the heat transfer coefficients for stratified, stratified-wavy, annular, intermittent and mist flow regimes.
The proposed condensation model assumes three simplified geometries for describing annular flow, stratified-wavy flow and fully stratified-wavy flow, as shown in the Fig. 2.5.

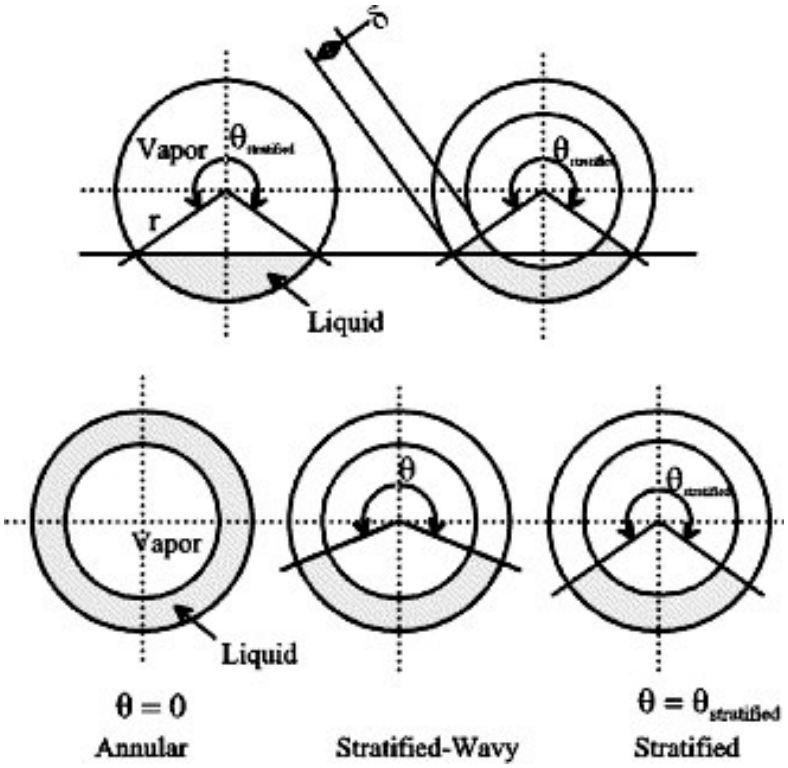

FIGURE 2.5 - SIMPLIFIED FLOW STRUCTURES FOR TWO-PHASE FLOW PATTERNS [19].

For annular flow, a uniform liquid film thickness is assumed, and the actual larger thickness of the film at the bottom compared to the top due to gravity is ignored. For fully stratified flow, an equivalent geometry is proposed, with the same angle of stratification θ and cross-sectional area occupied by the liquid of the actual one. As shown in Fig. 2.4, the liquid is

assumed to be distributed as a truncated annular ring of uniform thickness. Thome et. al [19] assume that two types of heat transfer mechanisms occur within the tube: convective condensation and film condensation. In this case, convective condensation refers to the axial flow of the condensate along the channel due to the imposed pressure gradient, while film condensation refers to the flow of condensate from the top of the tube towards the bottom due to gravity.

The two heat transfer mechanisms are applied to their respective heat transfer surface areas as shown in Fig. 2.6.

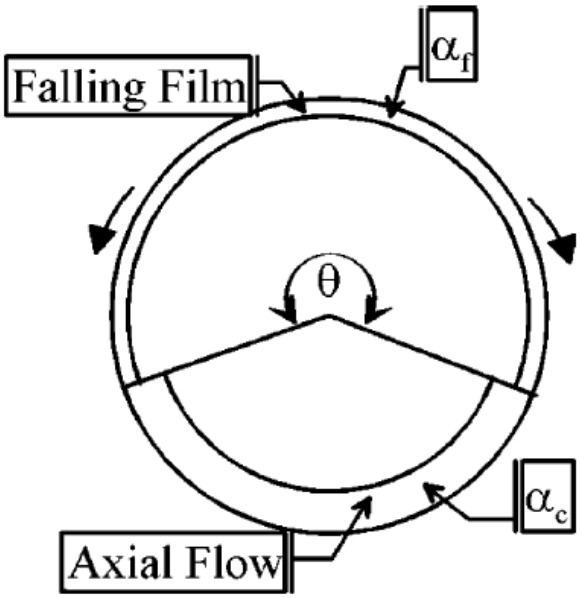

FIGURE 2.6 - HEAT TRANSFER MODEL SHOWING CONVECTIVE AND FALLING FILM BOUNDARIES [19].

The convective condensation heat transfer coefficient α_c is applied to the perimeter wetted by the axial flow of liquid film.
Film condensation heat transfer coefficient α_{film} is applied to the upper perimeter of the tube for stratified-wavy and fully stratified flows.

The general expression for the local two-phase heat transfer coefficient α_{tp} is:

$$\alpha_{tp} = \frac{\alpha_{film} r\theta + (2\pi - \theta) r\alpha_c}{2\pi r} \tag{2.43}$$

The concept behind this equation consists in averaging two heat transfer coefficients accounting for the portion of tube circumference in which the two mechanisms are present.

In this expression, r is the internal radius of the tube and θ is the falling film angle around the top perimeter of the tube. Hence, for annular flow with $\theta = 0$, α_{tp} is equal to α_c. The stratified angle θ_{strat} is calculated from the following implicit geometric equation:

$$A_L = \frac{d^2}{8}[(2\pi - \theta_{strat}) - \sin(2\pi - \theta_{strat})] \tag{2.44}$$

where A_L is the cross-sectional area occupied by the liquid phase.
In the upper part of the tube, we have film condensation. Film condensation heat transfer coefficient α_{film} is obtained from the theory of Nusselt [14] for laminar flow of a falling film on the internal perimeter of the tube, where α_{film} is the mean heat transfer coefficient for this perimeter.

$$\alpha_{film} = 0.728\left[\frac{\rho_L(\rho_L - \rho_V)g h_{LV}\lambda_L^3}{\mu_L d(T_{sat} - T_w)}\right]^{1/4} \tag{2.45}$$

The heat transfer coefficient α_f is a function of the wall temperature difference while the convective one is not.

In the lower part of the tube, convective condensation occurs. The convective condensation heat transfer coefficient α_c is obtained from the following turbulent film equation,

$$\alpha_c = cRe_L^n Pr_L^m \frac{\lambda_L}{\delta} f_i \tag{2.46}$$

where, the interfacial roughness correction factor f_i is

$$f_i = 1 + \left(\frac{u_V}{u_L}\right)^{1/2}\left(\frac{(\rho_L - \rho_V)g\delta^2}{\sigma}\right)^{1/4} \tag{2.47}$$

function of the velocity of the two phases.

In 2016, Shah [20] proposed a heat transfer model to calculate the heat transfer coefficient for condensation inside tubes.
The model has been validated by comparison with a database that includes 33 fluids, tube diameters d from 0.10 to 49.0 mm, reduced pressures p^* from 0.0008 to 0.946, mass flux G from 1.1 to 1400 kg/(m^{2}s), various shapes and orientations.

The model is based on the definition of three regimes; the regimes are defined depending on the dimensionless vapor velocity,

$$J_V = \frac{xG}{\left(gd\rho_V(\rho_L - \rho_V)\right)^{0.5}} \tag{2.48}$$

and on the parameter Z,

$$Z = \left({}^{1}/_{x} - 1\right)^{0.8}(p^*)^{0.4}. \tag{2.49}$$

Regime 1 occurs when:

$$J_V \geq 0.98(Z + 0.263)^{-0.62} \tag{2.50}$$

Regime 3 occurs when:

$$J_V \leq 0.95(1.254 + 2.27Z^{1.249})^{-1} \tag{2.51}$$

If neither of the two conditions is verified, Regime 2 occurs.
The correlation uses two heat transfer equations,

$$\alpha_I = \alpha_{LO}\left(1 + \frac{3.8}{Z^{0.98}}\right)\left(\frac{\mu_L}{14\mu_V}\right)^{(0.0058+0.577p_r)} \tag{2.52}$$

where,

$$\alpha_{LO} = 0.023Re_{LO}^{0.8}Pr_L^{0.4}k_L/d_i \tag{2.53}$$

and,

$$\alpha_{Nu} = 1.32Re_{LO}^{-1/3}\left[\frac{\rho_L(\rho_L - \rho_V)g\lambda_L^3}{\mu_L^2}\right]^{1/3} \tag{2.54}$$

Equations (2.52) and (2.54) are properly combined to evaluate the two-phase heat transfer coefficient α_{tp} in the three regimes.
In Regime 1,

$$\alpha_{tp} = \alpha_I \tag{2.55}$$

In Regime 2,

$$\alpha_{tp} = \alpha_I + \alpha_{Nu} \tag{2.56}$$

In Regime 3,

$$\alpha_{tp} = \alpha_{Nu} \tag{2.57}$$

2.3 Calculation of the two-phase pressure loss

The calculation of pressure drops in a two-phase flow is complicated by the interaction between the two phases. The majority of the existing models in the literature are categorized in two different elementary approaches. In the homogeneous model, it is assumed that the gas and liquid phases have the same velocity $u_V = u_L$, so that the fluid mixture is treated as a single-phase fluid and the calculation of the pressure loss Δp is carried out with the existing relationships for single-phase flows. According to this approach, the substance and flow variables required for the calculation are average values from the variables of both phases [21] [22]. Despite the important insights provided by analytical models for two-phase pressure losses in conventional round pipes, models in the literature are largely based on empirical methods. The heterogeneous model approach assumes that gas and liquid flow separately through the pipe with different phase velocities $u_V \neq u_L$.

The total two-phase pressure loss in a pipe,

$$\Delta p_{tot} = \Delta p_f + \Delta p_h + \Delta p_\rho \tag{2.58}$$

is calculated as the sum of the contributions of the frictional pressure loss Δp_f, the hydrostatic pressure loss Δp_h due to a change in height a, and the acceleration pressure loss Δp_ρ due to the partial phase change across the tube. In the case of a horizontal pipe flow, the hydrostatic pressure loss,

$$\Delta p_h = (\rho_L - \rho_V) g a \sin\gamma \tag{2.59}$$

is negligible due to the null height change along the tube. The acceleration pressure loss Δp_ρ accounts for a change in the volume flow due to a partial phase change during the condensation process within the flow. The acceleration pressure loss in a pipe section

$$\Delta p_\rho = G^2 \left\{ \left[\frac{(1-x)^2}{\rho_L(1-\varepsilon)} + \frac{x^2}{\rho_G \varepsilon} \right]_2 - \left[\frac{(1-x)^2}{\rho_L(1-\varepsilon)} + \frac{x^2}{\rho_G \varepsilon} \right]_1 \right\} \tag{2.60}$$

is determined as a function of the mass flux G, the densities of the two phases ρ as well as the vapor content x and the void volume fraction ε. This variable,

$$\varepsilon = \frac{x}{\rho_G} \left[\left(1 + 0{,}12(1-x)\right) \left(\frac{x}{\rho_G} + \frac{1-x}{\rho_L} \right) + \frac{1{,}18(1-x)\left(g\sigma(\rho_L - \rho_G)\right)^{0{,}25}}{G\ \rho_L^{0{,}5}} \right]^{-1} \tag{2.61}$$

is so calculated [23].

In the case of condensation, the acceleration pressure loss Δp_ρ is actually a pressure recovery, being the density of the liquid ρ_L higher than the one of the gaseous phase ρ_V.

In the literature, various approaches to calculate the two-phase friction pressure loss Δp_f for a horizontal pipe flow have been published, distinguishing between adiabatic and diabatic flows.

Lockhart and Martinelli [24] described a method according to which the adiabatic two-phase friction pressure loss Δp_f is calculated using the two-phase multiplier, one related the liquid phase,

$$\Phi_L^2 = 1 + \frac{C_{LM}}{X_{tt}} + \frac{1}{{X_{tt}}^2} \tag{2.62}$$

and one related to the gaseous phase,

$$\Phi_V^2 = 1 + C_{LM} X_{tt} + {X_{tt}}^2 \tag{2.62}$$

where, C_{LM} is an experimentally derived parameter that takes different values according to the liquid and vapor flow regime. In particular,

$C_{LM} = 20$ with turbulent liquid phase and turbulent gas phase.

$C_{LM} = 12$ with laminar liquid phase and turbulent gas phase.

$C_{LM} = 10$ with turbulent liquid phase and turbulent gas phase.

$C_{LM} = 5$ with laminar liquid phase and laminar gas phase [25].

While X_{tt} is the Martinelli parameter,

$$X_{tt} = \sqrt{\frac{\left(-\frac{dp}{dz}\right)_{f,L}}{\left(-\frac{dp}{dz}\right)_{f,V}}} \tag{2.63}$$

is function of the ratio of the frictional pressure drop $\left(-\frac{dp}{dz}\right)_{f,k}$ of each phase if it was flowing alone inside the tube with its respective mass flow rate $\dot{m}_k$.

The two-phase multipliers Φ_L and Φ_G describe the influence that the flow of each phase has on the other one in terms of pressure losses. In the model, the initial flow is treated as single-phase, so that the friction pressure loss per unit of length $\left(\frac{\Delta p_f}{\Delta L}\right)_k$ of each phase can be calculated, according to Kast [26],

$$\left(\frac{\Delta p_f}{\Delta L}\right)_k = f_k \frac{\rho_k u_k^2}{2d} \tag{2.65}$$

as a function of the fluid density ρ, the friction factor f, the flow velocity u and the pipe diameter d.

The two-phase friction pressure loss is thus calculated according to:

$$\left(\frac{\Delta p}{\Delta L}\right)_{tp,f} = \left(\frac{\Delta p}{\Delta L}\right)_V \cdot \Phi_V^2, \tag{2.66}$$

$$\left(\frac{\Delta p}{\Delta L}\right)_{tp,f} = \left(\frac{\Delta p}{\Delta L}\right)_{L} \cdot \Phi_L^2. \tag{2.67}$$

The two-phase multipliers, Φ_L and Φ_V, which allow to calculate the frictional pressure loss $\left(\frac{\Delta p}{\Delta L}\right)_{tp,f}$ of the two-phase flow as a function of the two single-phase pressure losses, $\left(\frac{\Delta p}{\Delta L}\right)_{V}$ and $\left(\frac{\Delta p}{\Delta L}\right)_{L}$, are taken up again in the Friedel's model [27]. Friedel's correlation for calculating the friction pressure loss of a multiphase flow is developed with the help of a database consisting of 25000 measured data of various refrigerants, mixtures of water and gases as well as oils and air and liquid metals. The model enables the calculation of the friction pressure loss for an adiabatic horizontal raw flow. To determine a two-phase multiplier R_F, the density ρ and the dynamic viscosity μ of the two phases are required. Furthermore, the pipe friction factor f_k of the respective phase is calculated as a function of the Reynolds number Re. The validity range of the correlation is given for a viscosity ratio $\frac{\mu_L}{\mu_V} < 1000$ and a mass flux $G > 100\ \frac{kg}{m^2 s}$.

The frictional two-phase pressure drop is calculated as,

$$\left(\frac{\Delta p}{\Delta L}\right)_{tp,f} = \left(\frac{\Delta p}{\Delta L}\right)_{1Ph,L} \cdot R_F \tag{2.68}$$

thanks to the two-phase multiplier R_F.

All the required equations are reported in the table down below (Tab. 2.2).

TABLE 2.2 – FRICTIONAL TWO-PHASE PRESSURE DROPS ACCORDING TO FRIEDEL [27]

Friedel [27]	$(\Delta p/\Delta L)_{tp,f} = (\Delta p/\Delta L)_{1Ph,L} \cdot R_F$	(2.69)
	$(\Delta p/\Delta L)_{1Ph,L} = \frac{f_{1Ph,L} \cdot G^2}{2 d_H \rho_L}$	(2.70)

	$R_F = Z + 3{,}43x^{0{,}685}(1-\dot{x})^{0{,}24}(\rho_L/\rho_V)^{0{,}8}(\mu_V/\mu_L)^{0{,}22} \cdot \left(1-(\mu_V/\mu_L)\right)^{0{,}89} {Fr_L}^{-0{,}047} {We_L}^{-0{,}0334}$	(2.41)
	$Z = (1-x)^2 + x^2\left(\frac{\rho_L \cdot f_{1Ph,V}}{\rho_V \cdot f_{1Ph,L}}\right)$	(2.72)
	If $Re_{1Ph,k} \leq 1055$, $f_{1Ph,k} = 64/Re_{1Ph,k}$	(2.73)
	If $Re_{1Ph,k} > 1055$, $f_{1Ph,k} = \left[0{,}86859\left(\frac{Re_{1Ph,k}}{\left(1{,}964 \cdot \ln(Re_{1Ph,k}) - 3{,}8215\right)}\right)\right]^{-2}$	(2.74)

Muller-Steinhagen et al. [28] proposed a method to calculate the frictional pressure drop $\left(\frac{\Delta p}{\Delta L}\right)_{tp,f}$ for two-phase flow inside pipes. To determine its reliability, the proposed correlation was checked against a database containing 9300 frictional pressure drop measurements for a large variety of fluids and flow conditions.

Considering the frictional pressure drop of the single phases:

$$\left(\frac{dp}{dz}\right)_{f,L} = f_L \frac{\dot{m}^2}{2\rho_l d} = M \tag{2.75}$$

$$\left(\frac{dp}{dz}\right)_{f,V} = f_V \frac{\dot{m}^2}{2\rho_g d} = N \tag{2.76}$$

with,

$$f_L = \frac{64}{Re_L} \text{ and } f_V = \frac{64}{Re_V} \text{ if } Re_L, Re_V \leq 1187,$$
$$f_L = \frac{0.3164}{Re_L^{1/4}} \text{ and } f_V = \frac{0.3164}{Re_V^{1/4}} \text{ if } Re_L, Re_V > 1187. \tag{2.77}$$

The two-phase friction pressure drop is calculated as

$$\left(\frac{dp}{dz}\right)_{tp,f} = S(1-x)^{1/P} + Nx^{P} \tag{2.78}$$

Where the parameter P is equal to 3 and the parameter S is so defined:

$$S = M + 2(M-N)x \tag{2.79}$$

In Fig. 2.7, the two-phase differential friction pressure drop $\left(\frac{dp}{dz}\right)_f$ is reported, on the y-axis, as function of the vapor quality x, on the x-axis, for air-water mixture, $G = 200\ kg/(m^2 s)$ and a pressure range $p = 1.2 - 1.6\ bar$. The measured values marked with circles, squares, and triangles, for different tube diameters d, are compared to the calculated pressure drop is identified by the solid line.

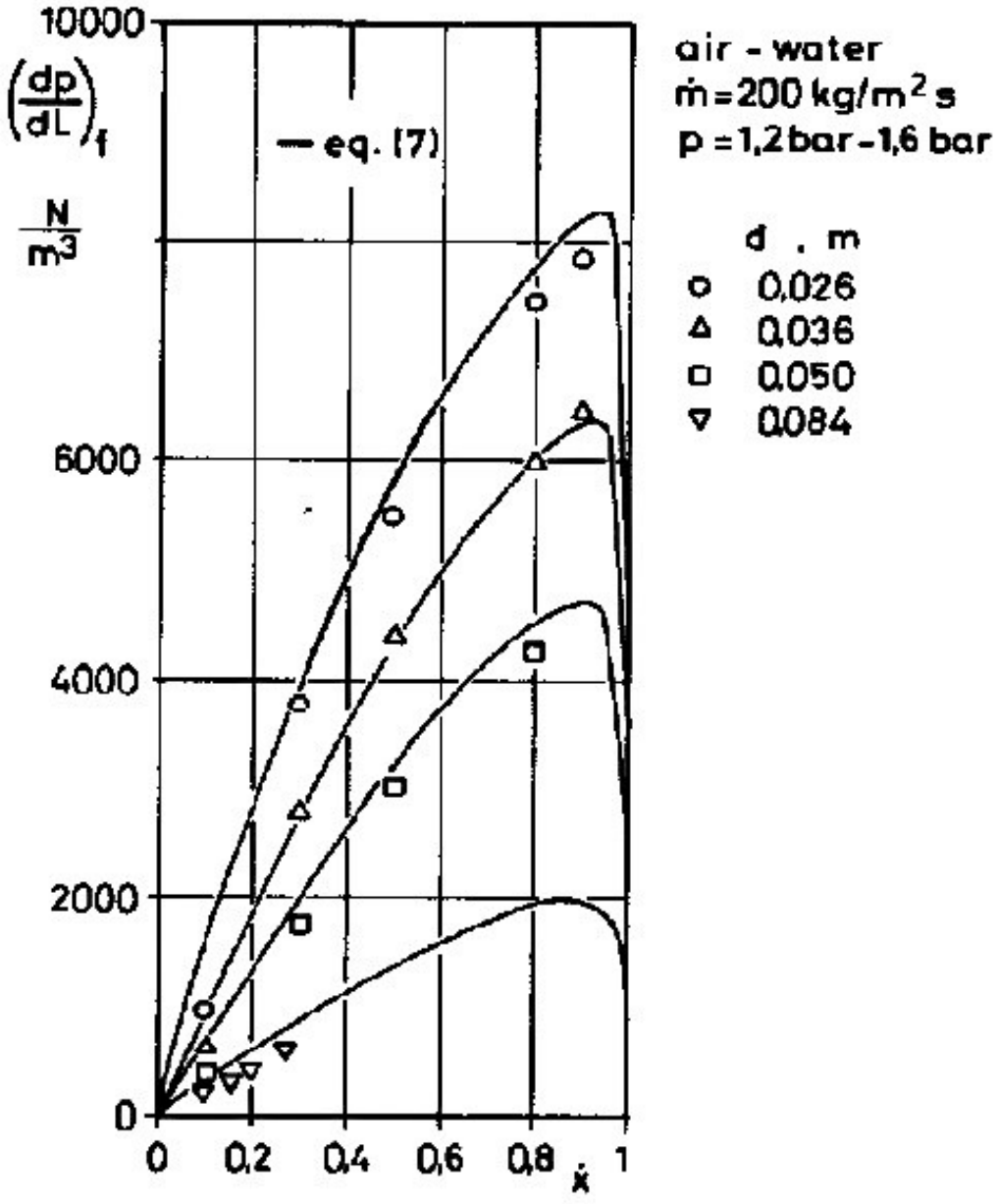

FIGURE 2.7 – MEASURED AND CALCULATED PRESSURE DROP OF WATER AND AIR AS FUNCTION OF VAPOR QUALITY PROPOSED BY MULLER-STEINHAGEN [28].

3 Experimental set up

The KIIR experimental apparatus is placed inside the laboratory of the Technical Thermodynamics department (TTK) of the University of Kassel. This facility has been built to run experimental tests regarding flow condensation. The experimental tests are implemented setting the operative parameters and recording the variables of interest.

In this chapter, the test rig is described, the equipment and installation of the tube-shell-heat in the facility are explained and the characteristics of the sensors used are presented.

The system, shown in detail in Figure 3.1, consists of several parts:

- A primary cycle, which includes the test section.
- A bypass cycle.
- Four secondary cycles, one of them involved in the test section.

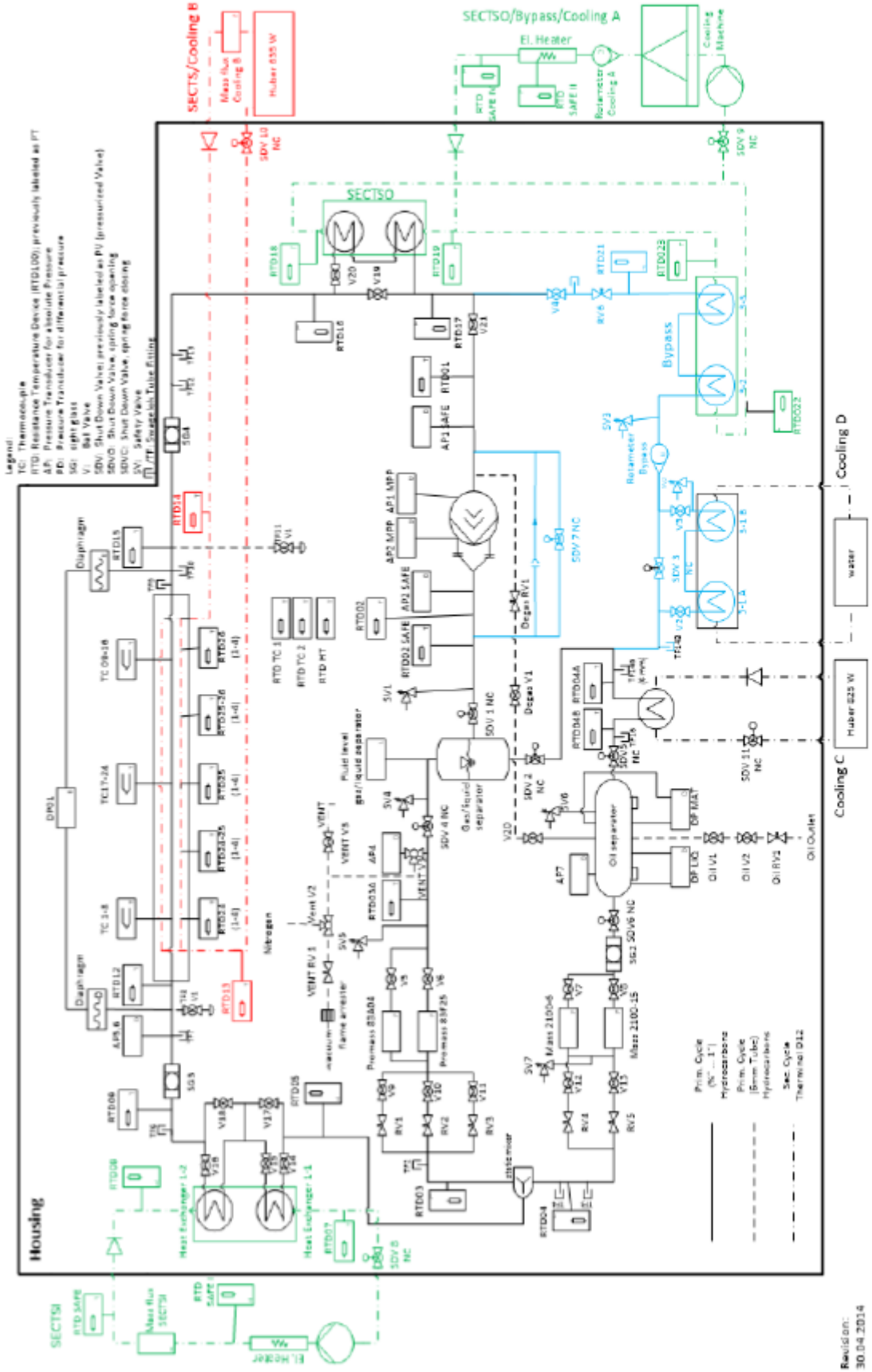

FIGURE 3.1 - DETAILED REPRESENTATION OF THE EXPERIMENTAL APPARATUS

3.1 Primary Cycle

The primary cycle is the principal loop of the experimental set up, indeed, the test tube is placed in this cycle. Propylene flows inside this loop. A schematic representation of the system is presented in Figure 3.2, and the designation of the main components is reported in Table 3.1.

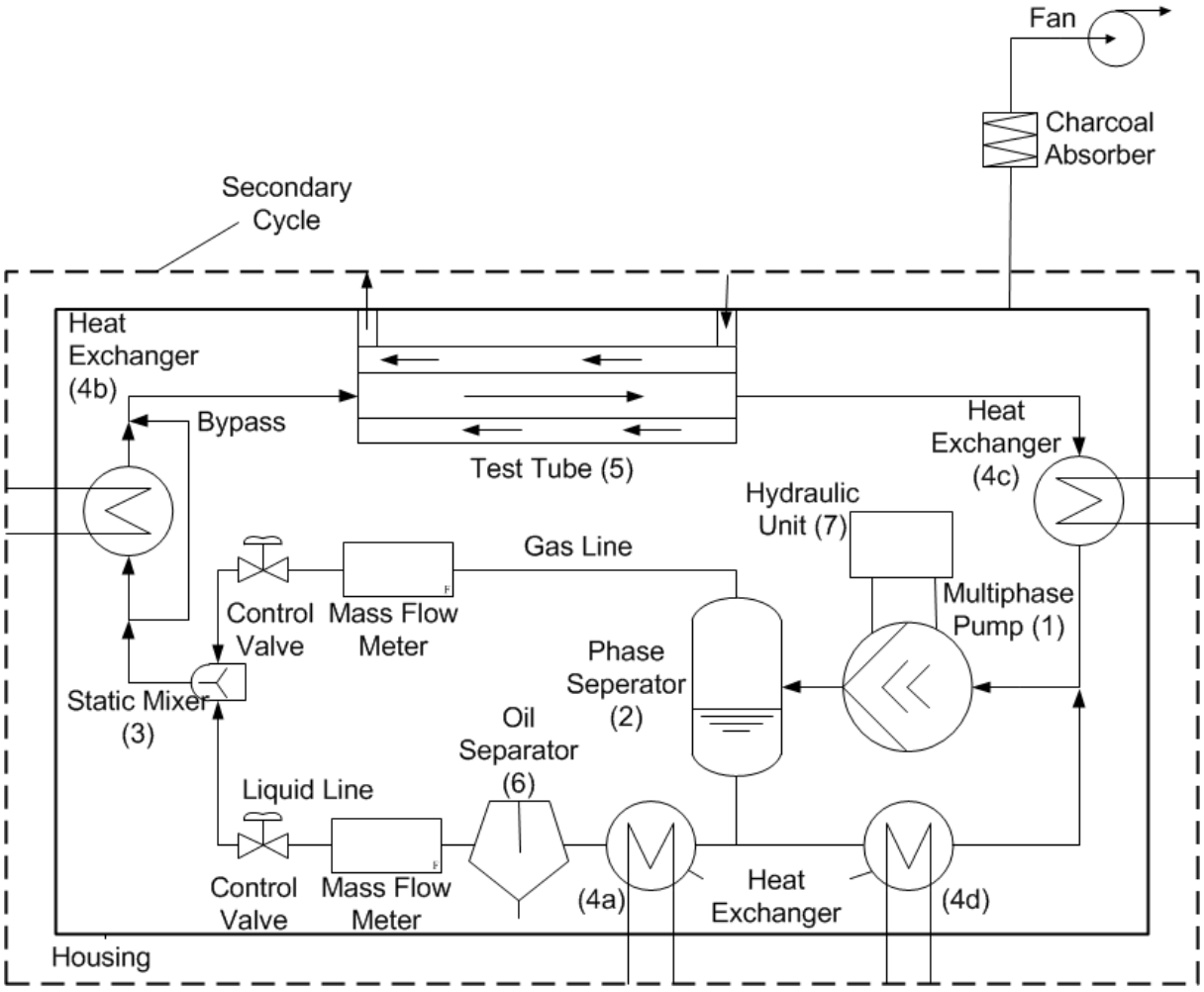

FIGURE 3.2 – SCHEMATIC REPRESENTATION OF THE EXPERIMENTAL APPARATUS

TABLE 3.1 – COMPONENTS' DESIGNATION OF THE PRIMARY CIRCUIT

Number	***Component***
1	Multi-phase pump
2	Liquid-vapor separator
3	Static mixer
4(a), 4(b), 4(c), 4(d)	Heat exchangers
5	Test tube
6	Oil separator
7	Hydraulic Unit

Propylene's flow is guaranteed by a prototype multi-phase screw pump, developed specifically for the present application. Differently from traditional pumps and compressors, this machine is able to elaborate two phases. This pump is suitable for low-viscosity fluids, and it has been designed to work under four specific conditions:

- The overall pressure difference between suction and discharge ports must be lower than 10 bar to avoid possible mechanical failures.
- The mass-based gas content at suction must be higher than 94% to avoid dangerous overheating during compression.
- The suction pressure must be higher than 0.5 bar to avoid the occurrence of cavitation.
- The rotational speed range is fixed between 400 and 1500 rpm. Adjusting the rotational velocity, it's possible to change the volumetric flow rate $\dot{V}$ in the primary cycle.

Downstream the pump, the fluid is sent to the phase separator (2), where the liquid-phase is separated from the gas-phase by gravitational effect. The liquid flows out from the outlet tube at the bottom of the separator, while the gas exits from the outlet tube at the top of the separator.

The liquid line splits in two at the outlet of the separator.

The first line leads to the by-pass section where a heat exchanger (4d) dissipates the heat produced by the pump. The purpose of this is to preserve the correct operative conditions of the pump. The presence of a valve allows to regulate the mass flow rate of liquid $\dot{m}_L$ at inlet of the pump. The second line guides the liquid towards the test section. Since the fluid is in saturated conditions at the outlet of the phase separator, a subcooling process of the liquid is necessary to avoid the occurrence of evaporation before the liquid enters the test tube. For this reason, along the liquid line, between the separator and the test tube line, there's a heat exchanger (4a). The downside of this procedure is that the liquid will enter the test tube in subcooled conditions and not in perfectly

saturated ones. After the heat exchanger, the liquid passes through an oil separator (6) to remove the lubricant oil traces collected while flowing inside the pump. The presence of the oil is undesired inside the circuit outside the pump. In fact, an excessive concentration of oil can significantly modify the fluid properties and, as consequence, undermine the experimental measurements. To better regulate the amount of fluid to send to the test tube, the liquid flows in two parallel pipes. Each pipe is equipped with a Coriolis flow meter to measure the liquid mass flow rate $\dot{m}_L$. Downstream to this measurement section, there are two control valves that regulate the mass flow in the static mixer (3), where the liquid and the gas pipes are reconnected.

Similar to the liquid line, after the two-phase separator (2), the gas line is split in three parallel pipes connected to the Coriolis flow meters and to the control valves to regulate the vapor mass flow rate $\dot{m}_V$, as already seen for the liquid lines. In the static mixer (3) the two lines converge and the desired fluid composition for the test section is provided. Before entering the test tube (5), the fluid can pass through a heat exchanger (4b). If this is not needed, the heat exchanger (4b) can be bypassed.

3.2 Secondary Cycles

In the test rig, four secondary loops are connected in parallel to the primary circuit, as depicted in Figure 3.2.
Their purpose is to properly modify the thermodynamics conditions of the primary fluid at different locations. These loops can include a heating machine, a pump, a heat exchanger, and a thermostat that controls the temperature of the secondary working fluid. Down below, a brief description of the four loops is provided:

- "Test Section Inlet Cycle" (*SECTSI*) (Heat exchanger (4b) in Fig. 3.2) is positioned upstream to the test section. Its purpose is to transfer heat to the working fluid in order to increase its temperature at the inlet of the test tube. In two-phase applications it can be used to control the vapor quality of the working fluid. This section is equipped with five valves that allow propylene to bypass the heat

exchanger fully or partially. Partial bypass is adopted with the purpose of reducing the pressure drop for high mass flows.

- "Test Section Cycle" (*SECTS*) hosts a heat exchanger connected at the outlet of the test tube. Its purpose is to cool down the oil, keeping constant the oil temperature at the inlet of the test section over time.
- "Test Section Outlet Cycle" (*SECTSO*) (Heat exchanger (4c) in Fig. 3.2) includes a heat exchanger, placed downstream to the test section. A bypass branch is included in case its utilization is not required.
- "Cooling C" (Heat exchanger (4a) in Fig. 3.2) consists in an additional heat exchanger able to perform the subcooling of the liquid phase, if needed.

3.3 Test Section

The test section consists of two concentric tubes: a circular cross section tube where propylene flows, and an annular shell tube where the cooling (Therminol D12) flows in counter-flow configuration with reference to propylene. The two tubes form a tube-shell-heat exchanger. The test section is shown in Fig. 3.3.

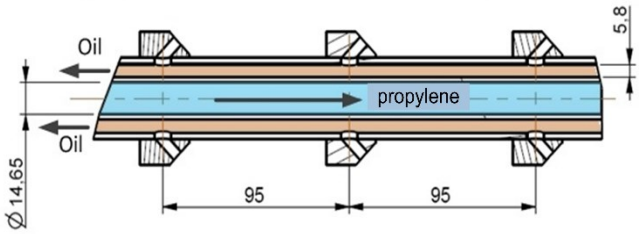

FIGURE 3.3 – COUNTER-FLOW CONFIGURATION PROPYLENE AND COOLING OIL

The internal tube is 3150 mm long, with an internal diameter d_{int} of 14.8 mm and an external diameter d_{ext} of 17.2 mm and it is wrapped by a shell tube, 2400 mm long, with a diameter d of 37 mm. The internal tube exhibits a smooth surface both inside and outside. The cooling oil flows inside the shell tube. A schematic representation is reported in Figure 3.4.

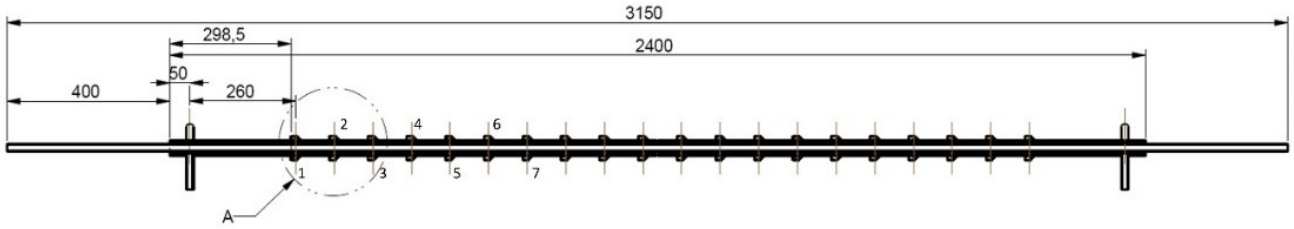

FIGURE 3.4 – SCHEMATIC REPRESENTATION OF THE TEST TUBE

The external tube is inserted into a compensating sleeve to avoid mechanical stress to the structure during operation of the entire system.
Both temperature T and pressure p of the primary fluid are acquired at the inlet and outlet of the test tube. In fact, in order not to disturb the flow and to have a better hydro thermodynamic behavior of the working fluid, there are no sensors inside the tube. The temperature of the secondary fluid is detected, within the test section, by 20 resistance thermometers (RTDs) threaded in the outer pipe and positioned in the center of the bulk flow. They are spaced by 95 mm from one to the other and they are positioned with a 180° offset in an alternated configuration, as shown in Figure 3.5.

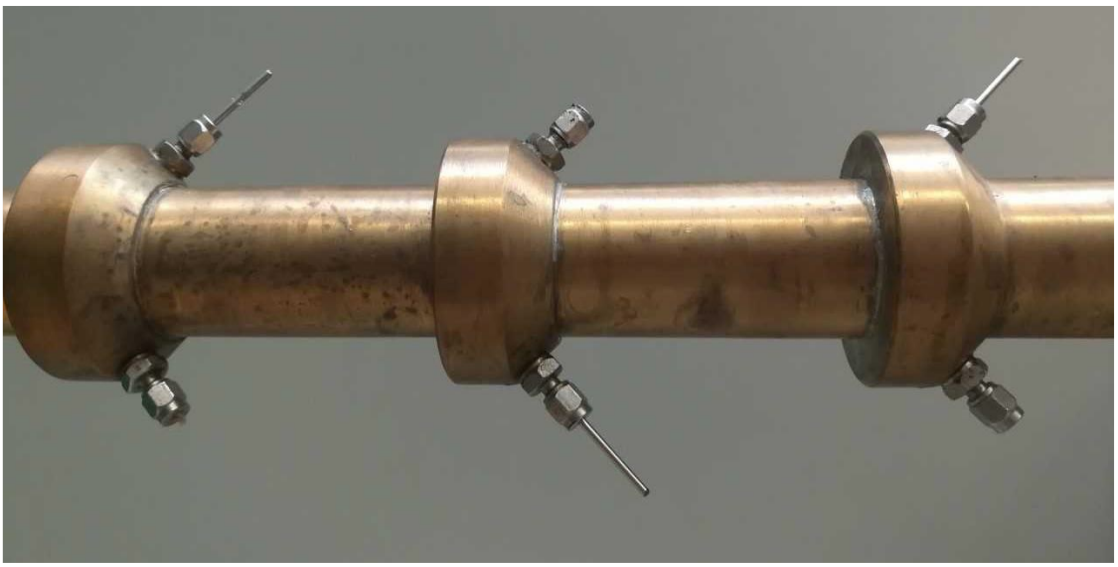

FIGURE 3.5 – RTD SENSORS DISPOSITION ON THE ANNULAR TUBE

The reason for this arrangement is to limit the errors in temperature measurements in case of the occurrence of turbulent flow inside the annular tube. The high amount of measuring sections allows to have an accurate picture of the temperature profile on the oil side.

It is worth to mention that the test section, on the oil side, is a part of the Test Section Cycle (*SECTS*). This secondary loop comprises of a cooling machine (Huber 635 W) and a bypass valve.
The cooling machine is utilized to cool down the heated oil returning from the test section while the bypass valve can be used to partialize the oil mass flow rate. By properly adjusting the mass flow rate, it's possible to set the oil temperature at the inlet of the test tube.
At the outlet of the cooling machine, before entering the test tube, the temperature (RTD14) $T_{oil,in}$ and mass flow rate of Therminol $\dot{m}_{oil}$ are measured. The cooling oil is conveyed to the test section through three sub-pipes, as shown in Figure 3.7.

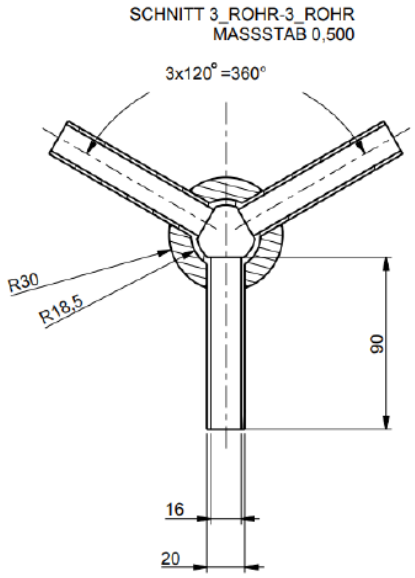

FIGURE 3.7 – TECHNICAL DRAWING OF THE THREE-PIPES OIL CONVEYOR

Downstream the test section, the outlet temperature of the secondary fluid (RTD13) $T_{oil,out}$ is measured after the regroup of the outlet sub pipes. A return pipe links the outlet of the test section with the cooling unit that closes the loop.

3.4 Construction of the test tube

In addition to the experimental analysis, this work includes the construction and equipping of the test tube. This part of the job consists in preparing the test tube before its installation inside the experimental apparatus. The test tube must be equipped with the TCs and with one

mechanical sleeve per each tube end, subsequently, the annular tube can be installed around the test tube.

3.4.1 Thermocouples installation

To favor an easier installation, the test tube is provided with grooves on the outer surface, properly designed to host the thermocouples.
A total number of 24 thermocouples have been installed in the grooves around four different cross sections along the tube; each cross section is equipped with 6 TCs.
The TCs' disposition around the tube has been chosen to fulfill three goals:

- Maximize the temperature knowledge on the test tube with the given number of sensors.
- Minimize the crossing of thermocouples' wires to reduce the risk of breakage during the installation and to limit derived turbulence effects in oil flow.
- Limit the risk of missing information in the individual section and in areas of special interest such as the upper and lower portions of the tube, considering the probable malfunction or breakage of some TCs.

A representation of the positioning of the TCs in Figure 3.8.

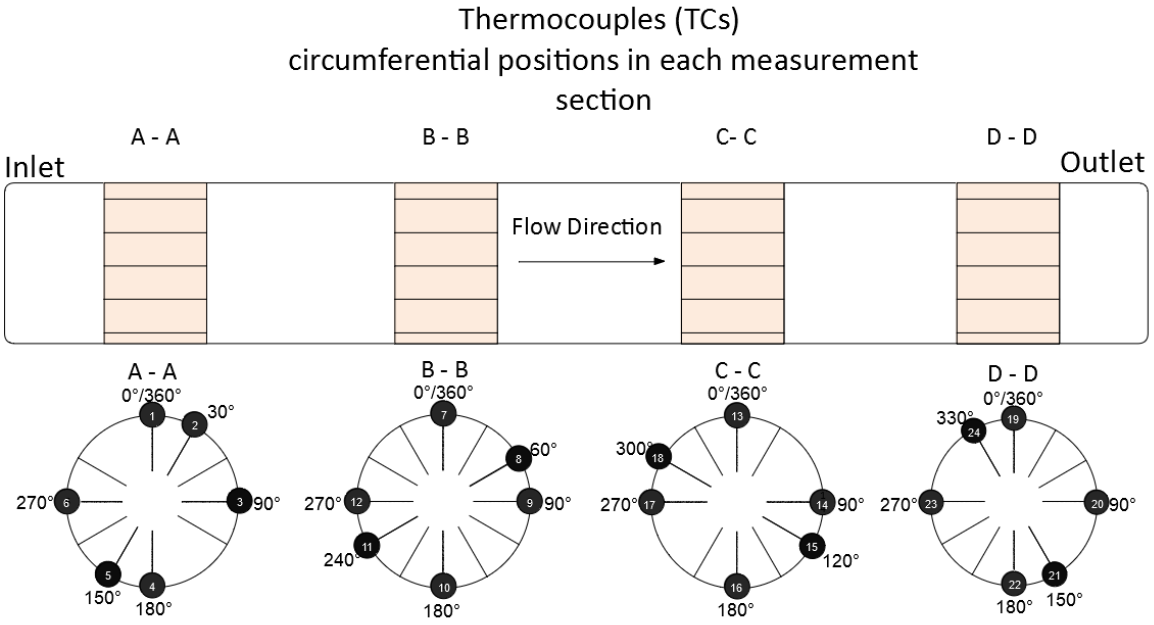

FIGURE 3.8 - THERMOCOUPLES (TCS) CIRCUMFERENTIAL POSITIONS IN EACH MEASUREMENT SECTION

In order to reach the inner sections of the tube, sections BB and CC, 'long thermocouples' were used, while shorter thermocouples were used for the outer sections, AA and DD, closer to the ends of the tube. The only relevant difference between these two types is the length of the metal wire that, if longer, allows to place the TC's sensor at a greater distance from the TC's head.

Prior to gluing, the tube was thoroughly washed with isopropanol ($(CH_3)_2CHOH$) to remove dirt and impurities from the inner and outer surfaces. The gluing process is critical for the good outcome of the experimental work; indeed, a wrong positioning of the thermocouples can undermine the quality of the measurements, compromising the whole work.

The gluing of the TCs tips has been carried out with the use of a special glue called "8349TFM – Thermal Adhesive", manufactured by "MG Chemicals" (See Figure 3.9). This thermal adhesive is a 2-part 1-1 epoxy system. It has a working time of 20 minutes and a cure time of 16 hours at room temperature or 20 minutes at 65 °C. In the present application, no heat sources have been used for the glue hardening, therefore, the cure time has been considered equal to 16 hours. Once hardened, the glue can work in a temperature range of -65 to 120 °C, which is sufficiently wide for the intended experimental work.

FIGURE 3.9 – THERMAL ADHESIVE 8349TFM

The chosen glue has a very low thermal conductivity, $\lambda_{glue} = 0.9\ \frac{W}{m*K}$. This thermal property is useful to isolate the thermocouples from the cooling oil.

The thermocouples have been glued keeping in mind that the sensor is positioned on the tip, in a space of a few millimeters. The limited working time of the glue and the willingness to install every thermocouple with the maximum care, has limited the daily gluing capacity to 5 thermocouples per day. Moreover, for precautionary reasons, it has been decided to alternate the thermocouples' installation among different sections of the tube in the same day. In fact, losing the temperature information on a full measurement section for a bad gluing technique, would have highly affected the quality of the obtained results.
A picture of two glued thermocouples is shown in Fig. 3.10.

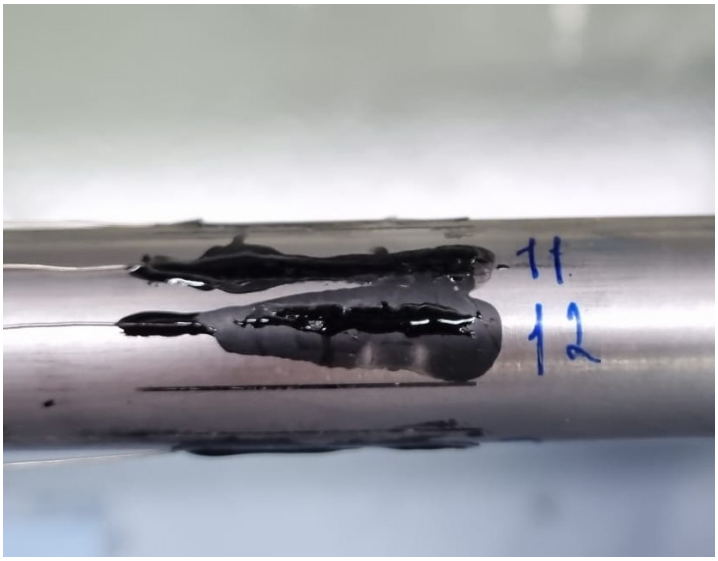

FIGURE 3.10 – DETAIL OF THERMOCOUPLES 11 AND 12 GLUED ON THE TEST TUBE.

Once all thermocouples' tips have been attached to the tube, the installation was finished by gluing the TCs' ends. This has been done properly pulling the TC wires to keep the wires themselves as close as possible to the test tube in order to limit the disturbance on oil flow. In some cases, this was not done properly; therefore, the loosest thermocouples have been glued to the tube to reestablish the required tension, as shown in Fig. 3.11.

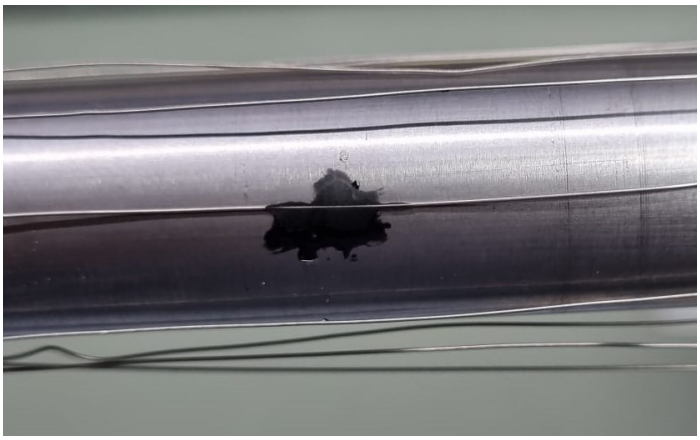

FIGURE 3.11 – DOT OF GLUE APPLIED ON A LOOSE TC.

At the very end of the tube, the TCs have been fixed to the tube by using a mechanical sleeve, properly glued applying a solvent-free two-component adhesive based epoxy resin, “UHU Plus Endfest 300”. Subsequently, the bulbs have been fixed all together on the test tube, as shown in Fig. 3.12.

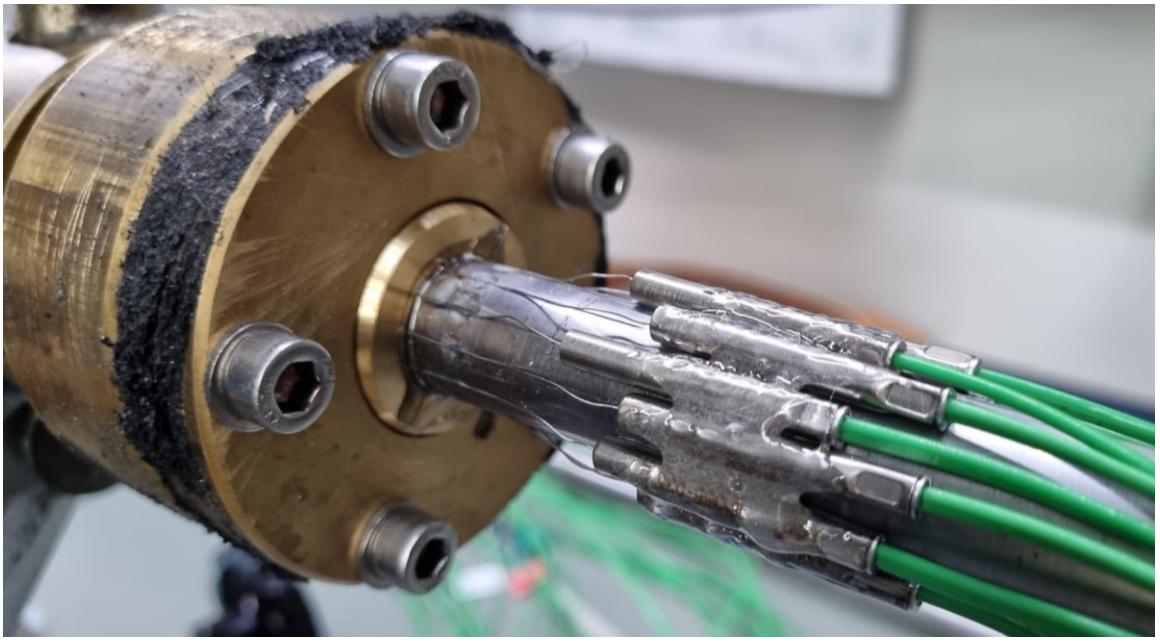

FIGURE 3.12 - TCS' BULBS GLUED ON THE EXTERNAL SURFACE OF THE TEST TUBE.

Before the installation of the external tube, the outer surface of the tube was cleaned with isopropanol to remove glue in excess and any other trace of dirt.

3.4.2 Installation of the annular tube

At this point, the annular tube can be installed around the test tube. The inner and the outer tube are fixed together by two hydraulically sealed

flanges. Prior the installation, it must be ensured that the inner tube is perfectly concentric with respect to the outer tube. This is important because imperfect concentricity could lead to the creation of an uneven oil velocity field and the resulting unevenness of convection heat transfer. To accurately adjust the concentricity of the two tubes, 6 screws were used to act on threaded holes located on two equidistant sections of the outer tube. The thickness of the annulus is measured in the different directions by using a caliber. Once the tube is ready, the screws are fixed and sealed on the threaded holes thanks to a special glue, as shown in Fig. 3.13.

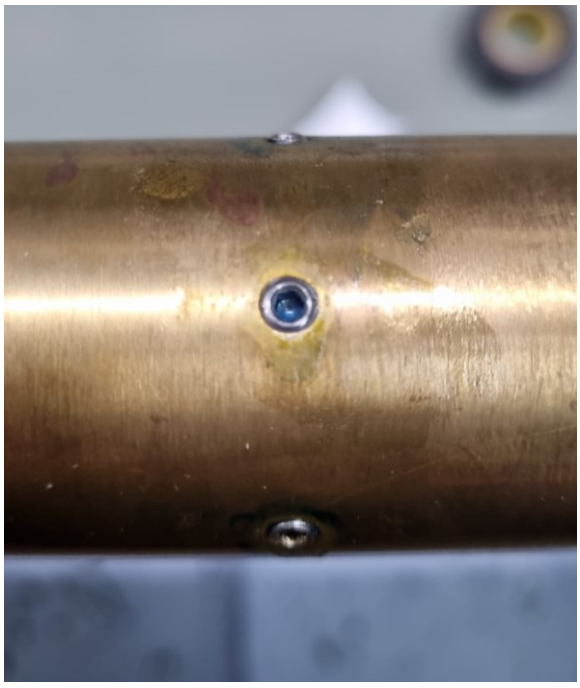

FIGURE 3.13 – DETAIL OF SEALED SCREW USED FOR CONCENTRICITY ADJUSTMENT.

Finally, the tube is installed inside the experimental apparatus.
In Fig. 3.14 a tridimensional representation of the test tube coupled with the external one is shown.

FIGURE 3.14 – 3D REPRESENTATION OF THE TEST TUBE

3.5 Sensors

Three different kinds of sensors are used in the test rig to measure three main variables:

- Temperature sensors
- Pressure sensors
- Mass flow sensors

The output signals from the sensors are collected by a centralized multiplexer. This device is linked to a computer that makes use of LabView software, where all the measured values can be visualized and monitored.

3.5.1 Temperature Sensors

As mentioned in the previous paragraphs, two types of temperature sensors are used in the test bench: the thermocouples (TCs) and the resistance temperature detectors (RTDs). In our application, both are manufactured by “E+S Metronic”.

- A thermocouple is an electrical device, consisting of two junctions made of two different conducting materials. Due to the Seebeck

effect, it's possible to associate a value of temperature to a measured of voltage. The thermocouples TC are active transducers, so they don't need power supply. The thermocouples adopted are type K thermocouples, composed of two-conductor alloys, Chromel and Alumel, covered with two protective layers. The outer one is Inconel, while the inner one is magnesium oxide (MgO). This kind of thermocouple is particularly robust thanks to the materials used. In addition, they have a quick response to temperature variations, and they are durable. In this application, the hot joint is glued into the grooves on the external surface of the inner tube, while the cold joint, used as a reference, is placed in a metal plate. The operating range is from -250 to 1200 °C.

- A resistance temperature detector (RTD) is a temperature sensor; its working principle relies on the existing relationship between the electrical resistance of a conductor and its temperature. RTDs operate in a narrower temperature range in comparison to thermocouples (from -200 to 800 °C) but, as an advantage, they have a more linear behavior that allows an easier calibration. RTD sensors used in the experimental set up are PT100. This acronym means that they make use of a platinum electrical resistance that measures 100 Ω at a temperature of 0 °C. This type of sensor is suitable for working in harsh environments.

3.5.2 Pressure Sensors

Both absolute and differential pressure transducers are used to measure pressure in different sections of the test system. Pressure measurements are particularly important to monitor the correct operation of the multiphase pump to prevent its damage. The sensors of pressure are also exploited to calculate the properties of the primary and secondary fluids in the test section and to analyze the pressure drop along the pipe. Inside the apparatus, strain gauge pressure sensors are installed. Their construction consists of a diaphragm in contact with the fluid, which is deformed by the pressure. The deformation is measured, and the corresponding pressure value is obtained.

3.5.3 Flow Sensors

In the test facility, two types of flow meters are used: Coriolis flow sensors and rotameters.

- Coriolis sensors are inertial flow meters based on the principles of motion mechanics. When the process fluid enters the sensor, the flow is split into two parallel tubes each of them with half of the total flow rate. The tubes are fixed by anchorages at the inlet and the outlet of the sensor. During operation, an electro-mechanic drive unit, positioned midway between the two anchorages, induces a vibration in both tubes and this movement causes the fluid particles to move orthogonally to the direction of the main flow. This effect produces a Coriolis force, that causes a deflection of the tubes. The two parallel vibrating tubes, generate two different sinewaves, measured by a special sensor. These waves have the same frequency but are out of phase. The time delay between the two sinewaves is directly proportional to the mass flow rate $\dot{m}$, which can thus be determined. Such sensors are used to measure the mass flow rate $\dot{m}$ of gases and liquids upstream of the test section.

- Rotary sensors are variable area gauges and are used in the test bench to measure bypass flow. A shaped weight positioned inside the sensor is pushed upward by the flow drag force and pulled downward by gravity. The equilibrium position defines the volumetric flow rate $\dot{V}$ in the tube. The output value is exhibited by an analog indicator external to the sensor.

3.5.4 Sensors Data Sheets

TABLE 3.2 – SENSORS' DATA TECHNICAL FEATURES

Variable	Sensor	Range		Unit	Accuracy
		Min	Max		
Temperature	*TC*	-250	1200	[°C]	± 0,2 °C
Temperature	*RTD*	-200	850	[°C]	± 0,15 °C
Pressure	*AP1*	0	30	[bar]	± 0,2 %
Pressure	*AP2*	0	100	[bar]	± 0,2 %
Pressure	*AP5, AP6*	5	85	[bar]	± 0,106 %
Pressure	*DP01*	0	1000	[mbar]	± 0,040 %
Mass flow rate	*Promass 83°04*	0	90	[kg/h]	± 0,1 % of 22,5 kg/h
Mass flow rate	*Promass 83°05*	0	3600	[kg/h]	± 0,1 % of 540 kg/h
Mass flow rate	*Mass2100-6*	0	563.2	[kg/h]	± 0,05 % of 30 kg/h
Mass flow rate	*Mass2100-15*	0	2914	[kg/h]	± 0,05 % of 80 kg/h
Mass flow rate	*Mass flux Coolin B*	0	10000	[kg/h]	± 0,1 % of 105 kg/h
Mass flow rate	*Rotameter*	0	5.5	[m^3/h]	± 1,6 % of 3,065 m^3/h

3.6 Fluids of the experimental apparatus

The fluids that flow inside the experimental apparatus can be grouped in two main categories: primary and secondary fluids. The one and only primary fluid is propylene, which flows in the whole primary circuit. The secondary fluids are water and Therminol D12. Their purpose is to cool the test section and allow the primary fluid to return to the test section inlet at the desired conditions of temperature T, pressure p, and vapor quality x.

In the following, the three mentioned fluids are briefly presented and described:

- Propylene (C_3H_6) is an unsaturated organic compound. Its chemical formula is $CH_3CH=CH_2$. It belongs to the alkene class of hydrocarbons. In refrigerant's nomenclature, it is identified with the acronym R1270. Some characteristics of interest are briefly presented:
  - Low Global Warming Potential (GWP = 2)
  - Null Ozone Depletion Potential (ODP = 0)
  - High flammability. According to the ASHRAE safety groups, its designation is A3, "A" corresponds to low toxicity level and "3" to high flammability.
  - Low charge requested

- Water is abundant and cheap. Furthermore, it has excellent thermodynamics properties that makes it suitable as heat transfer fluid. It is directly used only in the first heat exchanger of the bypass cycle and then as coolant in the cooling machine of the SECTSO and in all Huber thermostats.

- Therminol D12 is a synthetic, liquid phase heat transfer fluid, produced by "Eastman Chemical Company". It is especially suited to applications where a low order of acute toxicity and odor are desired. Therminol D12 is based on halogen-free chemistry and is considered non-hazardous and practically harmless to the environment. Due to its excellent heat transfer properties, it is used in all secondary cycles and in the test section to exchange heat with propylene. Therminol D12 has an operative temperature range of -94° to 190°C.

3.7 Safety measures

Propylene is a highly flammable substance, so protective measures against explosions and the spread of fire must be considered. The entire test rig is surrounded and sealed by an enclosure consisting of a metal structure with plastic walls. A gas sensor measures the percentage of hydrocarbons in the air, triggering an alarm if dangerous levels of hydrocarbons are detected. When a certain limit is exceeded, a

ventilation system is activated, and the working fluid is drained outside the enclosure and adsorbed by an activated carbon filter.

4 Data reduction

After having conducted the experimental work, the acquired data must be properly elaborated to calculate all the variables of interest. The goal of this chapter is to present the assumptions and to explain the methods adopted to calculate the local α_{loc} and overall heat transfer coefficients α. Before the calculations, the temperature measured by the thermocouples need to be properly modified according to the calibration procedure. Pressure losses are measured directly through the sensors, therefore, there's no need to carry out any calculations or corrections to the recorded values.

4.1 Calibration of the thermocouples

In order to get information about the temperature on the external surface of the inner tube, Type K thermocouples are used.

As already mentioned in Paragraph 3.5.1, a thermocouple is an electrical device, consisting of two conductive materials that form an electrical junction, as shown in Fig. 4.1. The thermocouples adopted for this work are type K, composed by two-conductor alloys, Chromel and Alumel.

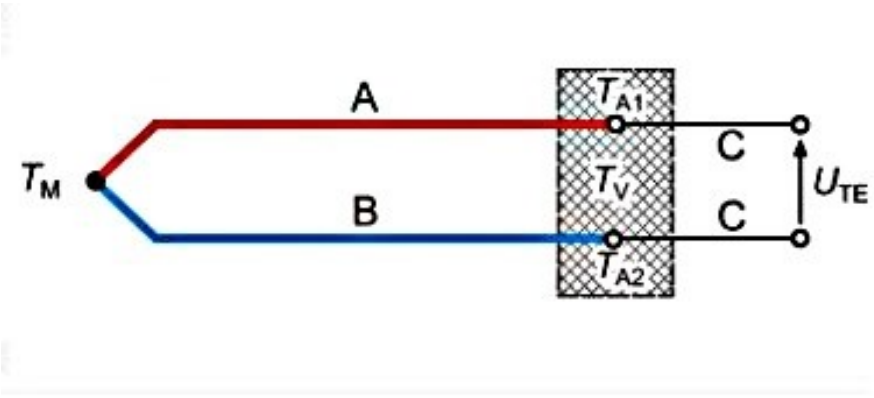

FIGURE 4.1 – SCHEMATIC REPRESENTATION OF A THERMOCOUPLE

Thanks to the Seebeck effect, it is possible to associate a temperature value with a voltage measurement. In Fig. 4.2, the characteristic curve of a Type K thermocouple is reported; the voltage ΔU, on the y-axis is

plotted as function of the temperature T. It's noticeable that the trend is almost perfectly linear.

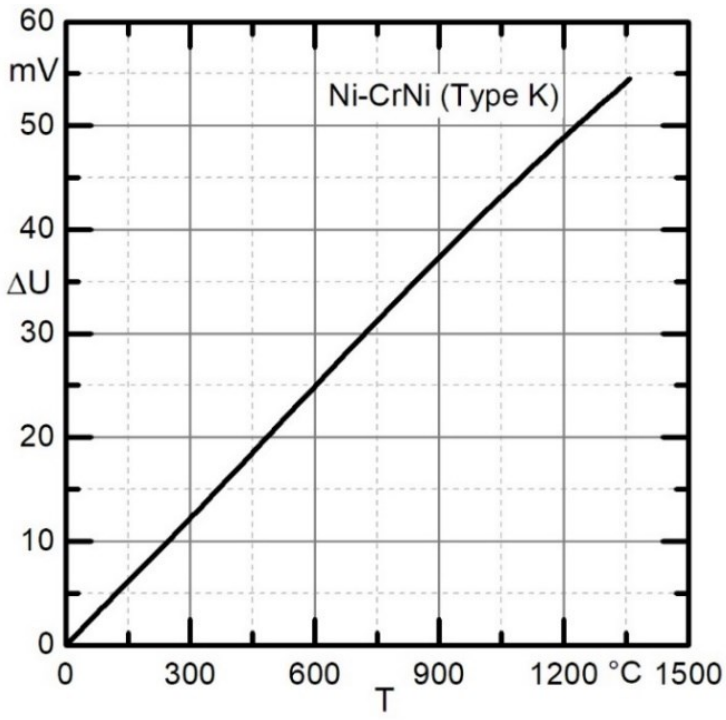

FIGURE 4.2 – CHARACTERISTIC CURVE OF A TYPE K THERMOCOUPLE

Before the installation on the test tube, the thermocouples must be calibrated in order to minimize their measurement uncertainty. The reason for performing calibration is to reduce all temperature effects not associated with condensation. Calibration consists in comparing the TCs acquired output to the measurement of a more accurate equipment. In Fig. 4.3, the mean temperatures measured by the 24 TCs during calibration are plotted and compared to the reference temperature T_{ref} (green line). It can be noted that the offset can be considerable, even greater than 1 °C for some thermocouples.

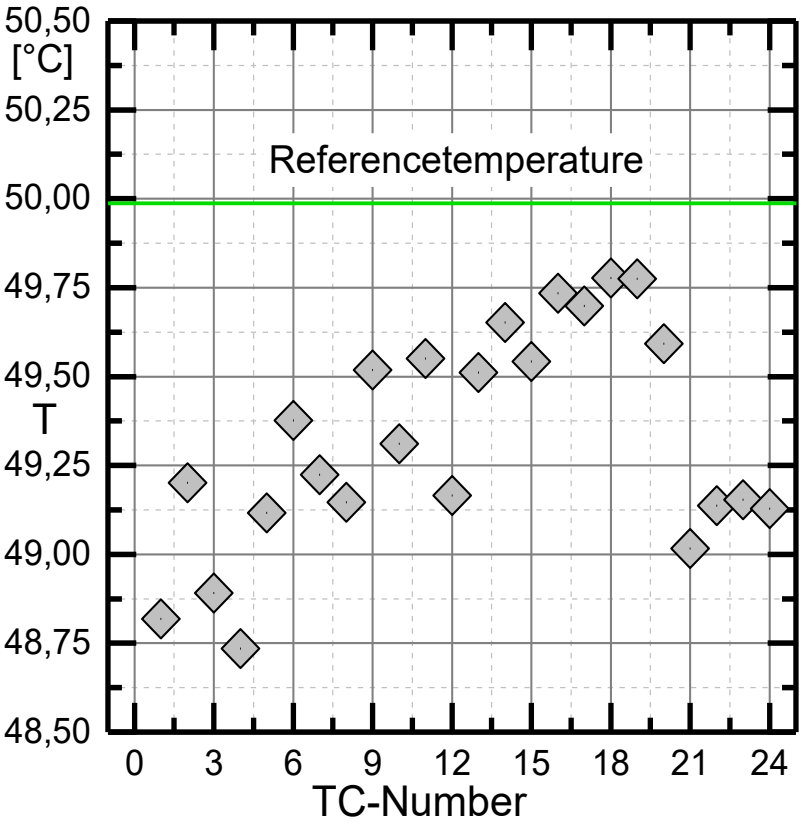

FIGURE 4.3 – EXEMPLARY TEMPERATURE MEASUREMENTS DURING THE CALIBRATION PROCESS

The calibration procedure has been carried out inside the thermodynamics laboratory, making use of a “Julabo SL” machine, shown in Fig. 4.4. This machine allows calibration measurements in a range of temperature between -50 and 105 °C.

FIGURE 4.4 – CALIBRATION MACHINE "JULABO SL"

Before starting the calibration, an ice-water heterogeneous mixture has been taken as reference point, being at almost constant 0°C. The TCs to be calibrated were placed inside a chamber, taking care that the sensors were immersed a liquid medium, maintained at the reference temperature T_{ref}, as shown in Fig. 4.5.

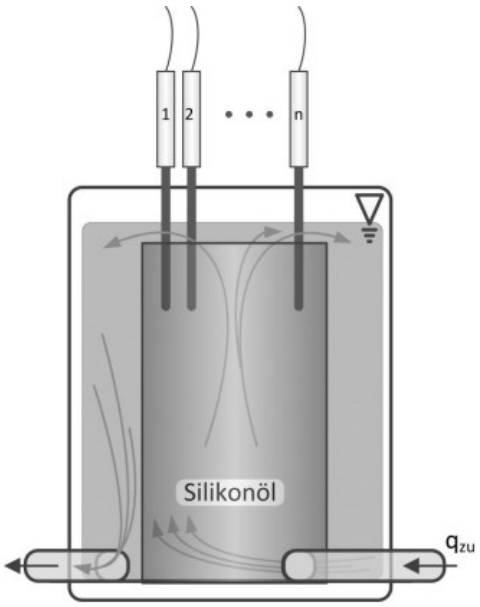

FIGURE 4.5 – SCHEMATIC DRAWING OF THE CALIBRATION BATH

The medium used as reference is a silicone-based temperature control liquid called "JULABO Thermal H5". The calibration machine allows to change the reference temperature T_{ref} of the medium to perform the calibration in a wide range of temperature values.

The temperature of the reference medium has been varied according to the following pattern:

- First heating cycle from 0 to 80 °C with a step of 10 °C.
- First cooling cycle from 80 to 0 °C with a step of 10 °C.
- Second heating cycle from 0 to 80 °C with a step of 10 °C.
- Second cooling cycle from 80 to 0 °C with a step of 10 °C.

To ensure that a steady-state condition exists for the measurement, a period of 60 minutes is set between each temperature change. During the data recording, the analogue voltage signal of the thermocouples is

transmitted to a data logger via a measuring card. The data from the thermocouples and the precision thermometer are transferred to a PC via an interface. These data are stored in LabVIEW as a data matrix.

In total, 33 reference temperatures have been tested.

Following the data collection work, a calibration method has been implemented. By comparing the recorded temperatures from the thermocouples with the reference temperature T_{ref}, it is possible to define a calibration function. The calibration function is an equation that allows to calculate the calibrated temperatures, T_{cal}, from the raw temperature measurements, T_{raw}. A second-degree polynomial interpolation function has been adopted to accomplish this task. In a temperature range from above -270 °C to 1300 °C, the calibration function for thermocouples type K is calculated, according to Tegeler [29], with the following equation:

$$T_{cal} = R_0^* \cdot (1 + A_0^* \cdot T_{raw} + B_0^* \cdot T_{raw}^2) \tag{4.1}$$

The coefficients R_0^*, A_0^* and B_0^* for the polynomial function have been calculated solving the system of equation resulting from the following matrix-form equation:

$$\begin{pmatrix} m & \sum T_j^1 & \sum T_j^2 \\ \sum T_j^1 & \sum T_j^2 & \sum T_j^3 \\ \sum T_j^2 & \sum T_j^3 & \sum T_j^4 \end{pmatrix} \cdot \begin{pmatrix} R_0^* \cdot 1 \\ R_0^* \cdot A^* \\ R_0^* \cdot B^* \end{pmatrix} = \begin{pmatrix} \sum R_i \cdot T_j^0 \\ \sum R_i \cdot T_j^1 \\ \sum R_i \cdot T_j^2 \end{pmatrix} \tag{4.2}$$

The solution has been found adopting a numerical, least mean square value method:

$$\sum_{i=0}^{n} \Delta R_{0i}(T_j) = \sum_{i=0}^{n} \left[R_{0i}^*(T_j) - R_{0i}(T_j)\right]^2 \rightarrow Min. \tag{4.3}$$

4.2 Assumptions

In the following, the main assumptions for the calculation of the heat transfer coefficient α are listed:

- The whole system is considered stationary.
- Ambient heat losses are neglectable, i.e., the total heat exchanger can be considered adiabatic.
  This assumption can be adopted because all the system components are insulated to the outside with a thick insulating material.
- Pressure losses on the oil-side are neglected.
- At a given section, i.e., position along the test tube length L, oil and propylene temperatures are assumed to be constant. Both oil and propylene temperature change along the z-coordinate but are assumed to be constant along the radial direction ϕ.

4.3 Temperature profiles

The temperature profiles are graphs that represent the trend of temperature of oil, propylene, and external surface of the inner tube as function of the tube length z.
Propylene temperature is measured only at the inlet and at the outlet of the test tube by two RTD sensors.
Thermocouples allow to measure the temperature at different angles ϕ of the circumference for 4 different tube sections. The temperature values are properly corrected according to the calibration explained in Paragraph 4.1.
Oil temperature T_{oil} is measured at inlet and outlet sections and on 20 measuring points along the annular tube by RTD sensors.
A representation of the temperature profiles is reported in Figure 4.6.

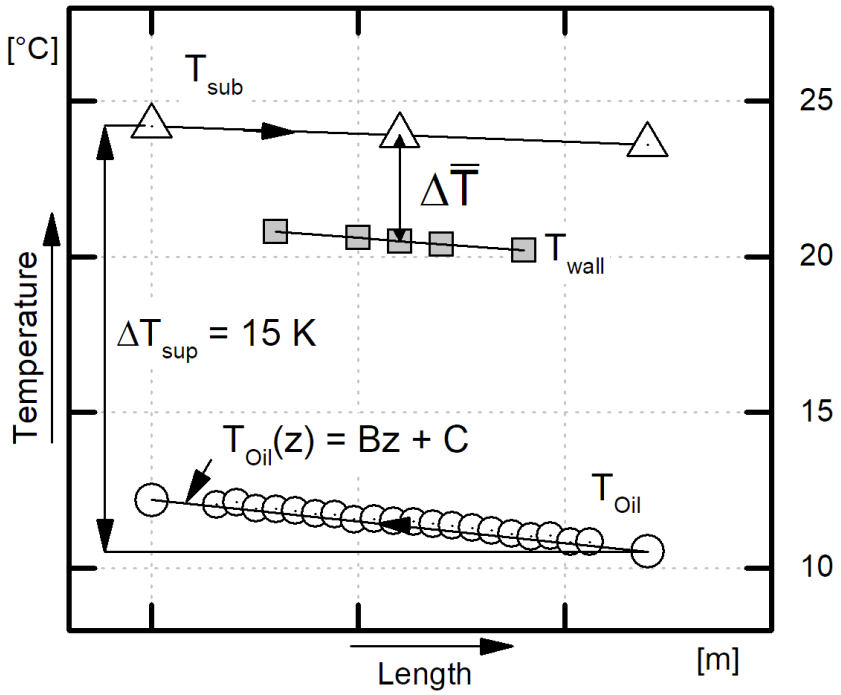

FIGURE 4.6 – EXPLICATIVE REPRESENTATION OF THE TEMPERATURE PROFILES

Propylene temperature profile

The propylene temperature profile is determined thanks to the values of pressure p available at the inlet and at the outlet of the test tube. In fact, being the substance in saturated conditions, it's possible to associate a unique temperature T to the pressure recorded. Nevertheless, RTDs are present at both inlet and outlet for a double check on temperatures determined from the pressure sensors. The temperature profile is simply given by the interpolation of these two values and assumed to be linear.

The condensation process ideally occurs at constant temperature but, since the pressure is decreasing along the tube, due to pressure drops, the temperature of propylene varies accordingly.

Oil temperature profile

The oil temperature profile is defined by a linear interpolation of the 20 measurement points recorded by the RTD sensors.

These points are interpolated by a linear spline,

$$T_{oil}(z) = Bz + C. \tag{4.4}$$

This equation links oil temperature with the z-coordinate of the tube.

Wall temperature profile

The temperature of the outer surface of the inner tube is measured thanks to the 24 thermocouples glued around 4 different sections of the tube.

The 6 values of temperature acquired per each section are averaged to obtain one mean value of temperature T_{wall}. The 4 mean values are linearly interpolated to get the wall temperature profile. Similarly to the oil, the interpolation function

$$T_{wall}(z) = Dz + E \tag{4.5}$$

allows to associate a temperature to a given z-coordinate of the tube.

The temperature difference between the inlet propylene temperature and the inlet oil temperature is defined as ΔT_{sub}. This temperature difference is set equal to 15 K and kept constant during the whole experimental activity.

4.4 Calculation of the overall heat transfer coefficient

In this paragraph, after having defined some key variables, the methods, and the calculations to evaluate the overall heat transfer coefficient α are explained.

The mass flux density

$$G = \frac{\dot{m}_V + \dot{m}_L}{A} \tag{4.6}$$

is a function of the mass flow rates of vapor and liquid phase as well as the cross-sectional area A of the inner test tube. The mass flow rate of each phase is measured by a mass flow meter in the vapour and liquid line. The reduced pressure

$$p^* = \frac{p_{prop}}{p_{crit}} \tag{4.7}$$

is calculated as the ratio between the measured inlet absolute pressure and the critical pressure of the test substance. The inlet vapor quality

$$x_{in} = \frac{h_{mix} - h_{sat,liq}}{h_{sat,vap} - h_{sat,liq}} \tag{4.8}$$

is function of the specific enthalpy of the two phases in saturated conditions, and, assuming to have adiabatic mixture at the static mixer, of the mixture specific enthalpy

$$h_{mix} = \frac{\dot{m}_V \cdot h_V + \dot{m}_L \cdot h_L}{\dot{m}_V + \dot{m}_L}. \tag{4.9}$$

The specific enthalpy of each phase

$$\begin{aligned} h_V &= f(\rho_V, T_{sat}) \\ h_L &= f(\rho_L, T_{sat}) \end{aligned} \tag{4.10}$$

is a function of the density ρ and temperature T of the vapor and liquid phase. For the calculation of the specific enthalpies of both liquid h_L and vapor phase h_V, the software REFPROP is used.

As mentioned in Paragraph 4.1, specific assumptions are applied to calculate the heat transfer coefficient during condensation.

By definition, the heat flow rate released by propylene,

$$\dot{Q}_{prop} = \dot{m}_{prop} \cdot h_{LV} \cdot (x_{j+1,prop} - x_{j,prop}), \tag{4.11}$$

where r is the enthalpy of condensation of propylene per unit mass at the given pressure p_{sat}, is so calculated. On the oil side, the heat flow rate absorbed,

$$\dot{Q}_{oil} = \dot{m}_{oil} \cdot c_{p,oil} \cdot \left(T_{j+1,oil} - T_{j,oil}\right), \tag{4.12}$$

is formulated as shown.

Due to the neglection of the ambient heat losses, the one-dimensional heat flow rate in radial direction,

$$\dot{Q}_{prop} = \dot{Q}_{oil} = \dot{Q} \tag{4.13}$$

is defined by the energy balance between the heat released by the test substance and the heat absorbed by the cooling oil. Having set the temperature difference between the inlet oil and inlet substance temperature, $\Delta T_{sup} = 15\,K$, and according to the energy balance between propylene and Therminol, it can be calculated that, only partial condensation occurs. The change in vapor quality is in the order of 10%.

The temperature of the oil

$$T_{oil}(z) = Bz + C \tag{4.14}$$

is then defined as function of the tube length L, z-coordinate. As explained in the previous paragraph, coefficients B and C are calculated with a linear spline based on the measured oil temperatures in the annular tube (see Fig. 4.6).
If we differentiate the oil temperature on the z-coordinate,

$$\frac{dT_{oil}}{dz} = B = const. \tag{4.15}$$

we obtain a constant, equal to B.
The heat flow rate differentiated along the tube length,

$$\dot{Q}_{dz} = \frac{d\dot{Q}}{dz} = \dot{m}_{oil} \cdot c_{p,oil} \cdot \frac{dT_{oil}}{dz} \tag{4.16}$$

is calculated as function of the oil mass flow rate $\dot{m}_{oil}$, the specific heat $c_{p,oil}$ and the temperature differentiated on the z-coordinate $\frac{dT_{oil}}{dz}$. Being $\frac{dT_{oil}}{dz}$ and the oil mass flow rate $\dot{m}_{oil}$ constant, and assuming with good approximation that the specific heat of oil $c_{p,oil}$ is constant, it's possible to conclude that $\frac{d\dot{Q}}{dz}$ is also constant along the tube.
At each *j-th* measuring section, the temperature difference between propylene and the outer wall temperature is so defined:

$$\Delta T_j = T_{prop,j} - T_{wall,j}. \tag{4.17}$$

The heat transferred from the substance to the oil is so calculated,

$$\dot{Q} = K \cdot A \cdot \Delta T_{ml} \tag{4.18}$$

as function of the overall heat transfer coefficient K, the heat transfer area A, and the logarithmic mean temperature difference ΔT_{ml}.
The logarithmic mean temperature difference is defined as follows:

$$\Delta T_{ml} = \frac{\left(T_{prop,in} - T_{oil,out}\right) - \left(T_{prop,out} - T_{oil,in}\right)}{ln\left(\frac{T_{prop,in} - T_{oil,out}}{T_{prop,out} - T_{oil,in}}\right)}. \tag{4.19}$$

The heat is transferred from the substance to the oil and the total thermal resistance is

$$R_{tot} = \frac{1}{K \cdot A} = \frac{1}{\alpha_i \cdot A_i} + R_{con} + \frac{1}{\alpha_e \cdot A_e}. \tag{4.20}$$

This total thermal resistance R_{tot} is the sum of all the thermal resistances encountered by the heat flow.
The conductive thermal resistance

$$R_{con} = \sum_n \frac{1}{\lambda_n} \cdot ln\left(\frac{D_{n+1}}{D_n}\right) \tag{4.21}$$

accounts for all cylindrical thermal resistances of the layers around the tube, considering their own conductivity λ_n and thickness $(D_{n+1} - D_n)$.
Since the value of the heat transfer coefficient on the oil side α_{oil} is not known and would provide too many unknown variables in the equation, we consider the heat transfer from the substance to the outer surface of the inner tube. In fact, the external surface temperature of the inner tube is known thanks to the TCs. Knowing that the rate of heat flow $\dot{Q}$ exchanged between the working fluid and the external pipe surface is the same of the one exchanged between the substance and the oil, it is possible to write, for the *j-th* tube section:

$$\dot{Q}_j\left(= \dot{Q}_{prop,j} = \dot{Q}_{oil,j}\right) = K \cdot A \cdot \Delta T_{m,j} \tag{4.22}$$

The mean temperature difference is calculated between the propylene temperature and the mean value of the wall temperature at the *j-th* section,

$$\Delta T_{m,j} = T_{prop,j} - T_{wall,m,j}. \tag{4.23}$$

The heat transfer must be calculated in any point of the tube length L. The equation (4.26) can be written as:

$$\frac{\Delta \dot{Q}_j}{\Delta z} = \dot{Q}_{\Delta z} = K_{mod} \cdot A \cdot \frac{\Delta T_{m,j}}{\Delta z} \tag{4.24}$$

The total modified thermal resistance related to this temperature difference is

$$\frac{1}{K_{mod} \cdot A} = \frac{1}{\alpha_i \cdot A_i} + R_{con}. \tag{4.25}$$

This is again the sum of the thermal resistances encountered.
By substituting equation (4.25) in the (4.24), we get:

$$\dot{Q}_{\Delta z} = \frac{1}{\frac{1}{\alpha_i \cdot A_i} + R_{con}} \cdot \Delta T_{m,j}. \tag{4.26}$$

From this equation, the overall heat transfer coefficient can be calculated,

$$\alpha_{j,m} = \frac{2}{d_i \cdot \left(\frac{2 \cdot \pi \cdot \Delta T_{m,j}}{\dot{Q_{\Delta z}}} - R_{con}\right)}. \quad (4.27)$$

$\alpha_{j,m}$ is the mean value of the heat transfer coefficient in a single section around the test tube and it is a function of the heat flux $\dot{Q_{\Delta z}}$ and the temperature difference $\Delta T_{m,j}$.
The overall heat transfer coefficient α is simply calculated by averaging the four values obtained in the 4 Measurement sections.

4.5 Calculation of the local heat transfer coefficients

In this paragraph, the calculations to determine the local heat transfer coefficients α_{loc} are described. The adjective local, is referred to the radial direction ($\phi - coordinate$) and not to the longitudinal direction ($z - coordinate$).
Thanks to the TCs placed on different tube angles ϕ, we have information about the local temperature difference between propylene and the wall,

$$\Delta T_{j,\phi} = \Delta T_{loc} = T_{prop,j} - T_{wall,j,\phi} \quad (4.28)$$

where $T_{prop,j}$ is the temperature of propane at a given position along the tube z-coordinate, and it is assumed to be constant on the radial direction ϕ.
The variable $T_{wall,j,\phi}$ is the local value of temperature, at a given tube section j and a given radial direction ϕ.
The local rate of heat flow is calculated as function of the local temperature difference,

$$\dot{Q}_{loc} = K \cdot A \cdot \Delta T_{loc}. \quad (4.29)$$

Knowing that,

$$\frac{1}{K \cdot A} = \frac{1}{\alpha_i \cdot A_i} + R_{con}. \quad (4.30)$$

Similarly to what have been done for the overall value of heat transfer coefficient $\alpha_{j,m}$ for a given section,

$$\alpha_{loc} = \frac{2}{d_i \cdot \left(\frac{2 \cdot \pi \cdot \Delta T_{loc}}{\dot{Q}_{loc}} - R_{con} \right)}. \tag{4.31}$$

is calculated by substituting equation (4.30) in equation (4.29).
The formulation is nearly identical to the one utilized for the overall values of heat transfer coefficients, with the difference that we make use of the local values of temperature difference $\Delta T_{j,\phi}$ and rate of heat flow $\dot{Q}_{\Delta z,loc}$.

5. Experimental work

The experimental work has been carried out at the KIIR; using the test rig described in Chapter 3. The system allows to act on both propylene and oil sides to adjust the flow condensation conditions. During experimentation, propylene in two-phase flow condenses on contact with the tube, cooled by the oil flow, with a decrease in vapor quality x. The goal of the experimental work is to evaluate the local α_{loc} and overall two-phase heat transfer coefficient α, and the pressure drops $\left(\frac{\Delta p}{\Delta L}\right)_{tp}$ along the test tube at different values of reduced pressure p^*, mass flux G and vapor quality x.
Condensation of propylene is studied in four different flow conditions. In Table number 5.1 the experimental measurements settings are reported.

TABLE 5.1 – EXPERIMENTAL MEASUREMENT PLAN SETTINGS

Measurement	$\boldsymbol{p^*}$	$\boldsymbol{p_{sat}}$ $[bar]$	$\boldsymbol{T_{sat}}$ $[°C]$	$\boldsymbol{G}$ $[kg/m^2s]$
1	0.25	11.4	24.5	600
2	0.25	11.4	24.5	300
3	0.5	22.75	54.5	600
4	0.5	22.75	54.5	300

The plan is to vary the vapor quality x at the inlet of the test tube for each measurement, from $x = 0.1$ to $x = 0.9$ with a step of 0.1.
For measurement 1, $p^* = 0.25$, and $G = 600\ \frac{kg}{m^2 s}$, due to the impossibility to run the facility at the highest value of vapor quality x, the range of variation is set from $x = 0.1$ to $x = 0.8$.
For measurement 2, $p^* = 0.25$, and $G = 300\ \frac{kg}{m^2 s}$, due to the impossibility to run the facility at the highest values of vapor quality x, the range of variation is set from $x = 0.1$ to $x = 0.7$.
For measurement 4, $p^* = 0.5$, and $G = 300\ \frac{kg}{m^2 s}$, due to the impossibility to run the facility at highest values of vapor quality x, the range of variation is set from $x = 0.1$ to $x = 0.6$.

Due to the high sensitivity of the experimental facility, vapor quality x may slightly differ from the value set in the measurement plan. Moreover, in the results graphs, the mean vapor quality x_m along the tube is associated to each measurement. Clearly, this value is always lower than the inlet vapor quality x_{in} set.
As already mentioned in Chapter 4, the temperature difference between the inlet propylene temperature and the inlet oil temperature, ΔT_{sub}, is set equal to 15 K and kept constant for all the measurements executed.
The limited tube length L, coupled with the limited cooling capacity $\dot{Q}$, doesn't allow to perform full condensation inside the test tube. The decrease of vapor quality x along the tube varies according to the experimental conditions and is in the order of 10%.
The LabView Software installed in the PC available in the laboratory, provides the representation of the circuit, from which it's possible to monitor pressure p, temperatures T, and mass flow rates $\dot{m}$ inside the apparatus, in real time. Moreover, from LabView, the degree of opening of the valves can be directly adjusted to vary the vapor quality x. In the same way, the number of revolutions per minute rpm of the two-phase pump can be modified with a consequential effect on pressure p and mass flux G.

5.1 Preliminary comments on the local results

In this paragraph, the local results obtained are critically commented and analyzed with the goal of evaluating their accuracy and reliability. Doing so, some critical aspects regarding the experimental set up and the data reduction are highlighted.
The thermocouples glued on the test tube outer surface provide us the local tube wall temperature T_{wall}, in the position where the TC is installed. The substance temperature T_{prop} at a given position on the test tube is determined by the linear interpolation of the two temperatures recorded at two opposite ends of the tube.
From these two values, the local temperature differences between propylene and the tube wall ΔT_{loc} can be determined.
Both these measurements go along with their uncertainties. Indeed, the local tube wall temperature T_{wall}, contains the TC's own uncertainty

while the substance temperature T_{prop} is determined from two temperatures measured by RTDs with their own uncertainties and, moreover, the linear temperature trend assumed is not validated by any specific theory neither by direct temperature measurements inside the test tube.

In Fig. 5.1, two graphs are reported. Both graphs display the local temperature differences ΔT_{loc} on the y-axis, and the radial direction ϕ on the x-axis, for measurement Section 3. Moreover, in each graph the measured values of 3 test conditions are plotted, at three values of vapor quality $x = 0.1; 0.3; 0.6$.

Fig. 5.1 favors the comparison of different reduced pressures $p^* = 0.25; 0.5$, at constant mass flux $G = 600 \frac{kg}{m^2 s}$.

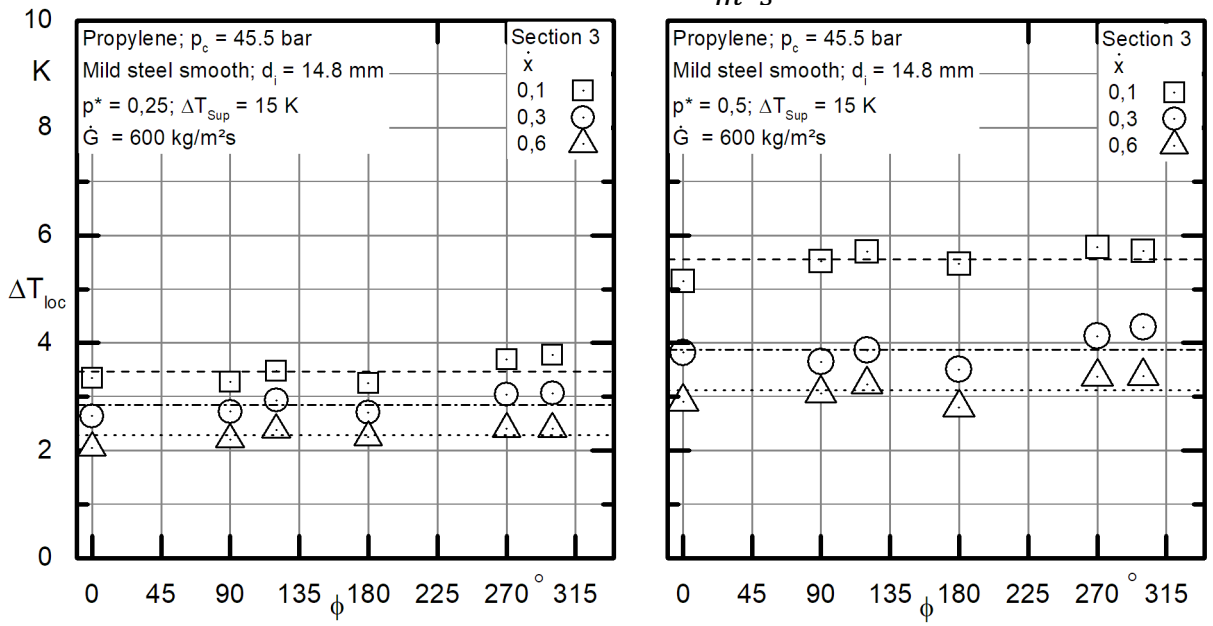

FIGURE 5.1 – LOCAL TEMPERATURE DIFFERENCES IN SECTION 3; EFFECT OF PRESSURE.

It can be observed, for both graphs, that the differences in terms of measured temperature differences ΔT_{loc} at constant vapor quality x, are relatively low. This observation is made easier by the presence of the dotted lines which represent the average temperature difference at fixed vapor quality x.

Overall, the local differences ΔT_{loc} are higher at higher pressure p.

In Fig. 5.2, two graphs are reported. As in Fig. 5.1, both graphs display the local temperature differences ΔT_{loc} on the y-axis and the radial direction ϕ on the x-axis, for measurement section 3. Moreover, in each graph the

measured values of 3 testing sessions are plotted, at three values of vapor quality $x = 0.1; 0.3; 0.6$.
Fig. 5.2 favors the comparison of different mass fluxes $G = 600; 300$, at constant reduced pressure $p^* = 0.25$.

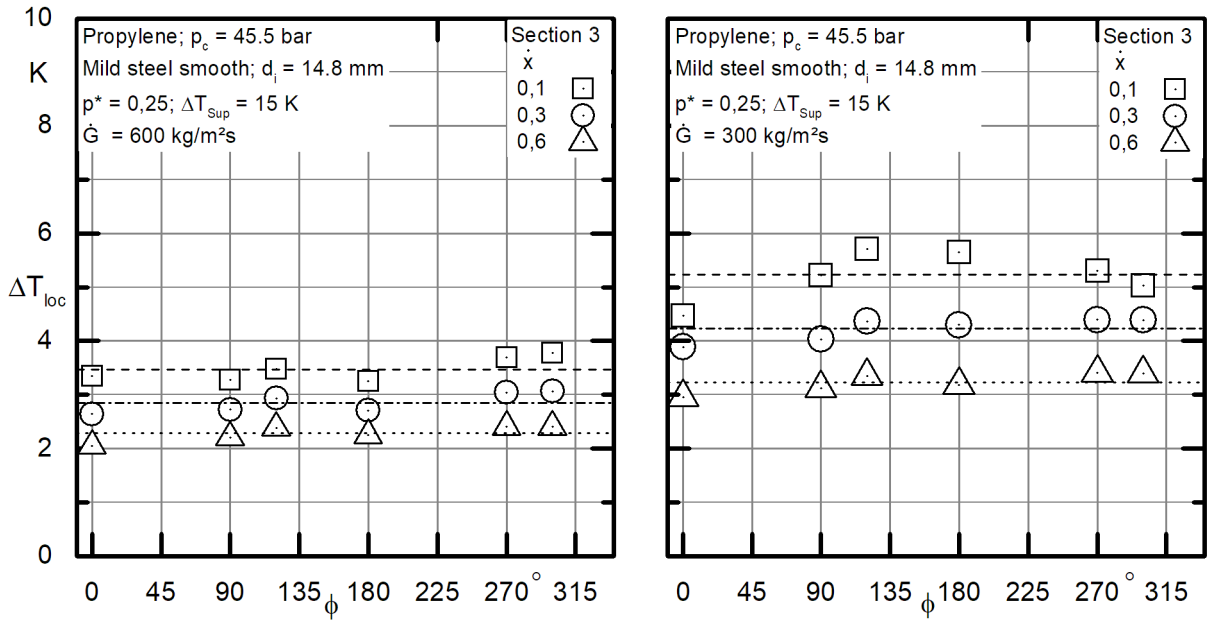

FIGURE 5.2 - LOCAL TEMPERATURE DIFFERENCES IN SECTION 3; MASS FLUX EFFECT.

Similar considerations to the ones done for Fig. 5.1 can be drawn. Relatively small differences within the same measurement section are noticed, except for the condition $p^* = 0.25;\ G = 600; x = 0.1;$
Overall, the local differences ΔT_{loc} are higher at lower mass flux G.
From the values of local temperature differences ΔT_{loc}, it is possible to determine the local heat transfer coefficients $\alpha_{i,loc}$, according to Eq. 4.31, as explained in Chapter 4,

$$\alpha_{i,loc} = \frac{2}{d_i \cdot \left(\frac{2 \cdot \pi \cdot \Delta T_{loc}}{\dot{Q}_{\Delta z,loc}} - R_{con} \right)}. \tag{4.31}$$

In Fig. 5.3, a couple of graphs is reported. Both graphs display the local heat transfer coefficients $\alpha_{i,loc}$ on the y-axis, and the radial direction ϕ on the x-axis, for measurement section 3. This figure is complementary to Fig. 5.1, local heat transfer coefficients α_{loc} are plotted for three values of vapor quality $x = 0.1; 0.3; 0.6$.

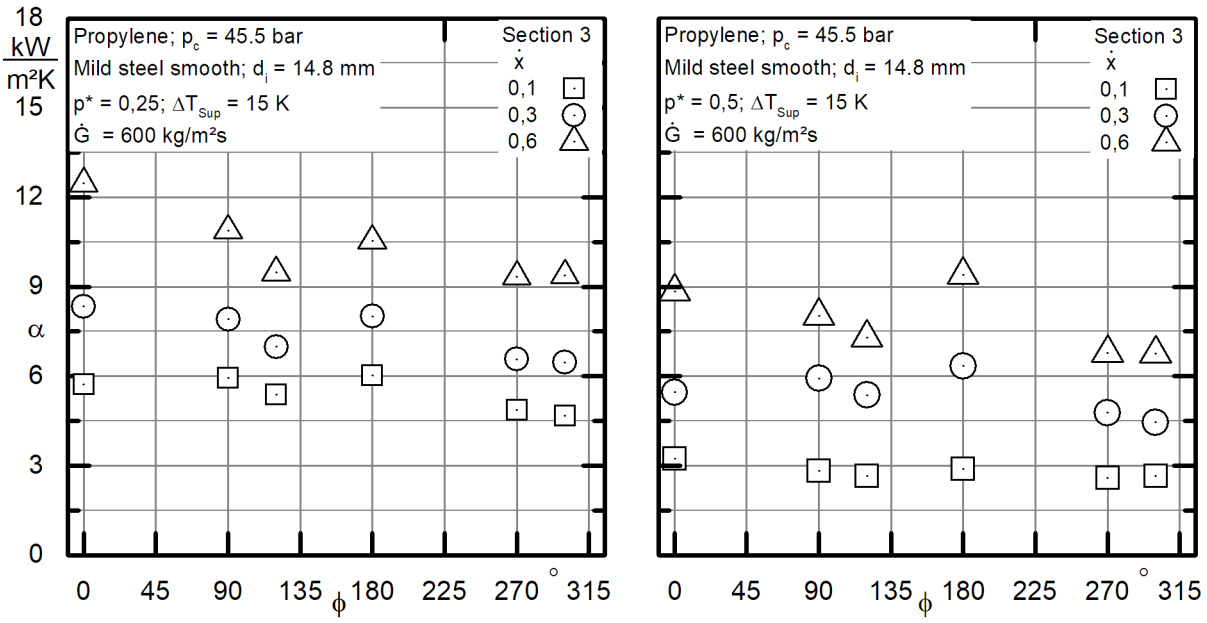

FIGURE 5.3 – LOCAL HEAT TRANSFER COEFFICIENTS IN SECTION 3; EFFECT OF PRESSURE.

In Fig. 5.4, a couple of graphs is reported. As in Fig. 5.3, both graphs display the local heat transfer coefficients α_{loc} on the y-axis, and the radial direction ϕ on the x-axis, for measurement section 3. This figure is complementary to Fig. 5.2, local heat transfer coefficients α_{loc} are plotted for three values of vapor quality $x = 0.1; 0.3; 0.6$.

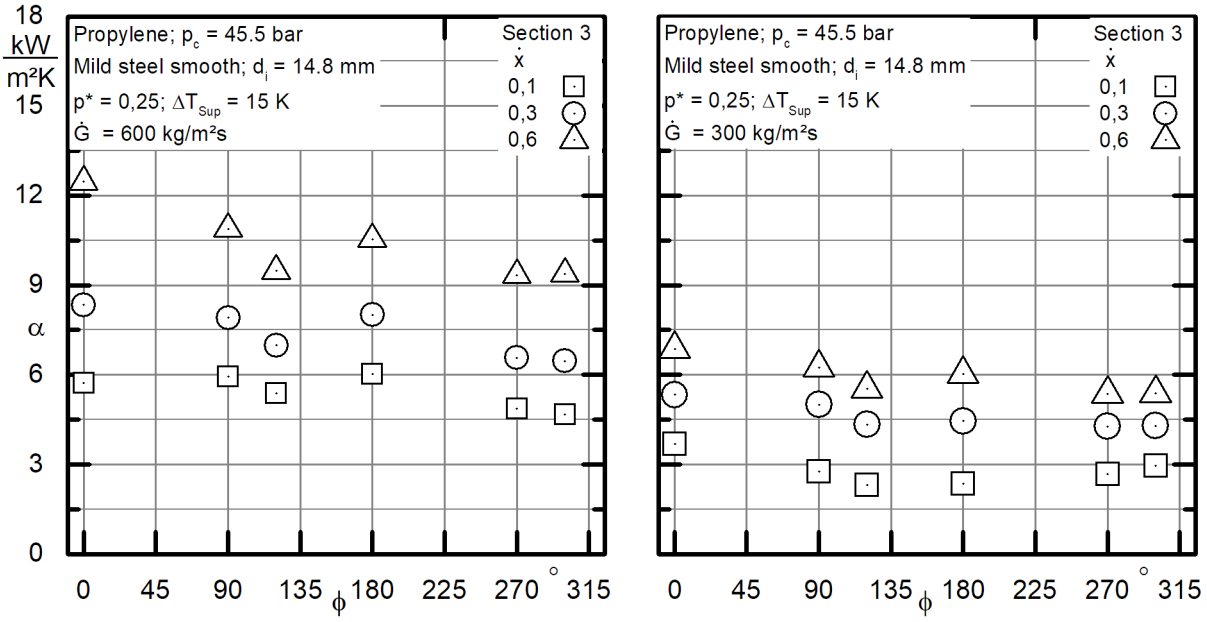

FIGURE 5.4 - LOCAL HEAT TRANSFER COEFFICIENTS IN SECTION 3; MASS FLUX EFFECT.

In general, it can be observed how the relative low differences in terms of temperature differences ΔT_{loc} result in considerable variations in heat transfer coefficients α_{loc} around the cross section.

The origin of this occurrence is to be looked for analyzing Eq. 4.31. In Eq. (4.31), the internal tube diameter d_{int}, the conductive thermal resistance

along of several layers of the tube R_{con} are constant. The local heat flux $\dot{Q}_{\Delta z,loc}$ is assumed to be constant on the radial direction ϕ. Even if this is physically incorrect, the goal is to evaluate solely the effect of temperature differences ΔT_{loc}.
Having done these assumptions, the local heat transfer coefficient α_{loc} is the function of a single variable: ΔT_{loc}.
As the local temperature difference ΔT_{loc} diminishes, the difference at the denominator shrinks and the resulting local heat transfer coefficient α_{loc} increases. It can be noted that, the equation that links the two variables presents an asymptotical behavior as the local temperature difference ΔT_{loc} gets smaller, reaching a hypothetical infinite heat transfer coefficient when the difference at the denominator is null.
This observation highlights the high sensitivity of the Data Reduction. Relatively small differences in local temperature differences ΔT_{loc} can lead to relatively big differences in heat transfer coefficients α_{loc}.
Considering TCs uncertainty, despite the calibration, and the fact that the temperature variations within the same measuring section are in the order of some tenths of Celsius degree, an even bigger uncertainty is transferred as consequence to the local heat transfer coefficients α_{loc}.
Furthermore, assuming a constant absolute uncertainty value, the more the local temperature difference ΔT_{loc} diminishes, the higher the percentage uncertainty becomes. For this reason, all the measurements characterized by a low ΔT_{loc}, and consequently a high α_{loc}, are coupled with a higher uncertainty on the heat transfer coefficient.
Carefully observing Fig. 5.3 and Fig. 5.4, it can be noted that local heat transfer coefficients α_{loc} follow a certain trend that appears to be inexplicable according to the known condensation theories. In case of stratified flow, it can be expected to have a lower local heat transfer coefficient α_{loc} in the lower part of the tube, $135° < \phi < 225°$, due to the high liquid layer thickness. The highest value of local heat transfer coefficient α_{loc} is indeed expected in the top part of the tube, $-45° < \phi < 45°$. In case of annular flow, a more even distribution of local heat transfer coefficient α_{loc} can be expected.

For some of the performed measurements, these described trends have not been observed.
Nevertheless, the observed trend seems to repeat itself with a certain constancy at the different vapor qualities x considered. This observation proves the non-random behavior of the data obtained. The observed effect seems to be related to the single thermocouple and not to condensation.
Some hypotheses for this behavior can be formulated, assessing all the external effects that might influence the temperature measurements on the test tube and consequently, on local heat transfer coefficients α_{loc}:

- *TCs uncertainty*
  Despite the calibration done and the calculation of an offset at ambient temperature, TCs maintain a given, non-null uncertainty.
- *Gluing*
  As explained in Chapter 3, the gluing process of the TCs on the test tube is critical. The gluing has been carried out manually and it is a process subject to imprecisions and mistakes. For this reason, each TC has been glued with a different glue layer thickness, determining a different local thermal resistance between the sensor and the oil flow. Moreover, being the annular very thin, with 6 mm between the test tube outer wall and the external tube, the glue layer shape could influence the oil velocity field. (Minimum effect)
- *Obstacles interacting with the oil flow*
  Inside the annular where the cooling oil flows, we can list several obstacles that undoubtedly influence the oil velocity field and so the local heat transfer on the oil side. The heat transfer on the oil side may be locally more efficient in some radial positions compared to others. Consequently, the measurement local temperature differences $\Delta T_{j,\phi}$ may be accordingly influenced. Inside the annular, the disturbance obstacles are: 20 RTDs positioned in an alternated pattern on the top and low side of the tube, the 6 sealed screws used for concentricity adjustment, the 24 TCs wires.

5.2 Local heat transfer

In this paragraph, the local temperature differences ΔT_{loc} and heat transfer coefficients α_{loc} are presented and commented. The comparison carried out for the local heat transfer considers a fixed cross section of the test tube, Section 3. This is done with the goal of having a more consistent comparison between the different test conditions considered. In fact, in this way, the local temperature differences ΔT_{loc} are always calculated taking into account the local wall temperatures $T_{wall,loc}$ measured by the same thermocouples. In Fig. 5.5, the disposition of TCs around the test tube for Section 3 is shown.

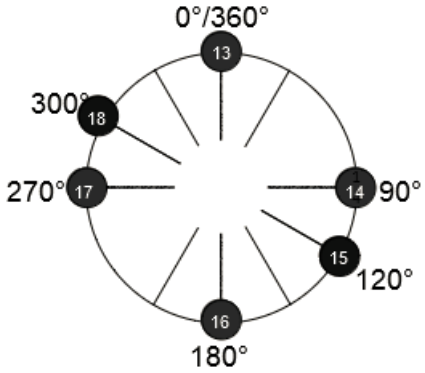

FIGURE 5.5 – TCS DISPOSITION IN MEASUREMENT SECTION 3

In the graphs presented, the local heat transfer coefficients α_{loc} and the temperature differences ΔT_{loc} are plotted as function of the radial direction ϕ.

For each measurement, three values of vapor quality are considered: $x = 0.1; 0.3; 0.6$.

The goal is to comment and analyze the experimental results, evaluating their trend under the different test conditions and speculating on the local heat transfer mechanisms occurring in the different portions of the test tube's circumference and the possible flow regimes occurring.

Measurement 1 - $p^* = 0.25$; $G = 600\ \frac{kg}{(m^2 s)}$

In Fig. 5.6 a couple of graphs is reported. The local temperature differences ΔT_{loc} and the local heat transfer coefficients α_{loc} are plotted as function of the radial direction ϕ. The results are referred to Measurement 1, $p^* = 0.25$; $G = 600\ \frac{kg}{(m^2 s)}$.

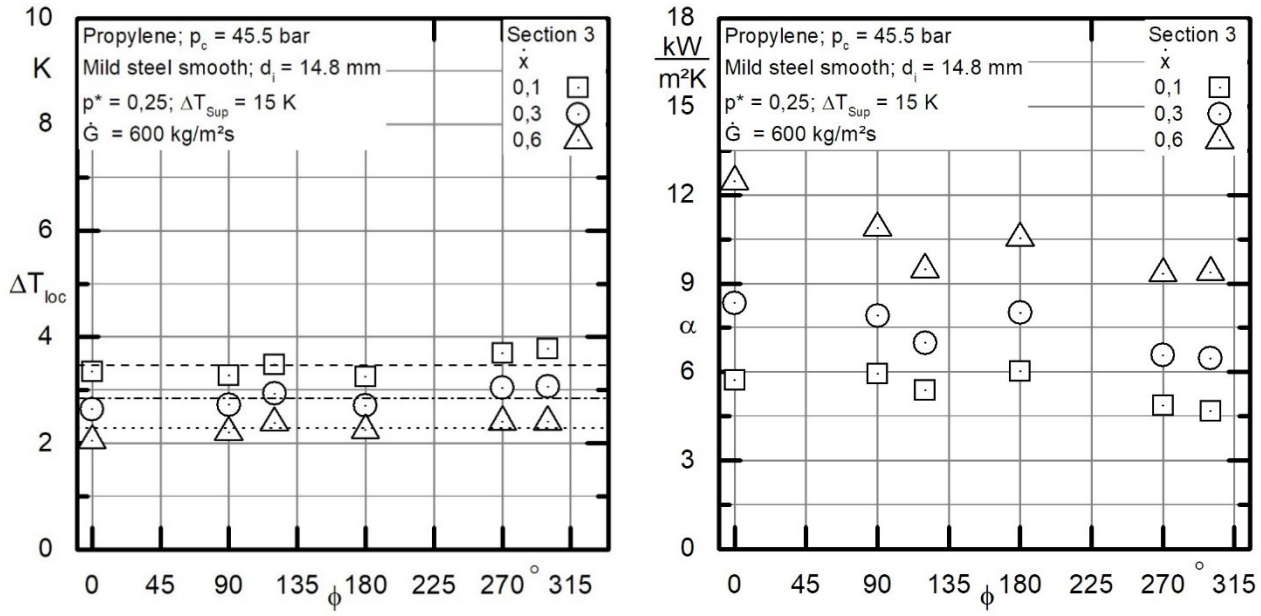

FIGURE 5.6 – LOCAL TEMPERATURE DIFFERENCE AND HEAT TRANSFER COEFFICIENT FOR MEASUREMENT 1

Measurement 1 is the test condition that exhibits the lowest values of local temperature differences ΔT_{loc}, to which the highest local heat transfer coefficients α_{loc} are associated. In fact, this measurement is carried out at the lowest reduced pressure p^* and the highest mass flux G considered. Both these factors increase the heat transfer.

On the left-hand side, the local temperature differences ΔT_{loc} are plotted as function of the radial direction ϕ for three different vapor qualities x examined. It can be observed that the variations of temperature within the cross section are very modest if compared with the average temperature difference, highlighted for each vapor quality x with a dotted line.

These temperature differences ΔT_{loc} are coupled, through the Data Reduction (Chapter 4), to local heat transfer coefficients α_{loc}, displayed in Fig. 5.6 on the right-hand side. The plotted data follow a downward trend as ϕ increases. It would have been expected to see a "parabolic trend", with the highest local heat transfer coefficient in the upper part of the tube, at ϕ close to $\phi = 0°$, where the liquid film should be thinner and the lowest in the lower part of the tube, at ϕ close to $\phi = 180°$, where the liquid film should be thicker. This would be theoretically predicted in both cases of stratified and annular flow although with a bigger difference between maximum and minimum in case of stratified flow.

It is very interesting to note that, as explained in the previous paragraph, small differences of temperature differences ΔT_{loc}, especially for $x = 0.6$,

result in considerable differences in local heat transfer coefficients α_{loc}. This observation may explain the seemingly inexplicable trend of local heat transfer coefficient α_{loc} according to the known condensation theories.

In Fig. 5.7 a photo of the two-phase flow of propylene is reported. The photo has been taken from the glass tube present at the inlet of the test section. It is worth to specify that the glass tube has a slighly bigger diameter d compared to the test tube. Therefore, the flow expands when it enters the glass tube, with an inevitable effect on the flow shape. The photo reported in Fig. … has been taken at $p^* = 0.25; G = 600\ \frac{kg}{(m^2 s)}; x = 0.3$.

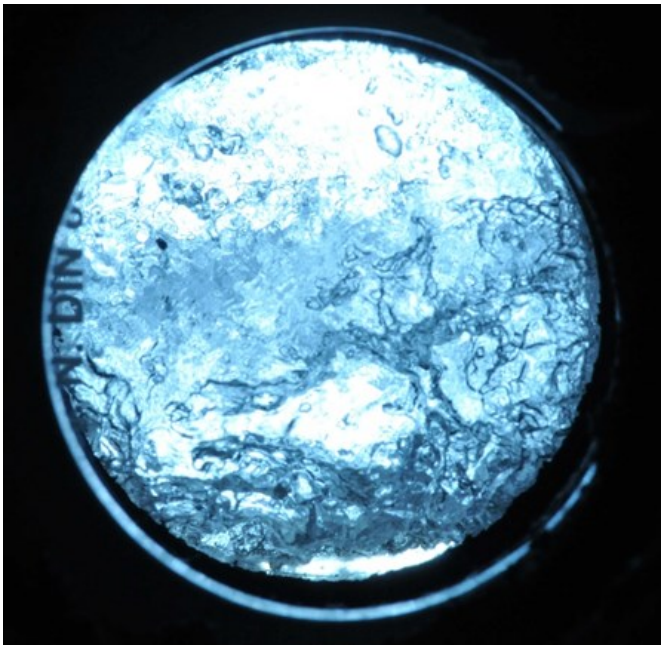

FIGURE 5.7 – PHOTO OF TWO-PHASE FLOW OF PROPYLENE FROM GLASS TUBE - $p^* = 0.25; G = 600\ \frac{kg}{(m^2 s)}; x = 0.3$.

The flow depicted shows a very high interaction between the two phases. This is not surprising if we consider the fact that low reduced pressure p^* and high mass flux G both enhance the engagement of one phase to the other. Despite the possibility to identify a thicker liquid layer in the lower part of the tube, the flow is highly turbulent and difficult to categorize in one the flow patterns described by flow pattern maps [8] [10].

The highly turbulent flow observable in Fig. 5.7, determines a difficulty in evaluating the liquid film thickness at a given radial position, being the layer continuously perturbated by the vapor phase. This may contribute

to explain the seemingly inexplicable trend of local heat transfer coefficient α_{loc} seen in Fig. ...

Measurement 2 - $p^* = 0.25; G = 300\ \frac{kg}{(m^2 s)}$

In Fig. 5.8 a couple of graphs is reported. The local temperature differences ΔT_{loc} and the local heat transfer coefficients α_{loc} are plotted as function of the radial direction ϕ. The results are referred to Measurement 2, $p^* = 0.25; G = 300\ \frac{kg}{(m^2 s)}$.

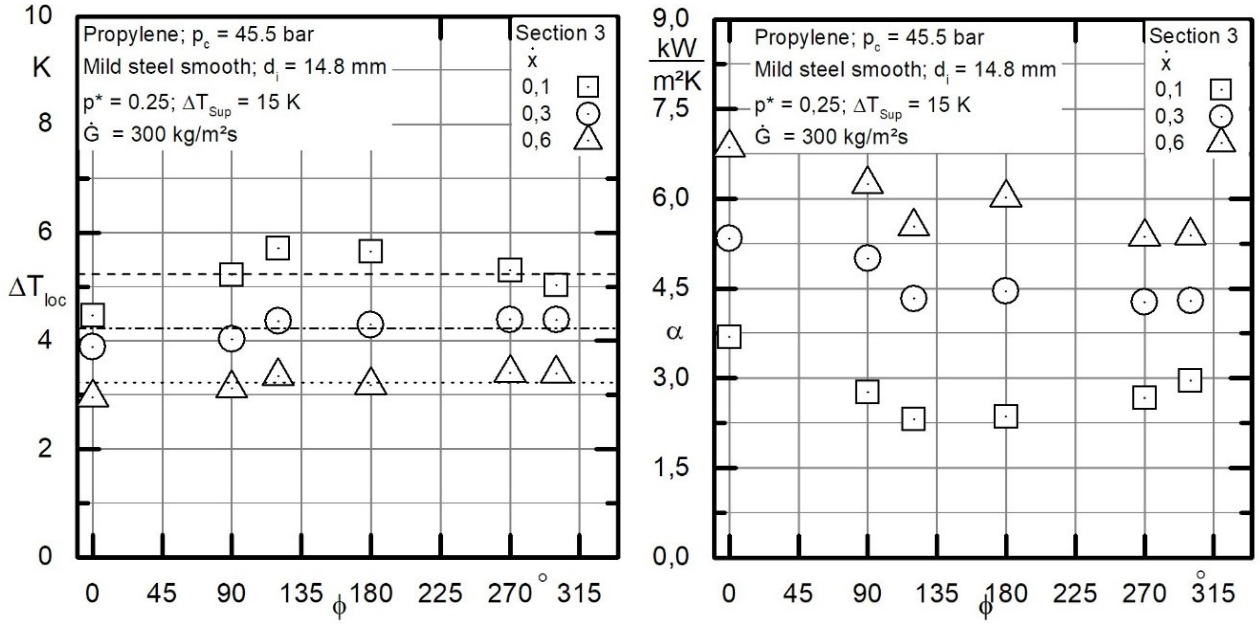

FIGURE 5.8 – LOCAL TEMPERATURE DIFFERENCE AND HEAT TRANSFER COEFFICIENT FOR MEASUREMENT 2

Measurement 2 is done at the lowest value of reduced pressure p^* and the lowest mass flux G. This test condition can be considered intermediate in terms of heat transfer. In fact, the heat transfer favored by low reduced pressure p^* is not supported by the low mass flux G.
On the left-hand side, the local temperature differences ΔT_{loc} are plotted as function of the radial direction ϕ for the three vapor qualities x examined. In this case, significative differences at different vapor qualities x can be noticed. For $x = 0.1$, the local temperature difference ΔT_{loc} is maximum in the portion of the tube, close to $\phi = 180°$ while it assumes the minimum value at $\phi = 0°$. The difference between maximum and minimum value is considerable, in the order of 1°C. For $x = 0.6$, the trend is much more difficult to identify, being the differences very small in both absolute and relative terms.

The temperature differences ΔT_{loc} are coupled, through Eq. (4.31), to local heat transfer coefficients α_{loc}, displayed in Fig. … on the right-hand side. Here, like for the local temperature differences ΔT_{loc}, considerable differences at different vapor qualities x can be noticed. For $x = 0.1$, a U-shape trend can be identified. The maximum value of heat transfer coefficient is measured at $\phi = 0°$ and the minimum value close to $\phi = 180°$. The difference between maximum and minimum value is considerable, in the order of $1.5\ \frac{kW}{m^2K}$. For $x = 0.6$, the trend exhibits the downward trend already noted for Measurement 1. It's interesting to observe that, despite the much smaller absolute and relative differences in temperature around the cross section if compared to $x = 0.1$, the absolute difference between maximum and minimum value in terms of local heat transfer coefficient α_{loc}, is similar, in the order of $1.5\ \frac{kW}{m^2K}$.
In Fig. 5.9 a photo of the two-phase flow of propylene is reported. The photo has been taken at $p^* = 0.25$; $G = 300\ \frac{kg}{(m^2s)}$; $x = 0.1$.

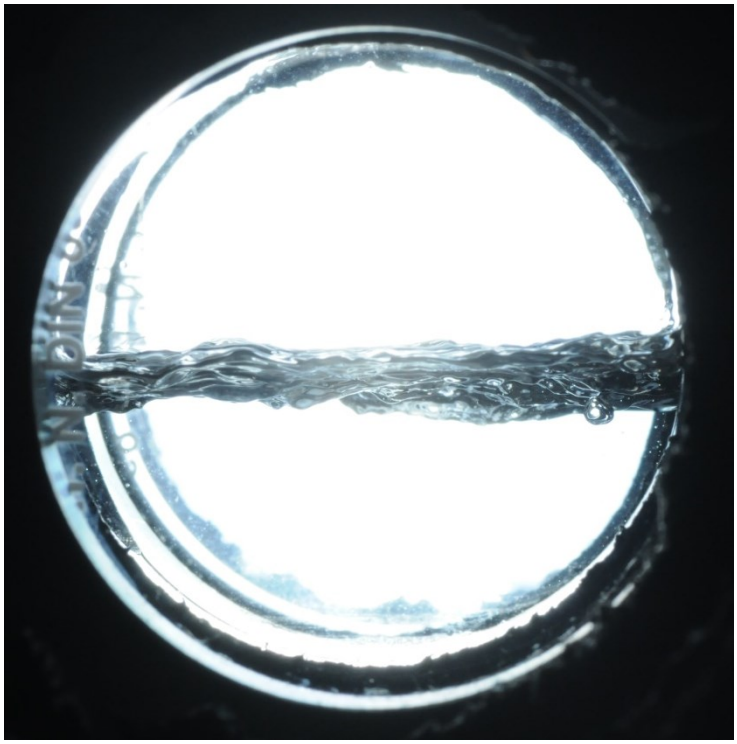

FIGURE 5.9 - PHOTO OF TWO-PHASE FLOW OF PROPYLENE FROM GLASS TUBE - $p^* = 0.25$; $G = 300\ \frac{kg}{(m^2s)}$; $x = 0.1$.

The photo displays a stratified flow. The liquid layer on the bottom part of the tube can be clearly observed. The upper portion of the tube is characterized by a thin layer of liquid that remains attached to the wall

due to adhesive forces between propylene and the tube wall. The liquid-vapor interface is relevantly perturbated by the vapor flow in the upper portion of the tube.
The assumption of stratified flow for $x = 0.1$, supported by the U-shape identified for the local heat transfer coefficient α_{loc}, seems to be confirmed by the vision of the flow regime.

Measurement 3 - $p^* = 0.5$; $G = 600\ \frac{kg}{(m^2 s)}$

In Fig. 5.10 a couple of graphs is reported. The local temperature differences ΔT_{loc} and the local heat transfer coefficients α_{loc} are plotted as function of the radial direction ϕ. The results are referred to Measurement 3, $p^* = 0.5$; $G = 600\ \frac{kg}{(m^2 s)}$.

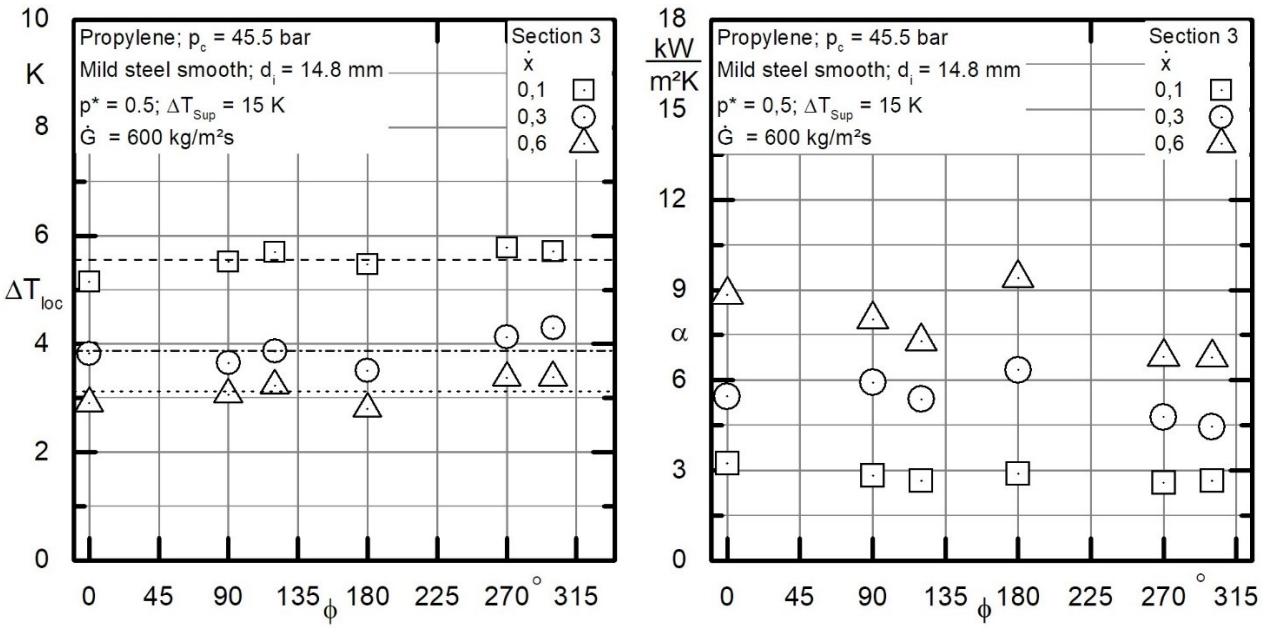

FIGURE 5.10 – LOCAL TEMPERATURE DIFFERENCE AND HEAT TRANSFER COEFFICIENT FOR MEASUREMENT 3

Measurement 3 is done at the highest value of reduced pressure p^* and the highest mass flux G. This test condition, like Measurement 2, can be considered intermediate in terms of heat transfer. In fact, the heat transfer favored by high mass flux G is not supported by the high reduced pressure p^*.
On the left-hand side, the local temperature differences ΔT_{loc} are plotted as function of the radial direction ϕ for the three vapor qualities x examined. Differently from Measurement 2, we don't observe important trend differences between the data collected a different vapor quality x.

The differences of temperature within the cross section are limited for all the considered vapor qualities x. Observing the corresponding local heat transfer coefficients α_{loc}, reported in the graph on the right-hand side, it can be noticed how a similar trend in local temperature differences ΔT_{loc}, gives as outcome a very different pattern of local heat transfer coefficients α_{loc}. For $x = 0.1$, a constant trend is observed with small variations as function of the radial direction ϕ. For $x = 0.6$, it is difficult to determine a trend due to the high variations in heat transfer coefficient associated with small radial direction ϕ variations.

In Fig. 5.11 a photo of the two-phase flow of propylene is reported. The photo has been taken at $p^* = 0.5$; $G = 600\ \frac{kg}{(m^2 s)}$; $x = 0.6$.

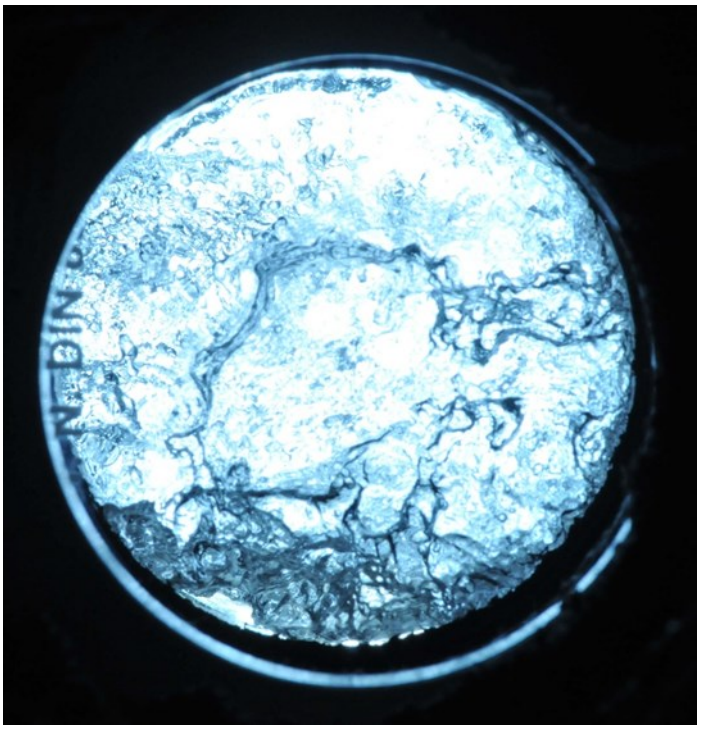

FIGURE 5.11 - PHOTO OF TWO-PHASE FLOW OF PROPYLENE FROM GLASS TUBE - $p^* = 0.5$; $G = 600\ \frac{kg}{(m^2 s)}$; $x = 0.6$.

As in Fig. 5.7 (Measurement 1), the flow depicted shows a very high interaction between the two phases. Despite the possibility to identify a thicker liquid in the lower part of the tube, the flow is highly turbulent and difficult to categorize in one the flow patterns described by flow pattern maps [8] [10].
The highly turbulent flow observable in Fig. …, determines a difficulty in evaluating the liquid film thickness at a given radial position, being the

layer continuously perturbated by the vapor phase. This may contribute to explain the seemingly inexplicable trend of local heat transfer coefficient α_{loc} seen in Fig. ...

Measurement 4 - $p^* = 0.5; G = 300\ \frac{kg}{(m^2 s)}$

In Fig. 5.12 a couple of graphs is reported. The local temperature differences ΔT_{loc} and the local heat transfer coefficients α_{loc} are plotted as function of the radial direction ϕ. The results are referred to Measurement 4, $p^* = 0.5; G = 300\ \frac{kg}{(m^2 s)}$.

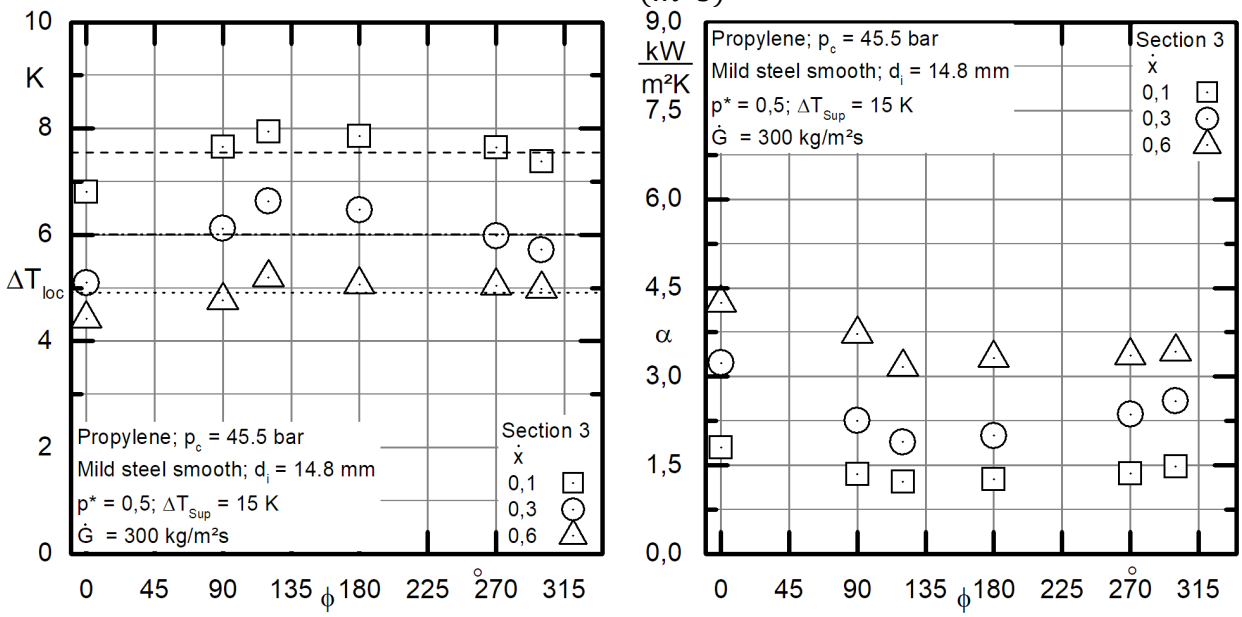

FIGURE 5.12 – LOCAL TEMPERATURE DIFFERENCE AND HEAT TRANSFER COEFFICIENT FOR MEASUREMENT 4

Measurement 4 is the test condition that exhibits the highest values of local temperature differences ΔT_{loc}, to which the lowest local heat transfer coefficients α_{loc} are associated. In fact, this measurement is carried out at the highest reduced pressure p^* and the lowest mass flux G considered.

On the left-hand side, the local temperature differences ΔT_{loc} are plotted as function of the radial direction ϕ for the three vapor qualities x examined. It can be observed that there's a considerable variation of temperature with the radial direction ϕ. These variations are very high at low vapor quality, $x = 0.1; x = 0.3;$ but are still relevant at high vapor quality, $x = 0.6$. Observing the corresponding local heat transfer coefficients α_{loc}, reported in the graph on the right-hand side, the characteristic U-shape is noticeable. The maximum value of local heat

transfer coefficient α_{loc} is associated with the top part of the tube, $\phi = 0°$, where the liquid film is thin and consequently, the thermal resistance is low. The bottom area of the tube, $\phi = 180°$, is characterized by the lowest heat transfer coefficient. This may be explained by the presence of thicker liquid layer in the occurrence of stratified flow. The lateral portions of the test tube, $\phi = 90°; \phi = 270°$, exhibit medium values of α_{loc}. This fact seems to confirm the previous hypothesis, indeed, the liquid film on the sides is medium thick.
In Fig. 5.13 a photo of the two-phase flow of propylene is reported. The photo has been taken at $p^* = 0.5$; $G = 300\ \frac{kg}{(m^2 s)}$; $x = 0.6$.

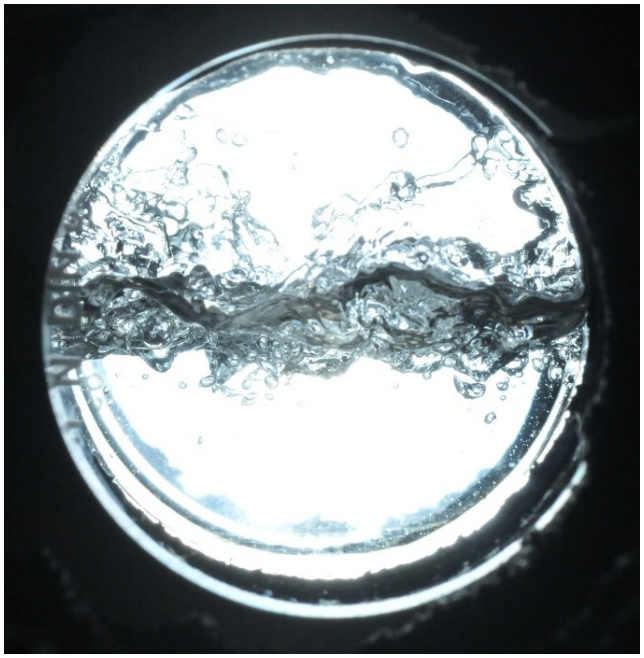

FIGURE 5.13 - PHOTO OF TWO-PHASE FLOW OF PROPYLENE FROM GLASS TUBE - $p^* = 0.5$; $G = 300\ \frac{kg}{(m^2 s)}$; $x = 0.6$.

The photo displays a stratified wavy flow. The liquid layer on the bottom part of the tube can be clearly observed. The upper portion of the tube is characterized by a thin layer of liquid that remains attached to the wall due to adhesive forces. The liquid-vapor interface is relevantly perturbated by the vapor flow in the upper portion of the tube.
The assumption of stratified flow, supported by the U-shape identified for the local heat transfer coefficient α_{loc}, seems to be confirmed by the vision of the flow regime.

5.3 Overall heat transfer

In this paragraph, the overall heat transfer is evaluated and commented for all the considered measurements.

Given a test condition, defined by fixed reduced pressure p^*, mass flux G and inlet vapor quality x, the overall heat transfer coefficient α is directly calculated from the local heat transfer coefficients α_{loc} described and commented in the previous paragraph. In particular, the average heat transfer coefficient for the single measurement section is calculated averaging the local heat transfer coefficients α_{loc} of that section. In this way, four values, one for each section, are obtained. Finally, the overall heat transfer coefficient α is calculated averaging the 4 values previously obtained.

In the following, two couples of graphs are presented and commented.

In the first, two different values of mass flux are plotted at fixed reduced pressure p^*, while in the latter, two different values of reduced pressure are plotted at fixed mass flux G.

In Fig. 5.14, the overall heat transfer coefficient is reported as function of the vapor quality x.

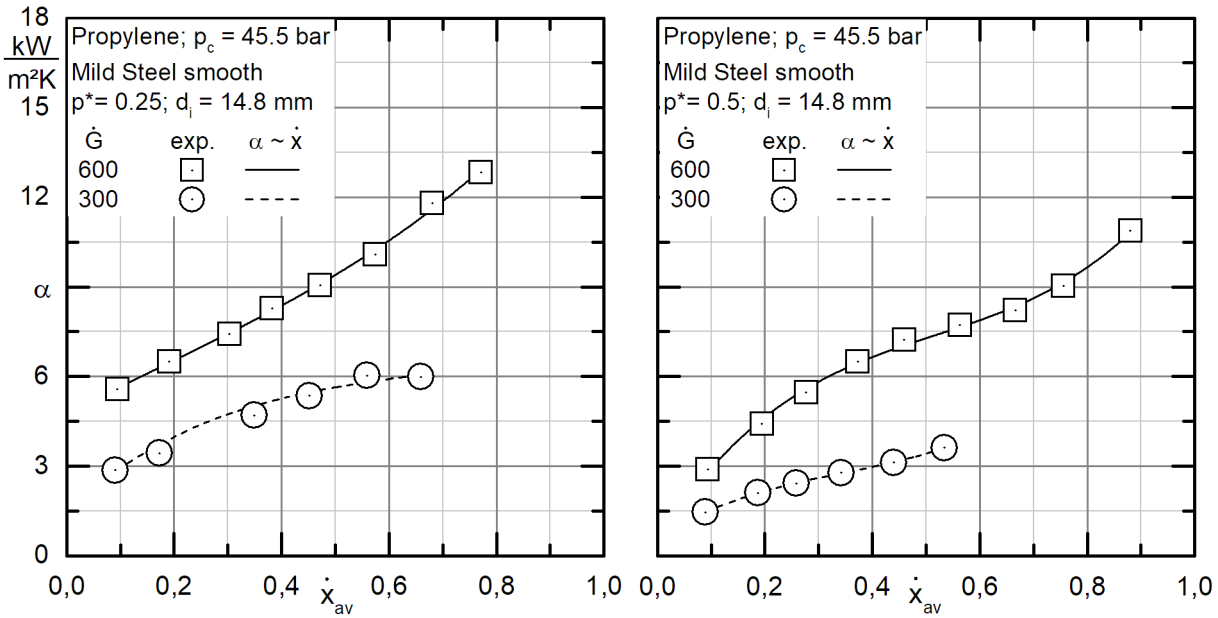

FIGURE 5.14 – OVERALL HEAT TRANSFER COEFFICIENT AS FUNCTION OF THE VAPOR QUALITY; EFFECT OF THE MASS FLUX

In the graph on the left-hand side, a comparison between the two values of mass flux G is done at constant reduced pressure, $p^* = 0.25$.

An increase of heat transfer coefficient with the vapor quality x can be observed for both values of mass flux G. At high mass flux G, the trend is nearly linear even if the increase is higher as the vapor quality x

increases. At low mass flux G, the trend is the opposite, with an increase that tend to lower at higher vapor quality x. Unfortunately, a complete comparison is not possible due to the lack of measurements at high vapor quality $x > 0.7$.

A high vapor quality x is generally associated with annular or mist flow. In these flow regimes, thermal resistance is mainly concentrated in the liquid film attached to the tube surface. A high vapor quality x is associated with a thinner film and therefore a lower thermal resistance, resulting in a higher overall heat transfer coefficient α.

An increase of heat transfer coefficient can be noticed with increasing the mass flux G. The increase of heat transfer coefficient is approximately equal to 80% between $G = 300 \frac{kg}{m^2 s}$ and $G = 600 \frac{kg}{m^2 s}$. This percentual increment though, varies quite considerably as function of vapor quality x.

The heat transfer coefficient α is, all other conditions being equal, higher in case of higher mass flux G. This is due to the dependency of the heat transfer coefficient on the velocity of the two-phase flow. As it is showed,

$$G = \frac{\dot{m}_{tot}}{A} = \frac{\rho \cdot \dot{V}_{tot}}{A} = \frac{\rho u A}{A} = \rho u \tag{5.1}$$

The mass flux G, is directly proportional to the flow velocity.

As the single-phase heat transfer theory suggests,

$$Nu = f(Re, Pr). \tag{5.2}$$

A higher value of mass flux G is indeed coupled with a higher velocity inside the tube and so a higher Re-number and as consequence, with a higher Nu-number, representing an enhanced convective heat transfer. It is also worth to remember that a higher mass flux G can lead to a change in the flow regime, and as a result, to a change in the heat transfer mechanism.

In the graph on the right-hand side, the heat transfer coefficient at different mass fluxes G is compared at constant reduced pressure, $p^* = 0.5$.

Similar statements to the ones done for the lower reduced pressure p^* can be done. At high mass flux G, in this case, the experimental points show a steep increase at low vapor quality x, the steepness decreases in the central values of x, to increase again for high values of vapor quality

x. At low mass flux G, the trend remains more linear. In addition, the effect of mass flux G on the heat transfer coefficient is percentagewise more important as vapor quality x increases.
At higher reduced pressure p^*, it can be noted that the effect of mass flux G is more important than at low pressure p^*, with a difference between the heat transfer coefficients approximately equal to 100% between the two mass fluxes G considered.
This may be caused by the different flow regimes that occur within the tube in the different thermodynamic conditions evaluated. It could also be possible that this is due to the uncertainty in the measurements acquired. In Fig. 5.15, the overall heat transfer coefficient is reported as function of the vapor quality x.

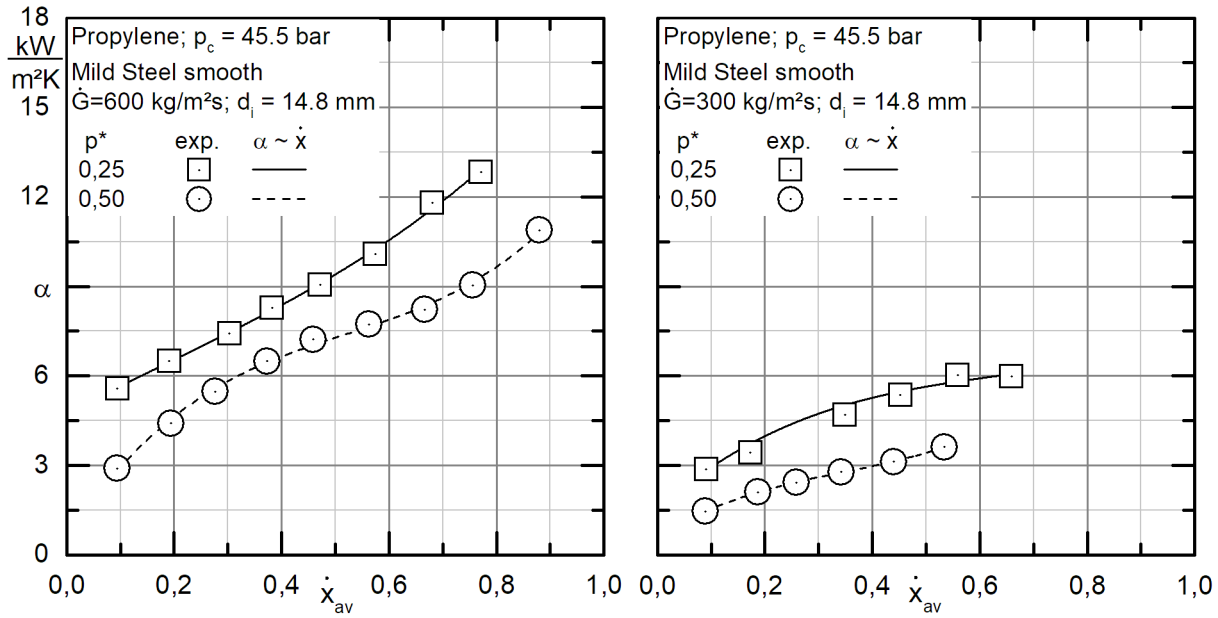

FIGURE 5.15 - OVERALL HEAT TRANSFER COEFFICIENT AS FUNCTION OF THE VAPOR QUALITY; EFFECT OF THE PRESSURE

In the graph on the left-hand side, a comparison between the two values of reduced pressure p^* is done at constant mass flux, $G = 600\ \frac{kg}{m^2 s}$. It can be observed how a lower pressure, at the same vapor quality, gives rise to a higher value of heat transfer coefficient.
This fact can be explained by analyzing the properties of the two phases at different pressures.
In Table 5.2, some propylene thermodynamic properties are reported for the two values of reduced pressure p^* set.

TABLE 5.2 – PROPYLENE THERMODYNAMIC PROPERTIES

p^*	$h_V - h_L$	ρ_L	ρ_V	$\rho_L - \rho_V$	μ_L	λ_L
	$[kJ/kg]$	$[kg/m^3]$	$[kg/m^3]$	$[kg/m^3]$	$[Pa * s]$	$[W/mK]$
0.25	335.85	507.15	24.07	483.08	$9.63 \cdot 10^{-5}$	0.1131
0.5	264.93	446.25	51.86	394.39	$7.09 \cdot 10^{-5}$	0.0963

Nusselt's theory for film-wise condensation proved several key dependencies between thermodynamics properties and condensation heat transfer coefficient.

According to Nusselt's theory, the average value of heat transfer coefficient over the entire surface of a vertical wall, of length L_{wall}, is equal to:

$$\bar{\alpha} = 0.943 \left[\frac{\lambda_L^3 g \rho_L (\rho_L - \rho_V)(h_V - h_L)}{\mu_L L_{wall} (T_s - T_{wall})} \right]^{\frac{1}{4}}. \quad (5.3)$$

Even though Eq. (5.3) is not applicable in case of flow condensation, it has been supported by several studies that the dependencies discovered by Nusselt between the heat transfer coefficient α and some key variables are valid for flow condensation. In this regard, Cavallini et al. [30] investigated the influence of the temperature difference $T_s - T_{wall}$ related to the flow condensation conditions, differentiating between a $\Delta T - dependent$ and $\Delta T - independent$ region. Like discussed in chapter 2.2 Thome [19] and Shah [20] included modified version of the Nusselt's equation for the heat transfer coefficient in their heat transfer models (See Eq. (2.45) and (2.54)).

At low reduced pressure, $p^* = 0.25$:

- Enthalpy of condensation (or vaporization) $(h_V - h_L)$, at the numerator, is higher than at $p^* = 0.5$.
- Density of the liquid ρ_L, at the numerator, is higher than at $p^* = 0.5$.

  A higher liquid density is associated with a higher Re-number in the liquid phase and therefore and increased convection heat transfer with the wall. As a result, the liquid layer tends to be thinner, and the associated thermal resistance is lower.
- Density difference between liquid and vapor $(\rho_L - \rho_V)$, at the numerator, is higher than at $p^* = 0.5$.

At higher density difference, the liquid is more squeezed toward the tube wall.

- Thermal conductivity of the liquid λ_L, at the numerator and raised to the third, is higher than at $p^* = 0.5$.
  A higher thermal conductivity enhances conduction in the liquid layer.
- Dynamic viscosity of the liquid μ_L, at the denominator, is higher than at $p^* = 0.5$.
  Higher dynamic viscosity tends to increase the viscous forces in the liquid layer. This fact reduces the liquid Re-number and a lower interaction between the two phases.

All these dependencies, except for the last one, tend to increase the heat transfer coefficient at lower pressure.

The effect of the temperature difference $(T_s - T_{wall})$ at different pressures is more difficult to predict, not being a substance property.

Anyway, observing the results reported in the previous paragraph, regarding local temperature differences ΔT_{loc}, it can be stated that temperature differences are lower in case of low reduced pressure $p^* = 0.25$. It is worth to specify that the temperature difference $(T_s - T_{wall})$ is not equal to the local temperature differences ΔT_{loc} measured thanks to the TCs. Indeed, thermocouples are positioned on the external wall of the test tube, while the temperature T_{wall} in Eq. (5.3) is the inner wall temperature. Nevertheless, the two temperature differences are strongly connected. The local temperature differences ΔT_{loc} also consider the conductive thermal resistance of the test tube on the radial direction.

According to equation (5.3), a lower temperature difference $(T_s - T_{wall})$, is associated with a higher heat transfer coefficient α.

At high reduced pressure $p^* = 0.5$, the experimental heat transfer coefficient obtained is lower than a lower pressure, for all the vapor qualities x considered. At low vapor quality $x = 0.1$, the relative difference is very high, with an increase of heat transfer coefficient of about 100% at lower pressure. This relative difference shrinks for medium values of vapor quality $x = 0.5$, to about 20%. At higher vapor quality x, the relative difference spread again. At $x = 0.8$, it is around 30%.

This observation suggests that the effect of pressure is not constant, but it depends on vapor quality x. This may be caused by the different flow

regimes that occur within the tube in the different thermodynamic conditions evaluated. It could also be possible that this is due to the uncertainty in the measurements acquired.
In the graph on the right-hand side, the same comparison is done at constant mass flux, $G = 300\ \frac{kg}{m^2 s}$. Similar considerations to the ones done for the higher mass flux G can be done.
In this case, the trend at high reduced pressure $p^* = 0.5$ doesn't differ so much from the one at lower pressure $p^* = 0.25$. Unfortunately, the lack of experimental data for $x > 0.6$, prevents a complete comparison. Nevertheless, it can be noted that the effect of pressure is not the same observed at higher mass flux G and that the effect of pressure is generally more evident percentagewise at low mass flux G. This may be caused by a change in flow regime or by the uncertainties of the experimental results.

5.3.1 Comparison of the experimental overall heat transfer coefficient with the literature

In this paragraph, the experimentally calculated overall heat transfer coefficients are compared with Shah's [20] and Thome's [19] correlations presented in Chapter 2.
The fitting between the experimental data and the correlations considered is evaluated for the four test combinations of reduced pressure p^* and mass flux G.
In Fig. 5.16, the heat transfer coefficient is reported as function of the vapor quality. The two graphs reported describe two different test conditions, Measurement 2 ($p^* = 0.25$; $G = 300\ \frac{kg}{m^2 s}$;) and Measurement 4 ($p^* = 0.5$; $G = 300\ \frac{kg}{m^2 s}$;).

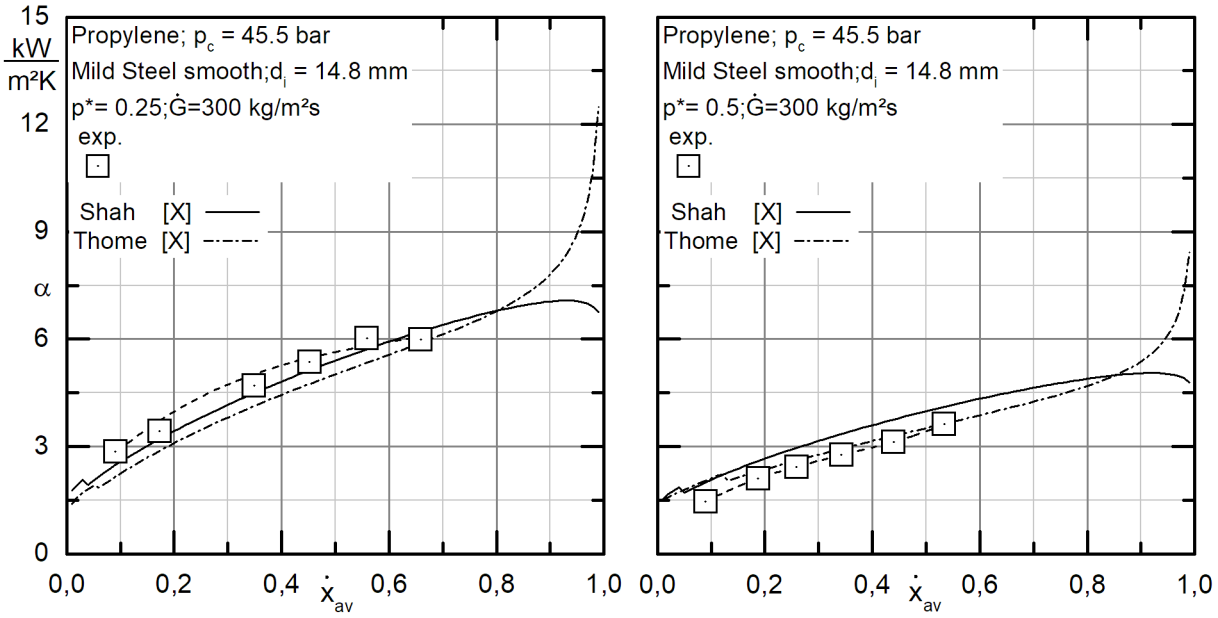

FIGURE 5.16 – COMPARISON BETWEEN THE EXPERIMENTALLY MEASURED VALUES AND THE VALUES PREDICTED BY SHAH'S [20] AND THOME'S [19] CORRELATIONS.

The square marks represent the experimentally measured heat transfer coefficient values, while the solid line identifies Shah's correlation function and the dashed line Thome's correlation function. In the graph on the left-hand side, the reduced pressure $p^* = 0.25$ and the mass flux $G = 300\ \frac{kg}{m^2 s}$ are investigated.

Shah's correlation predicts the heat transfer coefficient with a good accuracy. All the experimental points are slightly above Shah's curve except the last one, for $x = 0.7$.

Thome's correlation, slightly underestimates the heat transfer coefficient. The trend of the experimentally derived points is followed with good accuracy until about $x = 0.7$. Unfortunately, the lack of measurements at higher vapor quality x doesn't allow to assess the accuracy of the correlation in those conditions where the predicted heat transfer coefficient steeply increases with an asymptotical behavior at $x = 1$. This is due to the definition of the heat transfer model by Thome, indeed, it is supposed that the liquid layer shrinks progressively, until reaching null thickness at $x = 1$.

Nevertheless, at such a high quality x, being the mass of the liquid so small compared to that of the vapor, some portions of the tube may be dry, i.e., the vapor phase is directly in contact with the tube wall. This fact, known in the field of evaporation research as dry-out, should lead to lower values of the heat transfer coefficient compared to what is

expected by Thome's correlation. The mechanism governing heat transfer in dry-out is convection between the gas and the wall. Unfortunately, it was not possible to conduct experimental tests at high vapor quality, $x > 0.7$, to evaluate this phenomenon.

In the graph on the right-hand side, the reduced pressure $p^* = 0.5$ and the mass flux $G = 300\ \frac{kg}{m^2 s}$ are investigated.

At higher pressure p, both correlations exhibit a similar trend to the one of the experimental data.

Shah's correlation overestimates the experimental data, with a greater offset compared to Thome's correlation. The latter estimates the results with good accuracy, despite a small overestimation offset.

Also in this case, unfortunately, it was not possible to carry out tests at vapor quality $x > 0.6$ to assess the accuracy of Thome's correlation in particular.

In Fig. 5.17, the heat transfer coefficient is reported as function of the vapor quality. The two graphs reported describe two different test conditions,

Measurement 1 ($p^* = 0.25; G = 600\ \frac{kg}{m^2 s}$;) and Measurement 3 ($p^* = 0.5; G = 600\ \frac{kg}{m^2 s}$;).

The legend is the same already explained for Fig. 5.7.

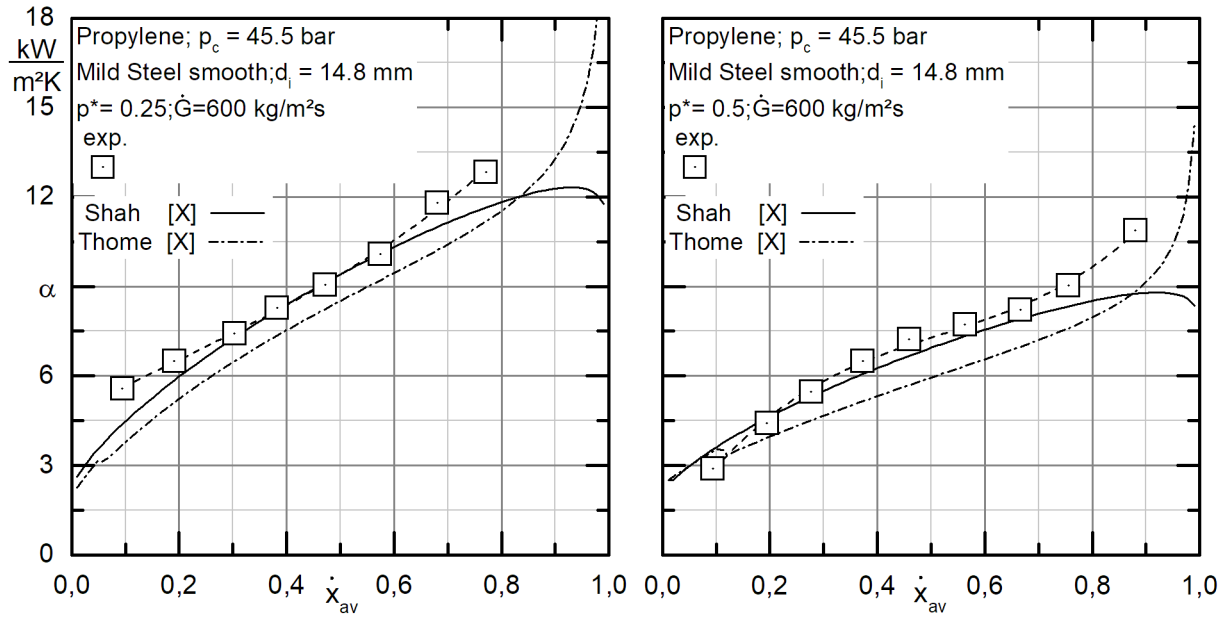

FIGURE 5.17 - COMPARISON BETWEEN THE EXPERIMENTALLY MEASURED VALUES AND THE VALUES PREDICTED BY SHAH'S [20] AND THOME'S [19] CORRELATIONS.

In the graph on the left-hand side, the reduced pressure $p^* = 0.25$ and the mass flux $G = 600\ \frac{kg}{m^2 s}$.
Shah's correlation overestimates the heat transfer coefficient at low vapor quality, $x < 0.3$ and at high vapor quality, $x > 0.6$. Instead, for medium vapor qualities, $0.3 \leq x \leq 0.6$, the predicted heat transfer coefficient is nearly identical to the measured one. This obviously means that the overall trend is not properly predicted by Shah's correlation curve.
Thome's correlation curve shows an almost constant offset as the vapor quality x varies. In particular, the correlation underestimates the experimental results. However, the trend is well better predicted than Shah's correlation.
In the graph on the right-hand side, the reduced pressure $p^* = 0.5$ and the mass flux $G = 600\ \frac{kg}{m^2 s}$.
In this case, Shah's correlation forecasts the heat transfer coefficient with a good accuracy for low and medium vapor qualities x, until it reaches $x = 0.7$. At higher vapor quality x the correlation curve underestimates the measured values.
Thome's correlation like at low reduced pressure, follows quite well the data trend even if at high vapor quality x, the offset between the curve and the data tends to increase. Overall, Thome's correlation underestimates the collected experimental data.

In Fig 5.18, Shah's correlation is assessed in comparison with the experimental data in a parity plot. The graph reports Shah's calculated heat transfer coefficient α_{calc}, on the y-axis, as function of the experimentally measured heat transfer coefficient α_{exp}, on the x-axis. In the graph, the solid line identifies the bisector, and the three dotted lines represent the percentual deviation of the calculated values from the experimental results.

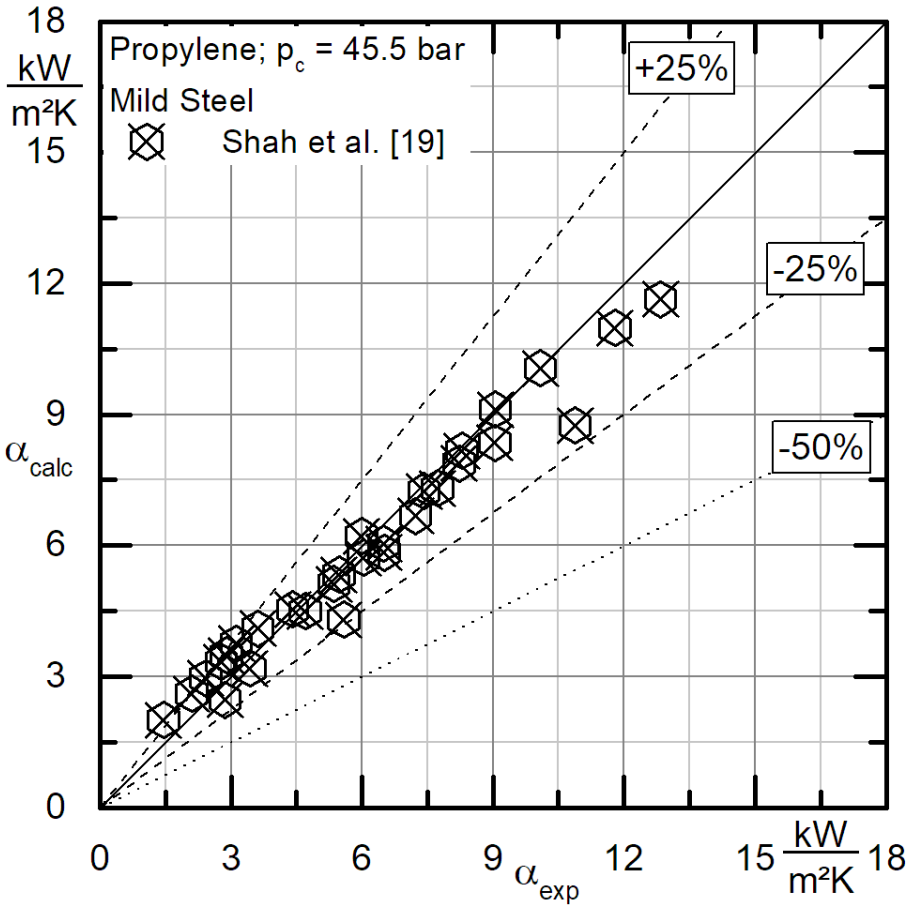

FIGURE 5.18 – PARITY PLOT FOR SHAH'S [20] CORRELATION

It can be observed that almost every measured point, above 95%, lies in the area identified by the two straight lines representing a positive or negative deviation of 25% from the bisector.

In Fig 5.19, Thome's correlation is assessed in comparison with the experimental data in a parity plot. The graph reports Thome's calculated heat transfer coefficient α_{calc}, on the y-axis, as function of the experimentally measured heat transfer coefficient α_{exp}, on the x-axis. As in Fig 5.18, the bisector is identified by a solid line while the three dotted lines represent the percentual deviation of the calculated values from the experimental results.

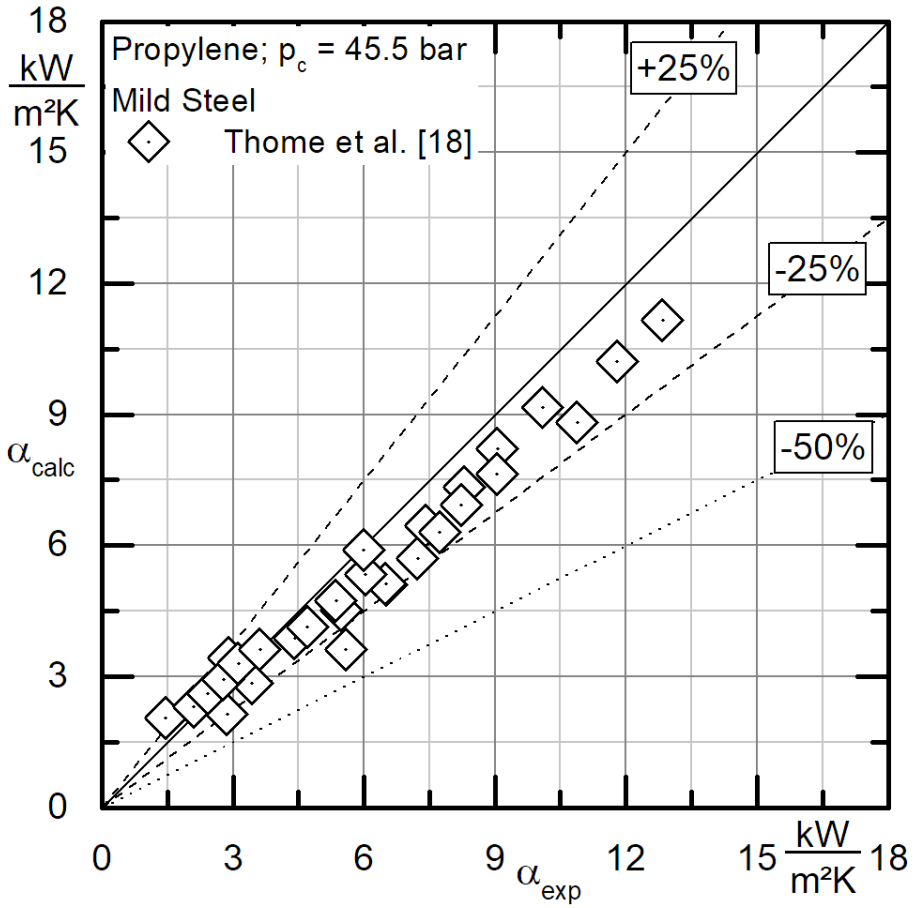

FIGURE 5.19 - PARITY PLOT FOR THOME'S [19] CORRELATION

As observed for Shah's correlation, it can be noted that almost every measured point, above 90%, lies in the area identified by the two straight lines representing a positive or negative deviation of 25% from the bisector.

5.4 Experimental pressure drops

In the following, two couples of graphs are presented and commented.

In Fig. 5.20, the total pressure drops $\left(\frac{\Delta p}{\Delta L}\right)_{tp}$ along the test tube is reported as function of vapor quality x.

The pressure drop $\left(\frac{\Delta p}{\Delta L}\right)_{tp}$ is measured by a differential pressure measuring device with one sensor per each end of the tube.

The pressure drops $\left(\frac{\Delta p}{\Delta L}\right)_{tp}$ are reported as specific value, per unit of length and measured in $\left[\frac{mbar}{m}\right]$.

As explained in Chapter 2, the total pressure drops $\left(\frac{\Delta p}{\Delta L}\right)_{tp}$ along the test tube are the result of the summation of three components: frictional, hydrostatic and acceleration (Eq. 2.58). In our case study, the frictional pressure drops $\left(\frac{\Delta p}{\Delta L}\right)_{tp,f}$ are by far the most important, being equal to about 80% [27] of the total ones.

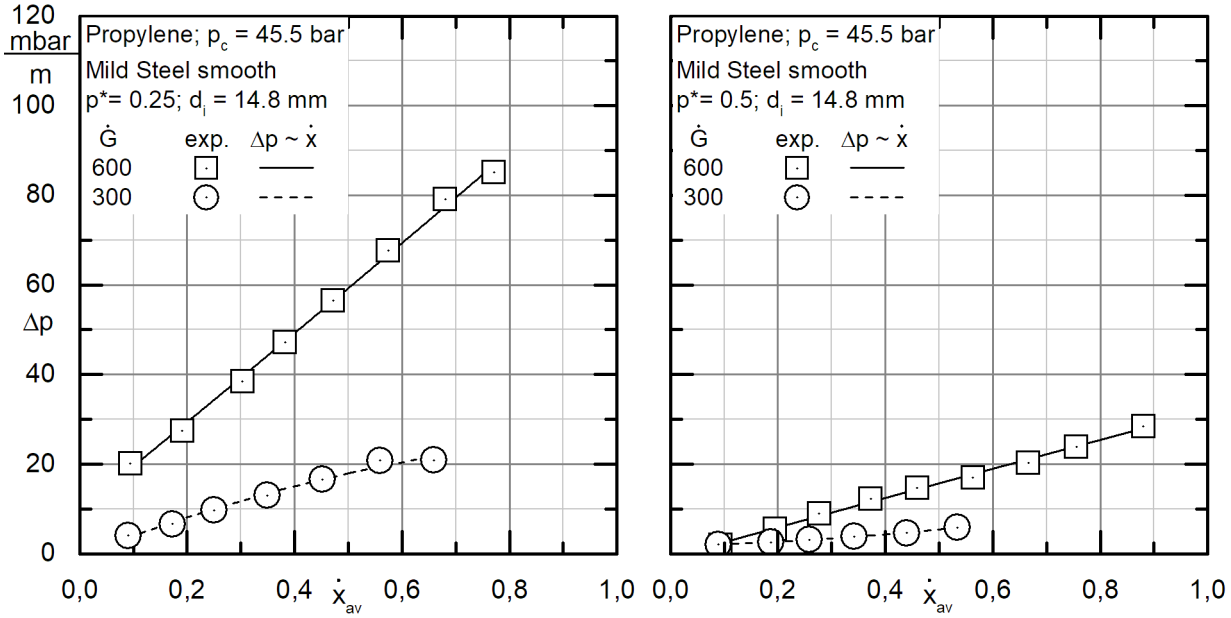

FIGURE 5.20 – PRESSURE DROPS AS FUNCTION OF VAPOR QUALITY; EFFECT OF MASS FLUX

In the graph on the left-hand side, a comparison between the two values of mass fluxes G is done at constant reduced pressure, $p^* = 0.25$.
For both values of mass flux G, a steep and almost perfectly linear increase of pressure drops $\left(\frac{\Delta p}{\Delta L}\right)_{tp}$ can be observed as vapor quality increases.
As the vapor quality increases, the difference of velocity between phases,

$$\Delta u = u_V - u_L \tag{5.4}$$

according to continuity equation, increases. The shear stress, from which the frictional pressure drops $\left(\frac{dp}{dz}\right)_{tp,f}$ depends, are proportional to the gradient of velocity $\frac{du}{dr}$ along the direction perpendicular to the flow r, in the region of the liquid-vapor interface. In particular,

$$\left(\frac{dp}{dz}\right)_{tp,f} \propto \int \tau_V dz \tag{5.5}$$

Moreover, the tangential shear stress τ_V exerted by the vapor on the liquid is defined [7] as,

$$\tau_V = \frac{f_V G_V^2}{2\rho_V} \tag{5.6}$$

where,

$$G_V = \frac{\dot{m}_{tot} \cdot x}{A}. \tag{5.7}$$

A proportionality exists between vapor quality x and frictional pressure drops $\left(\frac{dp}{dz}\right)_{f,2Ph}$.

As the vapor quality x increases, the two lines spread more or more but, despite this, the percentual difference at constant vapor quality x remains approximately constant. At high mass flux $G = 600\ \frac{kg}{m^2 s}$, the pressure drops $\left(\frac{\Delta p}{\Delta L}\right)_{tp}$ are about 3 times higher than at low mass flux G. At $G = 300\ \frac{kg}{m^2 s}$, a decrease of the steepness of the curve can be noticed as the vapor quality x increases. This fact is only lightly visible at the higher mass flux G, between $x = 0.6$ and $x = 0.7$.

In the graph on the right-hand side, the same comparison is done at constant reduced pressure, $p^* = 0.5$. Similar considerations to the ones done for the lower reduced pressure p^* can be done. In this case, the pressure drops $\left(\frac{\Delta p}{\Delta L}\right)_{tp}$ are, in general, much lower. Moreover, the trend for $G = 300\ \frac{kg}{m^2 s}$, cannot be completely analyzed due to the lack of measurement above $x = 0.6$.

Furthermore, at both pressure levels, we see that the pressure drops $\left(\frac{\Delta p}{\Delta L}\right)_{tp}$ are higher with higher values of mass flow G. From the definition of mass flow rate $\dot{m}$, we can observe that, for the same pipe, a higher value of G corresponds to a higher velocity u inside the pipe. The shear stress τ along the tube wall and between the two phases, on which

frictional pressure drops $\left(\frac{\Delta p}{\Delta L}\right)_{tp,f}$ depend, are proportional to the velocity gradient in the region near the wall of the pipe. Since according to fluid dynamics, velocity u is null at the wall surface, as the velocity u inside the pipe increases, the velocity gradient $\frac{du}{dr}$, along the direction perpendicular to the flow r, increases accordingly. Therefore, at high mass flux G, high frictional pressure drops $\left(\frac{\Delta p}{\Delta L}\right)_{tp,f}$ are expected.

In Fig. 5.21, the pressure drops $\left(\frac{\Delta p}{\Delta L}\right)_{tp}$ along the test tube are reported as function of vapor quality x.

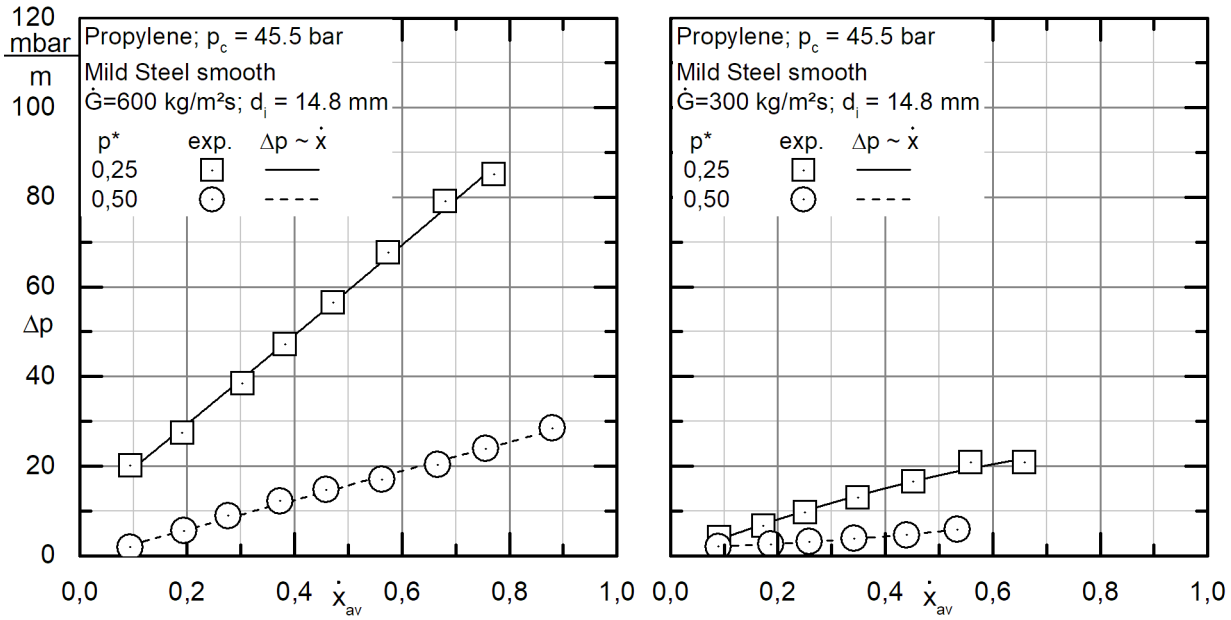

FIGURE 5.21 - PRESSURE DROPS AS FUNCTION OF VAPOR QUALITY; EFFECT OF PRESSURE

In the graph on the left-hand side, a comparison between two values of reduced pressure p^* is done at constant mass flux, $G = 600\ \frac{kg}{m^2 s}$.

It can be observed that, at constant vapor quality x, the pressure drops $\left(\frac{\Delta p}{\Delta L}\right)_{tp}$ are higher at lower pressure p^*. The percentual difference between the two curves is approximately constant, with the pressure drops $\left(\frac{\Delta p}{\Delta L}\right)_{tp}$ at $p^* = 0.25$ being around 3 times higher than at $p^* = 0.5$.

At lower pressure p, the density of the vapor ρ_V diminishes and as result, the tangential shear stress τ_V exerted by the vapor on the liquid at the interface [7],

$$\tau_V = \frac{f_V G_V^2}{2\rho_V}, \tag{5.6}$$

is higher. Since the pressure drops $\left(\frac{\Delta p}{\Delta L}\right)_{tp}$ are strongly bonded with the tangential shear stress τ_V exerted on the tube wall, this explains the higher frictional pressure drops $\left(\frac{\Delta p}{\Delta L}\right)_{tp,f}$ at lower pressure p.

The overall trend of the pressure drops $\left(\frac{\Delta p}{\Delta L}\right)_{tp}$ as function of vapor quality x is almost perfectly linear for both values of reduced pressure p^* considered.

In the graph on the right-hand side, the same comparison is done at constant mass flux, $G = 300\ \frac{kg}{m^2 s}$.

Similar considerations to the ones done for the lower mass flux can be done. Obviously, compared to the higher mass flux G, the two curves are shifted downwards.

Having concluded the analysis of the two-phase pressure drops $\left(\frac{\Delta p}{\Delta L}\right)_{tp}$, we can compare them with the overall heat transfer coefficients α analyzed in the previous paragraph.

It can be observed that the conditions that exhibit a high overall heat transfer coefficient are coupled with a high value of total pressure drops $\left(\frac{\Delta p}{\Delta L}\right)_{tp}$.

These conditions are:

- Low reduced pressure p^*
- High mass flux G
- High vapor quality x

All these conditions are associated with a high velocity, and they favor the interaction between the two phases.

5.4.1 Comparison of the experimental pressure drops with literature

In this paragraph, the experimentally measured pressure drops are compared with Muller-Steinhagen's [28] and Friedel's [27] correlation.

In Fig. 5.22, the pressure drops $\left(\frac{\Delta p}{\Delta L}\right)_{tp}$ along the tube are reported as function of the vapor quality x. The two graphs reported describe two different test conditions, Measurement 2 ($p^* = 0.25$; $G = 600\ \frac{kg}{m^2 s}$;) and Measurement 4 ($p^* = 0.5$; $G = 300\ \frac{kg}{m^2 s}$;).

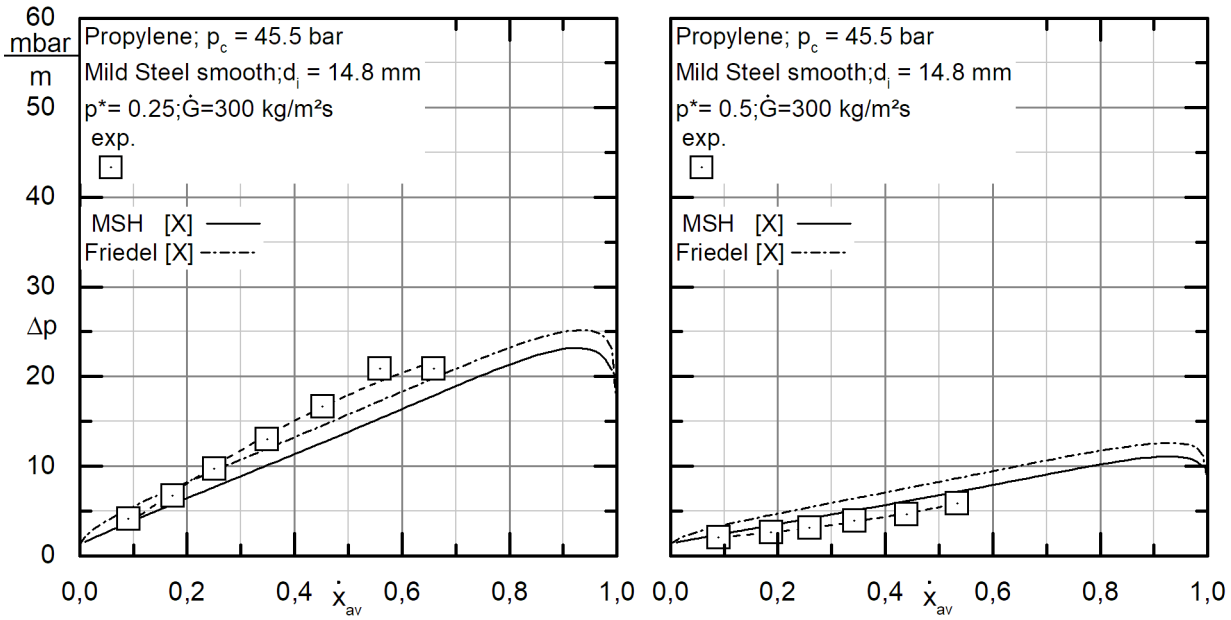

FIGURE 5.22 - COMPARISON BETWEEN THE EXPERIMENTALLY MEASURED VALUES OF PRESSURE DROPS AND THE VALUES PREDICTED BY MULLER-STEINHAGEN'S [28] AND FRIEDEL [27] CORRELATIONS.

The square marks represent the experimentally measured pressure drops $\left(\frac{\Delta p}{\Delta L}\right)_{tp}$, while the solid line identifies Muller-Steinhagen's correlation function [28] and the dashed line Friedel's [27] correlation function.

In the graph on the left-hand side, the reduced pressure $p^* = 0.25$ and the mass flux $G = 300\ \frac{kg}{m^2 s}$.

Muller-Steinhagen's correlation underestimates the experimental data for all the values of vapor quality x measured. The offset is higher at higher vapor quality x. Indeed, the steepness of the line that interpolates the experimental data is higher than the correlation curve.

Overall, Friedel's correlation fits the measured pressure drops $\left(\frac{\Delta p}{\Delta L}\right)_{tp}$ better than Muller-Steinhagen's one. Nevertheless, also in this case, the offset tends to increase as the vapor quality x increases.

In the graph on the right-hand side, the reduced pressure $p^* = 0.5$ and the mass flux $G = 300\ \frac{kg}{m^2 s}$.

In this case, the experimental data are available only until $x = 0.6$. Muller-Steinhagen's correlation shows a quite good accuracy in forecasting the pressure drops $\left(\frac{\Delta p}{\Delta L}\right)_{tp}$, with a slight overestimation. Friedel's correlation exhibits a greater overestimation the experimental data. However, both correlations follow a similar pattern to that of the experimental data.

In Fig. 5.23, the pressure drops $\left(\frac{\Delta p}{\Delta L}\right)_{tp}$ along the tube are reported as function of the vapor quality x. The two graphs reported describe two test conditions, Measurement 1 ($p^* = 0.25$; $G = 600\ \frac{kg}{m^2 s}$;) and Measurement 3 ($p^* = 0.5$; $G = 600\ \frac{kg}{m^2 s}$;).

The legend is the same already explained for Fig. 5.11.

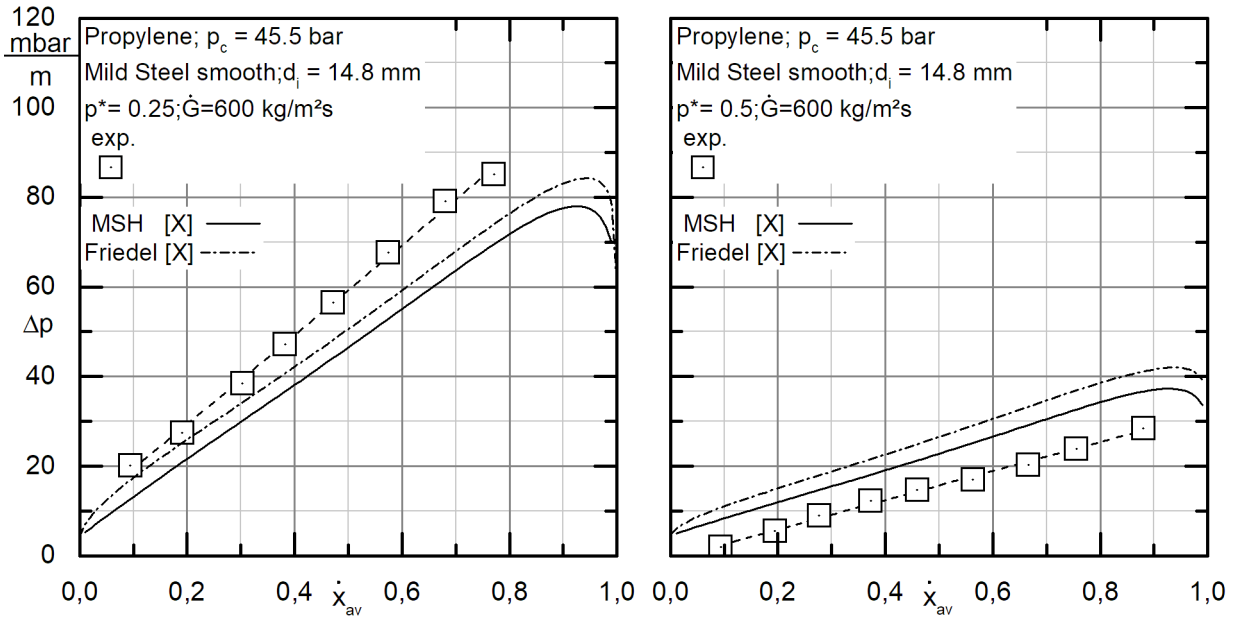

FIGURE 5.23 - COMPARISON BETWEEN THE EXPERIMENTALLY MEASURED VALUES OF PRESSURE DROPS AND THE VALUES PREDICTED BY MULLER-STEINHAGEN'S [28] AND FRIEDEL [27] CORRELATIONS.

In the graph on the left-hand side, the reduced pressure $p^* = 0.25$ and the mass flux $G = 600\ \frac{kg}{m^2 s}$.
Both correlations underestimate the pressure drops, for every value of vapor quality x considered. Friedel's correlation predicts the pressure drops with a good accuracy for low vapor qualities x. As $x > 0.3$, the experimental data separate progressively more from the correlation as vapor quality x increases. At high vapor quality $x = 0.9$, the error exceeds 10% for Friedel's correlation.
Muller-Steinhagen's correlation curve, having a similar trend to Fridel's one, behaves in a similar way but displaying a higher offset. At vapor quality $x = 0.9$, the error exceeds 15% for Muller's correlation.
In the graph on the right-hand side, the reduced pressure $p^* = 0.5$ and the mass flux $G = 600\ \frac{kg}{m^2 s}$.
In this case, the offset between the data and the correlations is considerable, with a smaller overestimation for Muller-Steinhagen's correlation.
The offset is almost constant as vapor quality x increases, showing that the trend of the experimental points is well predicted by both correlating functions.

In Fig 5.24, Muller-Steinhagen's correlation [28] is evaluated in comparison with the experimental data in a parity plot. The graph reports Muller-Steinhagen's calculated pressure drops $\left(\frac{\Delta p}{\Delta L}\right)_{calc}$, on the y-axis, as function of the experimentally measured pressure drops $\left(\frac{\Delta p}{\Delta L}\right)_{exp}$, on the x-axis. In the graph, the solid line represents the bisector, while the three dotted lines that represent the percentual deviation of the calculated values from the experimental results.

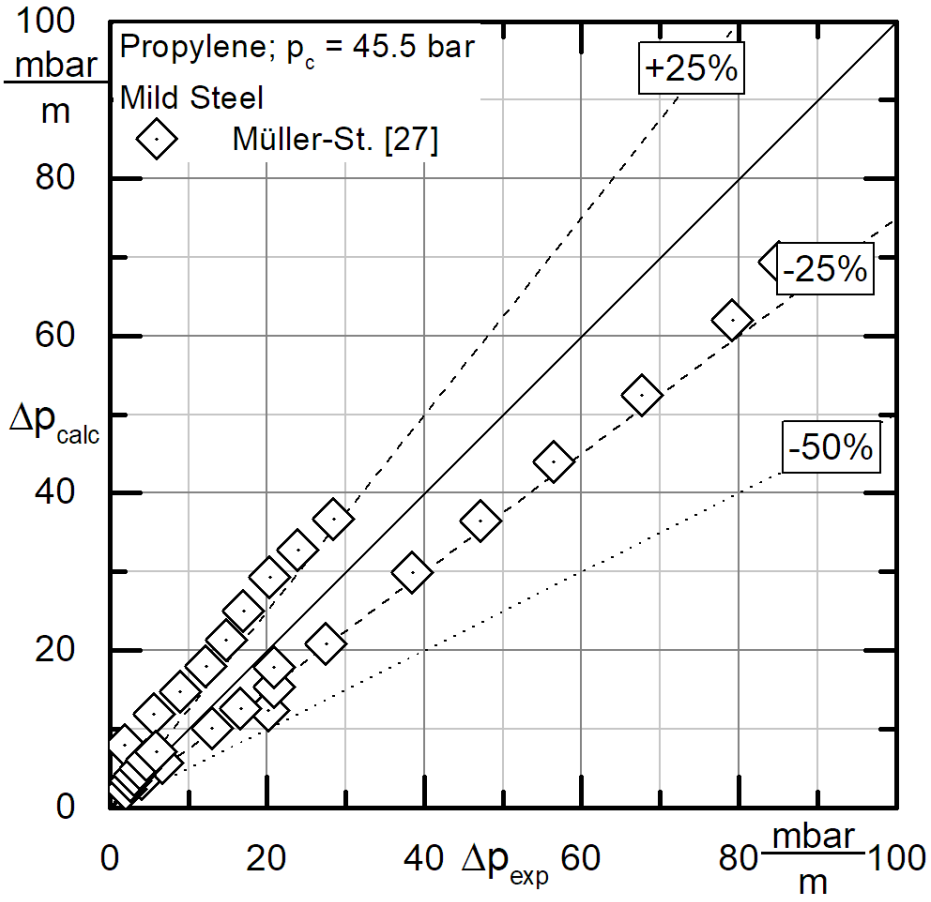

FIGURE 5.24 - PARITY PLOT FOR MULLER-STEINHAGEN'S [28] CORRELATION

It can be observed that a fair number of points, 70% lies outside from the area identified by the two straight lines representing a positive or negative deviation of 25% from the bisector. This means that the pressure drops are not assessed by the used Muller-Steinhagen's correlation with the highest degree of accuracy. Nevertheless, none of the points exceeds 50% inaccuracy.

In Fig 5.25, Friedel's correlation [27] is evaluated in comparison with the experimental data in a parity plot. The graph reports Friedel's calculated pressure drops $\left(\frac{\Delta p}{\Delta L}\right)_{calc}$, on the y-axis, as function of the experimentally measured pressure drops $\left(\frac{\Delta p}{\Delta L}\right)_{exp}$, on the x-axis. As in Fig…, the bisector is identified by a solid line while the three dotted lines represent the percentual deviation of the calculated values from the experimental results.

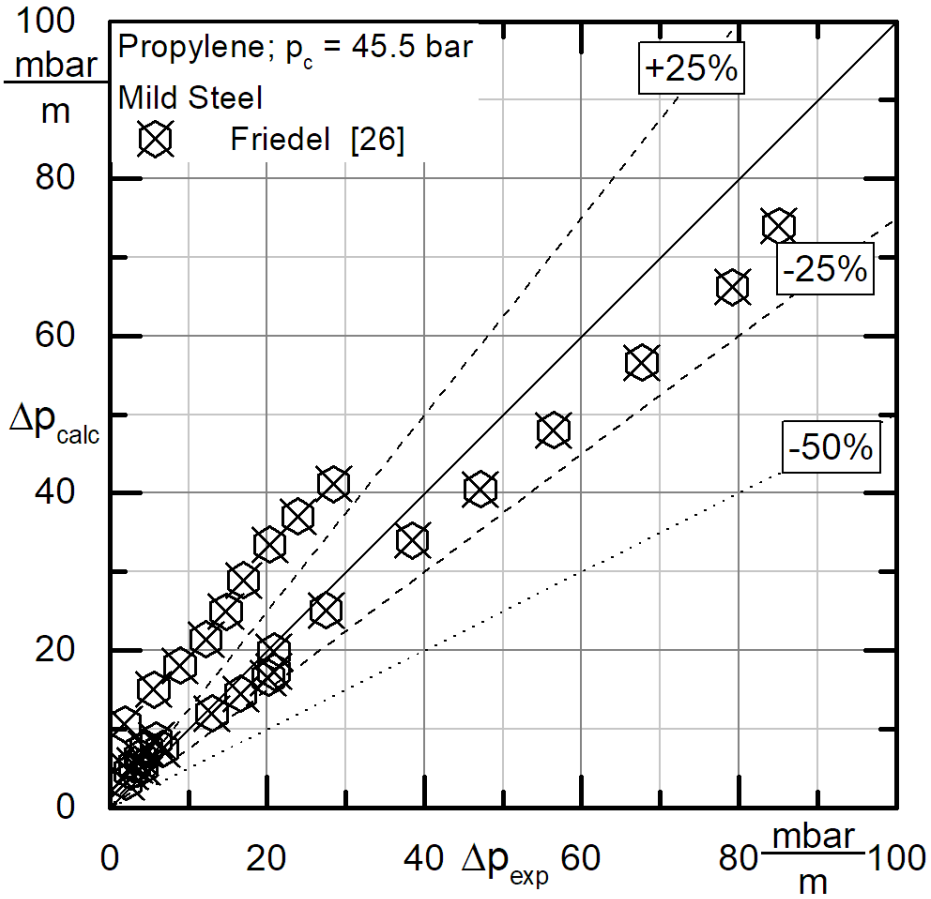

FIGURE 5.25 - PARITY PLOT FOR FRIEDEL'S [27] CORRELATION

It can be observed that most of the points, 70% lies inside the area identified by the two straight lines representing a positive or negative deviation of 25% from the bisector.

6. Conclusions and Outlook

The present work has been focused on the study of flow condensation of propylene inside a horizontal tube. The study of this complex mechanism is important in several applications like heat pumps, air conditioning systems and the chemical industry. The experimental work has been done exploiting an industrial scale test rig made available by TTK, at the University of Kassel.

In the first part of the work, a literature review has been conducted with the goal of studying and presenting the current knowledge on flow condensation. In particular, the study focused on flow pattern maps [8] [10], heat transfer models [19] [20] and pressure drop models [24] [27] [28].

The experimental work included the calibration of the thermocouples that, subsequently, have been glued on the test tube. Once equipped and ready, the test tube has been surrounded by the annular tube to realize the tube-shell-heat exchanger required for the intended experimental plan. Propylene flows in the test tube, while cooling oil flows in the annular, in counter-flow configuration. After having installed the heat exchanger in the test rig, the measurement plan has been carried out and it was possible to collect the experimental data required for the flow condensation analysis. The measurements have carried out for two values of reduced pressure, $p^* = 0.25$ and $p^* = 0.5$ and two values of mass flux $G = 600\ \frac{kg}{m^2 s}$ and $G = 300\ \frac{kg}{m^2 s}$. The experimental runs have been conducted setting different inlet vapor qualities, from $x = 0.1$ to $x = 0.9$, with a step variation of $\Delta x = 0.1$. The results related to local heat transfer have been critically analyzed and commented, highlighting weaknesses related to the experimental set up and the Data Reduction. The experimentally derived overall heat transfer coefficients α were then analyzed and compared with the literature. With the aid of parity plots, it was proved that the heat transfer models of Thome [19] and Shah [20], can predict the experimental data obtained in this work with a good

degree of accuracy. For both models, above 90% of the measured points are predicted within an uncertainty range of $\pm 25\%$. It was proved that the pressure drops models of Friedel [27] and Muller-Steinhagen [28], can predict the experimental data obtained in this work with an acceptable degree of accuracy. For both models, 70% of the measured points are predicted within an uncertainty range of $\pm 25\%$.

The conducted investigation on the local heat transfer allowed to remark the dependency of the heat transfer coefficient α on the radial position ϕ of the test tube. Specifically, under test conditions associated with the occurrence of stratified flow, the heat transfer coefficient α varies considerably as function of the radial position ϕ. Under the conditions associated with high turbulence and annular flow, the heat transfer coefficient α is approximately constant as function of the radial position ϕ. It is important to state that these observations were more evident under the conditions in which the average temperature difference between propylene and the cooling oil was higher.

For some measurement conditions, it was also possible to compare the local results obtained with the photos of the glass tube at the inlet of the test section. This allowed to support some of the assumptions made on the flow regime inside the tube. Analyzing the graphs of the overall heat transfer coefficient α as function of vapor quality x, in the different condensation conditions, it was possible to experimentally prove that the heat transfer coefficient α increases as the mass flux G increases. In the same way, it was possible to demonstrate that the heat transfer coefficient α decreases as the pressure p increases. By comparing the results regarding overall heat transfer and pressure drops, it was possible to verify that a high heat transfer coefficient α is always coupled with a high value of pressure drops Δp_{tot}.

In the following, the critical aspects of the present work are reported, and some future developments are suggested.

- TCs' uncertainty has an important impact on the uncertainty of the results. Unfortunately, not much can be done beyond proceeding to

calibration and calculating an additional offset at ambient temperature T_{amb}.

- The gluing of the TCs on the test tube is certainly a critical procedure. However, despite the utmost care taken, being a manual work, it is not easily improved.
- The presence of numerous obstacles within the annular results in disruptions in the oil flow. As result of this, the heat transfer on the oil side may be locally more efficient in some radial positions compared to others. Consequently, the measured local temperature differences ΔT_{loc} may be influenced. This effect on the oil flow may be partially reduced by decreasing the number of RTDs for the oil temperature. Another mitigating solution would be that of increasing the diameter d of the annular tube.
- The high sensitivity of the Data Reduction is a major weakness point. This problem is more severe when the local temperature differences ΔT_{loc} are small. In fact, it has been observed that at higher ΔT_{loc}, the sensitivity of the Data Reduction is highly reduced. With the goal of increasing the local temperature differences ΔT_{loc}, a higher ΔT_{sup} could be set. In this way, the temperature profiles of propylene and oil (See Fig. 4.6) would separate from one another. Consequently, the local temperature differences ΔT_{loc} would also be increased. It is important to remember that if the heat flow rate $\dot{Q}$ needs to be kept constant, the oil mass flow rate $\dot{m}_{oil}$ will need to be decreased accordingly. It must be also kept in mind that the specific heat at constant pressure, c_p is a function of temperature T.
- In a future study, it would be interesting to investigate further flow condensation conditions in terms of mass flux G and reduced pressure p^*.

7. References

[1]	Watco-Group. [Online]. Available: https://www.watco-group.co/surface-condenser-in-thermal-power-plant/. [Accessed 12 June 2023].
[2]	Bitzer. [Online]. Available: https://www.bitzer.de/shared_media/documentation/dp-200-6-en.pdf. [Accessed 12 June 2023].
[3]	D. M. Warsinger, K. H. Mistry, K. G. Nayar, H. W. Chung and J. H. Lienhard V., "Entropy Generation of Desalination Powered by Variable Temperature Waste Heat," *Entropy,* no. 17, pp. 7530-7566, 2015.
[4]	P. Cheng, H. Y. Wu and F. J. Hong:, "Phase-change heat transfer in microsystems," *J. Heat Transfer,* no. 129, pp. 101-108, 2007.
[5]	X. Fang, Z. Zhou and D. Li, "Review of flow boiling heat transfer coefficients for carbon dioxide.," *Int. J. Refrigeration,* no. 36, pp. 2017-2039, 2013.
[6]	T. Harirchan and S. Garimella, "A comprehensive flow regime map for microchannel flow boiling with quantitative transition criteria.," *Int. J. Heat Mass Transfer,* Vols. 13-14, no. 53, pp. 2694-2702, 2010.
[7]	L. Rossetto, "Lesson: Condensation in horizontal and vertical channel/tube and in micro-finned horizontal tube," Padova, Italy, 2022.
[8]	J. El Hajal, J. Thome and A. Cavallini, "Condensation in horizontal tubes, part 1: two-phase," *International Journal of Heat and Mass Transfer,* no. 46, pp. 3349-3363, 2003.
[9]	J. A. Mikie, «Condensation of hydrocarbons and zeotropic hydrocarbon/refrigerant mixtures in horizontal tubes.,» in

	Dissertation, Georgia Institute of Technology, , Georgia, USA, 2014.
[10]	M. Kind, Y. Saito, O. Herbst and A. Katsaounis, VDI-Wärmeatlas - Chapter 3, Heidelberg, 2013.
[11]	G. Breber, J. W. Palen e J. Taborek, «Prediction of Horizontal Tubeside Condensation of Pure Components Using Flow Regime Criteria,» *J. Heat Transfer ,* n. 102, pp. 471-476, 1980.
[12]	Y. Taitel and A. E. Dukler, "A model for predicting flow regime transitions in horizontal and near horizontal gas-liquid flow," *AIChE Journal,* no. 22, pp. 47-55, 1976.
[13]	N. Kattan, J. Thome and D. Favrat, "Flow boiling in horizontal tubes: Part 1—Development of a diabatic two-phase flow pattern map," *J. Heat Transfer,* no. 120, pp. 140-147, 1998.
[14]	O. Zurcher, J. Thome and D. Favrat, "Evaporation of ammonia in a smooth horizontal tube: heat transfer measurements and predictions," *J. Heat Transfer,* no. 121, pp. 89-101, 1999.
[15]	P. Kosky and F. Staub, "Local condensing heat transfer coefficients in the annular flow regime," *AIChE Journal,* no. 17, pp. 1037-1043, 1971.
[16]	T. Von Karman, "The analogy between fluid friction and heat transfer," *Trans. ASME ,* no. 61, pp. 705-711, 1939.
[17]	V. G. Rifert and V. V. Sereda, "Condensation inside smooth horizontal tubes, part 1: Survey of methods of heat-exchange prediction.," *Thermal Science,* no. 19, pp. 1769-1789, 2015.
[18]	D. P. Traviss, "Forced convection condensation inside horizontal tubes," in *Bericht, Massachusetts Institute of Technology*, Cambridge, Massachussetts, 1971.

[19]	J. Thome, J. E. Hajal and A. Cavallini, "Condensation in horizontal tubes, part 2: new heat transfer model based on flow regimes," *International Journal of Heat and Mass Transfer,* no. 46, pp. 3365-3387, 2003.
[20]	M. M. Shah:, "Comprehensive correlations for heat transfer during condensation in conventional and mini/micro channels in all orientations," *International Journal of Refrigeration,* no. 67, pp. 22-41, 2016.
[21]	F. Mayinger, "Strömung und Wärmeübergang in Gas-Flüssigkeits-Gemischen.," in *Springer Wien*, Wien, Austria, 1982.
[22]	H. Schmidt, A. Wellenhofer, S. Muschelknautz, D. M. J. Schmidt, A. Mersmann and J. Stichlmair, "Zweiphasige Gas-Flüssigkeitsströmungen," in *Kapitel L2, VDI-Wärmeatlas*, Berlin, Springer Verlag, 2013, pp. 1285-1358.
[23]	S. Rouhani and E. Axelsson, "Calculation of void volume fraction in the subcooled and quality boiling regions," *International Journal of Heat and Mass Transfer,* vol. 2, no. 13, pp. 383-393, 1970.
[24]	R. Lockhart and R. C. Martinelli, "Proposed correlation of data for isothermal two-phase, two-component flow in pipes," *Chemical Engineering Progress 45,* vol. 1, no. 45, pp. 39-38, 1949.
[25]	W. Kast, "Strömungsdynamik und Druckverlust," in *Chapter 1, L1.2, VDI-Wärmeatlas*, Berlin, Springer Verlag, 2013.
[26]	H. Lee and Lee S.Y., "Pressure drop correlations for two-phase flow within horizontal rectangular channels with small heights," *International Journal of Multiphase Flow,* pp. 783-796, 2001.
[27]	L. Friedel, "Improved friction pressure drop correlations for horizontal and vertical two phase pipe flow," *3R international,* no. 18, pp. 485-491, 1979.

[28]	H. Muller-steinhagen and K. Heck, "A Simple Friction Pressure Drop Correlation for Two-Phase Flow in Pipes," *Chem. Eng. Process,* no. 20, pp. 291-308, 1986.
[29]	E. Tegeler, F. Bernhard and S. Rudtsch, "Manual of Temperature Measurement.," in *Chapter 7 Calibration of Contact Thermometers*, Berlin, Springer-Verlag, 2014.
[30]	A. Cavallini, D. Del Col, L. Doretti, M. Matkovic, L. Rossetto and C. Zilio, "Condensation in Horizontal Smooth Tubes: A New Heat Transfer Model for Heat Exchanger Design," *Heat Transfer Engineering,* vol. 8, no. 27, pp. 31-38, 2006.